

Synthesis and characterization of magneto-electric nanoparticles for delivery of anti-tuberculosis drugs across the blood-brain barrier



Sinaye Mhambi

A mini-thesis submitted in partial fulfilment of the requirements for the degree of Magister Scientiae in Nanoscience in the Department of Medical Bioscience, University of the Western Cape.

Supervisor: Prof. Admire Dube
Co-supervisor: Prof. David Fisher

2022

ABSTRACT

The anatomical structure of the brain at the blood–brain barrier (BBB) creates a limitation for the movement of drugs into the central nervous system (CNS). Although anti-infective drugs effective against *Mycobacterium tuberculosis* are known, the effective delivery of such drugs across the BBB remains a major challenge. This is due in part to insufficient drug penetration across the BBB of some anti-TB drugs. Large hydrophilic drugs such as ethambutol have poor cerebrospinal fluid (CSF) penetration and cannot cross the BBB even when they are inflamed. Increasing the dose of ethambutol in order to obtain higher CNS penetration is pernicious as it may result in systemic toxicity. Drug delivery facilitated by magneto-electric nanoparticles (MENS) is a relatively new non-invasive approach for the delivery of drugs into the CNS. These nanoparticles (NPs) can create localized transient changes in the permeability of the cells of the BBB by inducing electroporation. However, MENS have not been applied to deliver antibiotics towards the treatment of TB infections in the CNS.

The key objectives of this study were to (i) synthesize $\text{CoFe}_2\text{O}_4 @ \text{BaTiO}_3$ core shell MENS, (ii) characterize the physicochemical and magnetic properties of the NPs, and (iii) determine the characteristics of nanoelectroporation and the uptake of ethambutol across the BBB. Brain endothelial cell-based *in vitro* models utilized immortalized mouse brain endothelioma (bEnd5) cell lines to test the permeability of MENS across the BBB. This was achieved through the hydrothermal synthesis and characterization of monodisperse, crystalline $\text{CoFe}_2\text{O}_4 @ \text{BaTiO}_3$ core shell MENS with an average hydrodynamic size of 28 nm. Transmission electron microscopy (TEM) and atomic force microscopy (AFM) was used to determine the morphology and size of the MENS. X-ray diffraction (XRD) was used to determine the crystalline structure and the nature of the phases of MENS. The interaction of MENS with bEnd5 cells in the presence of ethambutol as well as nanoporation formation on bEnd5 cells was analyzed using scanning electron microscopy (SEM). A magnetic system consisting of a Helmholtz coil, a magnetometer, alternating current (AC) and direct current (DC) power supply was used to determine the effect of exposure of bEnd5 cells to MENS and ethambutol and to induce nanoporation on bEnd5 cells. The trypan blue method was used to determine the cytotoxicity of MENS on bEnd5 cells.

The average MENS size achieved during this study was 28 nm in diameter. Furthermore, these tetragonal crystalline MENS had an average polydispersity index (PDI) and zeta potential (ZP) value of 0.265 ± 0.06 and -33.3 ± 0.1 mV, respectively. The results of the phase purity and crystallinity of MENS met precisely with the standard data for BTO (JCPDS Card No. 05-0626)

and CFO (JCPDS Card No. 22-1086). The data showed that MENs are biologically compatible with bEnd5 cells. The data also showed that low-level magnetic fields do not have an effect on the cytotoxicity of bEnd5 cells *in vitro*. The $\text{CoFe}_2\text{O}_4 @ \text{BaTiO}_3$ core shell MENs were able to effectively induce transient nanoporation on bEND5 cells leading to enhanced uptake of ethambutol across the cells. Ethambutol was observed to cross the BBB in the presence of the MENs although this was not statistically different to that of ethambutol alone. We conclude that MENs are promising systems for effective CNS drug delivery and treatment for these diseases, however, further *in vitro* and *in vivo* studies are required to achieve translation of this approach to the clinic.

Key words: CNS TB, BBB, drug delivery system, MENs, nanoelectroporation, magnetic field



DECLARATION

I, Sinaye Mhambi, declare that 'Design of magneto-electric nanoparticles for delivery of anti-tuberculosis drugs across the blood-brain barrier' is my own work. It is being submitted for the Degree of Master of Nanoscience at the University of the Western cape, Cape Town, South Africa. It has not been submitted before for any degree or examination at this or any other University, and all the sources I have used or quoted have been indicated and acknowledged by means of complete references.

Signature

Date



ACKNOWLEDGEMENTS

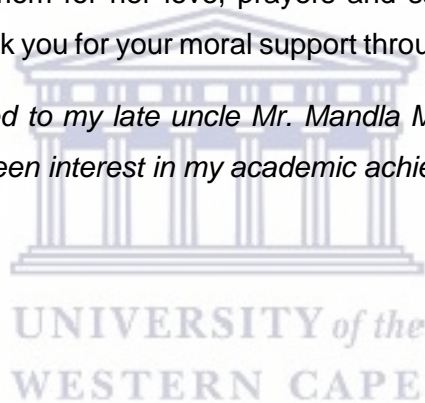
First and foremost, praises and thanks to God, the Almighty, for His blessings and for providing me with strength throughout my research work to complete this research successfully.

The completion of this thesis would not have been possible without the expertise and support of my supervisor, Professor Admire Dube. I thank God for your patience, for believing in me and for your open-door policy. May God continue to increase you and bless you.

I would like to thank my co-supervisor Professor David Fisher for being so welcoming and for providing me with assistance and space in his laboratory. I would also like to thank Professor Moise Tchokonte Tchoula for his guidance, open-door policy and willingness to share his laboratory space with me.

I am extremely grateful to my mom for her love, prayers and sacrifices for my education and preparing me for my future. Thank you for your moral support through this research work, MaNtuli.

This research thesis is dedicated to my late uncle Mr. Mandla Mani who has been my biggest support and has always taken keen interest in my academic achievements.



LIST OF ABBREVIATIONS

AC	Alternating current
AFM	Atomic force microscope
AP-1	Atherosclerotic plaque-specific peptide-1
AP-1 Lipo-Dox	Atherosclerotic plaque-specific peptide-1-conjugated liposomes containing doxorubicin
ART	Antiretroviral therapy
AUC	Area under the curve
AZTTP	Azidothymidine 50-triphosphate
BBB	Blood-brain barrier
BBMEC	Bovine brain endothelium cell model
BCECs	Brain capillary endothelial cells
bEnd5	Brain endothelial cell line
BL	Basal lamina
BTO	Barium titanate
BCSFB	Blood-cerebrospinal fluid barrier
CFO	Cobalt ferrite
CNS	Central nervous system
CRISPR	Clustered regulatory interspaced short palindromic repeat
CSF	Cerebrospinal fluid
CTAB	Cetyl Trimethyl Ammonium Bromide
Cur	Curcumin
DC	Direct current
DLS	Dynamic light scattering
FIB-TEM	Focused ion beam transmission electron microscope
GLUT1	Glucose transporter 1
GMO	Glycerol monooleate
HBMECs	Human brain macrovascular endothelial cells

HBMVE	Human brain microvascular endothelial cells
HEP2	Human epithelium type 2 cells
HIFU	High-intensity focused ultrasound
HIV	Human Immunodeficiency Virus
HPLC	High performance liquid chromatography
IONPs	Iron Oxide Nanoparticles
Log P	Lipophilicity
LRP	Lipoprotein receptor-related protein
MDR-TB	Multi drug-resistant tuberculosis
MENs	Magneto-electric nanoparticles
MFM	Magnetic force microscopy
MRI	Magnetic resonance imaging
NaOH	Sodium hydroxide
NPs	Nanoparticles
Oe	Oersted
PAMAM	Polyamidoamine
PLGA	Poly(lactic-co-glycolic acid)
PNIPAm	Poly-N-Isopropylacrylamide
PNA	Polyamide ('peptide') nucleic acid
PTX	Paclitaxel
siRNA	Small interfering ribonucleic acid
SPIONs	Superparamagnetic iron oxide nanoparticles
STS	Scanning tunneling spectroscopy
TB	Tuberculosis
TBM	Tuberculosis meningitis
TEM	Transmission electron microscope
Tf	Transferrin
THL	Trojan horse liposome

WHO

World Health Organization

XRD

X-ray diffraction



LIST OF PUBLICATIONS

Mhambi, S., Fisher, D., Tchokonte, M.B.T. and Dube, A., 2021. Permeation Challenges of Drugs for Treatment of Neurological Tuberculosis and HIV and the Application of Magneto-Electric Nanoparticle Drug Delivery Systems. *Pharmaceutics*, 13(9), p.1479.



LIST OF FIGURES

Figure 2.1. Schematic structure of the BBB with endothelial cells separated by a tight junction and surrounded by an astrocyte, microglia, neuron, pericytes and smooth muscle (BL1 is basal lamina 1, BL2 is basal lamina 2) (He et al., 2018).....	20
Figure 2.2. Strategies for crossing the BBB to deliver drugs. (A) Invasive approach: injection into the parenchyma of the brain is used to avoid the BBB when treating patients. (B) BBB disruption is achieved by injection of chemical agents, osmolytes or via focused ultrasound. This technique causes loosening of the tight junctions of the endothelium, permitting access to the brain by conventional drugs. (C) Transcellular transport of drug molecules through a cell.	23
Figure 2.3. Illustration of transport pathways for BBB transport. (A) The transcellular lipophilic pathway allows the passive diffusion of small, lipophilic molecules across the BBB and into the brain. (B) Carrier-mediated transport employs specific proteins to move molecules from the environment into and through the cell. (C) Endocytosis of molecules via adsorptive transcytosis nonspecifically and transported through the cell. (D) Specific ligands bind receptors and are endocytosed and transported through the cell via receptor-mediated transcytosis. (E) Translocation of MENs across the BBB. Once MENs have been administered into the body, an externally applied magnetic field changes the shape of the inner core. Magnetostriction, changes the shape of the piezoelectric shell. The magnetic field induces the nanoelectroporation of the diseased cell (see Section 2.4).	25
Figure 2.4.1. Schematic diagram showing different types of NPs (Karimi and Ghasemi, 2015)..	33
Figure 2.4.2. Schematic diagram of the effect of an applied magneto-electric field on core-shell MENs. MENs surrounded by a polyvinylpyrrolidone (PVP) polymer layer and glycerol monooleate layer with a drug loaded on the surface of MENs. Upon the introduction of low st.....	35
Figure 4.2. Hydrodynamic diameter (nm) of MENs synthesized by means of the hydrothermal method, in triplicate (sample 1, sample 2 and sample 3) calcined at 600 °C for 5 h. The degree of statistical significance is annotated with an asterisk (*); $p < 0.05$ (*),	53
Figure 4.3. Gel recovered from the liquid evaporation method of synthesis of MENs. The inner gel appears soft in texture while the outer surface of the gel appears hard.	55
Figure 4.4. Average sizes (nm) of MENs calcined at different temperatures (°C) measured using dynamic light scattering. H.R denotes MENs calcined using the heat rate method (see section 4.2.1). Samples that are statistically significant are annotated with an aster57	57

Figure 4.5. TEM images of the morphology of MENs at a) 100 nm scale. BTO (shell) and CFO (core) structure of MENs at b) 10 nm scale and c) 20 nm scale. A, B and C show that MENs vary in size from as small as 5 nm and showing an average of 36.5 nm (see figure 4.6).59

Figure 4.6. The morphology and average core-shell diameter of MENs. (a) TEM images of MENs at 100 nm scale, (b) the number size distribution of MENs measured using ImageJ Software. .60

Figure 4.7. A) AFM image of BTO (shell) CFO (core) MENs. The particle distribution of the MENs was inhomogeneous and most of the MENs had an almost spherical appearance which further confirmed the morphology and size distribution seen in the TEM images. B) the numbe63

Figure 4.8. XRD pattern of tetragonal crystalline cobalt ferrite (CFO) – barium titanate (BTO) MENs calcined at 600°C. These MENs showed the presence of both CFO (#) and BTO (*). The diffraction peaks in the curve could be indexed to tetragonal MENs.....64

Figure 4.1. Magnetic test on paper. MENs powder on upper side of blank A4 paper placed horizontally under a mobile magnet.....53

Figure 5.2. Viability of cells exposed to a primary control (C1) (growth media only), second control (C2) (bEnd5 cells only) and different concentrations of MENs for 12 h, 24 h and 48 h.73

Figure 5.5. Relative cell viability (%) of controls and concentrations of ethambutol: 50 µg/ml, 100 µg/ml, and 150 µg/ml.78

Figure 5.1. Helmholtz coil connected to an ac power supply where cell culture samples are exposed to a magnetic field.....70

Figure 5.3. Relative cell viability (%) of controls and cells exposed to 0.1 mg/mL MENs (the highest non-toxic dose observed) for 48 h after 30 min exposure to a DC-magnetic field stimulation. ...74

Figure 5.4. The effect of varying AC-magnetic fields on cell viability of MENs exposed to bEnd5 cells at set time points. Controls, 0,05 mg/ml MENs and 0.1 mg/ml MENs were exposed to bEnd5 cells to 0, 10 and 17.23 Oe ac-magnetic field for 0 min, 30 min and 1 h at.....75

Figure 5.6.1. SEM images showing the interaction of MENs and drug (150 µg/ml ethambutol) with the bEnd5 monolayer seeded at 50 000 cm³ cells per well on a Transwell insert membrane (12 mm diameter with a 0.45 µm pore size) (Millicell™) for 48 h on a 500 nm scale80

Figure 5.6.2. SEM images showing the interaction of MENs and drug (150 µg/ml ethambutol) with the bEnd5 monolayer seeded at 50 000 cm³ cells per well on a Transwell insert membrane (12 mm diameter with a 0.45 µm pore size) (Millicell™) for 48 h on a 500 nm scale.....81

Figure 5.6.3. SEM images showing the interaction of MENs and drug (150 µg/ml ethambutol) with the bEnd5 monolayer seeded at 50 000 cm³ cells per well on a Transwell insert membrane (12 mm diameter with a 0.45 µm pore size) (Millicell™) for 48 h on a 500 nm scale.....82

Figure 5.7. The effect of exposure of 150 µg/ml ethambutol only, ethambutol (150 µg/ml) and 0.05 mg/ml, and ethambutol (150 µg/ml) and 0.1 mg/ml MENs to an hour of DC and AC-magnetic field stimulation. This data shows the average % of.....84



LIST OF TABLES

Table 2.1. Non-invasive approaches for the delivery of drugs across the BBB	24
Table 2.2. Techniques used to characterize the physicochemical properties of MENs.	39
Table 4.1. Materials used in the study	47
Table 4.2. Hydrodynamic size (nm), PDI and ζ - potential of MENs synthesized using the liquid phase evaporation method of synthesis.	56



TABLE OF CONTENTS

DECLARATION	4
ACKNOWLEDGEMENTS	5
LIST OF ABBREVIATIONS	6
LIST OF FIGURES.....	10
LIST OF TABLES	13
CHAPTER ONE.....	17
INTRODUCTION.....	17
CHAPTER TWO	19
LITERATURE REVIEW.....	19
2.1 The BBB and CNS TB	19
2.2. Drug Permeation Challenges in CNS TB Treatment	20
2.3. Drug Delivery Across the BBB.....	21
2.3.1. Noninvasive drug delivery approaches.....	23
2.3.2. Nanoporation	29
2.4. Nanoparticles and MENs.....	30
2.4.1. NPs as delivery systems for drugs across the CNS	31
2.5. Synthesis and characterization of MENs.....	37
2.6. <i>In vitro</i> models of the BBB and determining drug uptake across the BBB	42
2.7. Application of MENs to deliver drugs across the BBB	45
CHAPTER THREE	47
AIMS, HYPOTHESIS, OBJECTIVES, RATIONALE	47
3.1. Problem statement	47
3.2. Aims.....	47
3.3. Hypothesis.....	47
3.4. Objectives.....	47
3.5. Rationale.....	47
CHAPTER FOUR	49
SYNTHESIS AND CHARACTERIZATION OF MENs	49
4.1. Introduction.....	49
4.2. Materials.....	49

4.3. Methods	51
4.3.1. Synthesis of MENs (hydrothermal method)	51
4.3.2. Synthesis of MENs (liquid phase evaporation method)	52
4.4.1. Size, polydispersity index, ζ - potential and shape	52
4.4.2. TEM analysis	53
4.4.3. pXRD analysis	53
4.4.4. AFM analysis	53
4.4.5. Determination of the magnetic properties and atomic forces of MENs.	54
4.5. Statistical analysis	54
4.6. Results and discussion	55
4.6.1. MENs synthesized using the hydrothermal method	55
4.6.3. The effect of calcination temperatures and heating rate on the hydrodynamic sizes of MENs.....	59
4.7. Transmission electron microscopy of MENs.....	61
4.8. Atomic force microscopy of MENs.....	64
4.10. XRD analysis of MENs	66
CHAPTER FIVE	68
CYTOTOXICITY, NANOPORATION AND DRUG TRANSPORTATION STUDIES OF MENs ...	68
5.1. Introduction.....	68
5.2. Materials.....	68
5.3. bEnd5 cell culture and seeding.....	70
5.4. Evaluation of the cytotoxicity effects of MENs on bEnd5 cells.....	70
5.5. Determination of cytotoxicity in the presence of DC and AC-magnetic field stimulation... ..	71
5.6. Ethambutol transportation across bEnd5 cells in the presence of MENs.....	74
5.7. LC-MS analysis of ethambutol	74
5.8. Statistical analysis	75
5.9. Results and Discussion	76
5.9.1. Cytotoxicity of MENs in the absence of magnetic field stimulation	76
5.9.2. Relative cell viability of MENs post-exposure to varying DC- magnetic fields.....	77
5.9.4. Cytotoxicity of different concentrations of ethambutol.....	80
5.9.6. Transportation of ethambutol across the BBB.....	86
CHAPTER SIX.....	88
CONCLUSION.....	88

CHAPTER SEVEN..... 89
REFERENCES 89



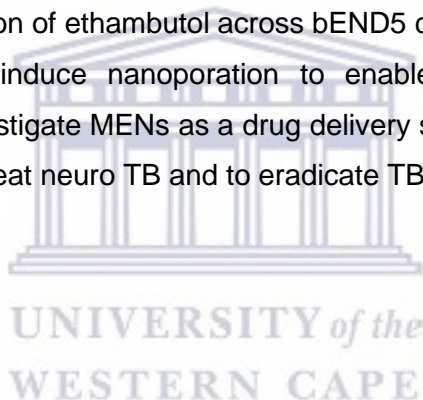
CHAPTER ONE

INTRODUCTION

TB is an infectious disease caused by the bacillus *Mycobacterium tuberculosis* (*M. tb*). Typically, TB affects the lungs but can spread and affect other sites of the body, i.e., extrapulmonary TB (Rodriguez-Takeuchi et al., 2019). TB in the CNS is referred to as CNS TB and is one of the less common yet highly devastating mycobacterial infections in humans (Cherian and Thomas, 2011)(Leonard, 2017). CNS TB is differentiated from TB meningitis (TBM) in that CNS TB begins as small tuberculous foci (Rich foci) in the brain, spinal cord or meninges (Cherian and Thomas, 2011), whereas TBM is a form of meningitis characterized by *M. tb* induced inflammation of the meninges. The location of the foci and the sites in which they are found determines their ability to be controlled as well as the type of CNS TB that occurs (Cherian and Thomas, 2011). In 2019, the global burden of new cases of TB was estimated to be 10.0 million of which 8.2% resulted from concomitant HIV-TB co-infections (World Health Organization, 2020)(Chakaya et al., 2021). In that same year, an estimated 1.2 million HIV-negative people died from TB and an additional 208,000 deaths occurred among HIV positive people (Chakaya et al., 2021). Two-thirds of the global TB incidence in 2019 was accounted for by eight countries led by India (26%), followed by Indonesia (8.5%), China (8.4%), the Philippines (6.0%), Pakistan (5.7%), Nigeria (4.4%), Bangladesh (3.6%) and South Africa (3.6%) (World Health Organization, 2020)(Chakaya et al., 2021). CNS TB accounts for 1% to 2% of active TB cases of which 15% to 40% of patients diagnosed with CNS TB die or become disabled even after anti-TB drug therapy (Chen et al., 2020). Children and adolescents are more prone to meningitis involvement as the clinical presentation, compared to adults (patients older than 15 years of age) (Picchio et al., 2020). This highlights the dire state of the prognosis of CNS TB. A major challenge in the treatment of CNS TB is the delivery of drugs across the BBB, where the endothelial cells of cerebral capillaries provide a highly regulated interface between the peripheral circulation and the CNS. Paracellular tight junctions between the endothelial cells prevent ions, molecules and unwanted cells from passively entering the brain (Daneman and Prat, 2015). Most of the anti-TB drugs are unable to penetrate the BBB in sufficient amounts to effectively eradicate TB from the CNS. For example, isoniazid and pyrazinamide exhibit good cerebrospinal fluid (CSF) penetration, while the concentrations of rifampicin in the CSF may not reach the minimum inhibitory concentrations required for eradication of *M.tb* (Alvarez-Uria et al., 2013)(Davis et al., 2018). Ethambutol penetrates the CSF poorly (Alvarez-Uria et al., 2013).

MENs are a class of NPs that exhibit magnetic and electrical properties that can be controlled using external magnetic and electric fields (Kaushik et al., 2014)(Rodzinski et al., 2016)(Stewart et al., 2018). These NPs can enhance transient permeability of the BBB through nanoelectroporation of cells. Nanoelectroporation is the use of focused electric pulse to porate the cell membrane to form a nanopore and also provides electrophoretic mobility of charged drug/gene molecules and/or NPs to move into the cell. Similar to other magnetic NPs, MENs have a nonzero saturation magnetization that could enable them to be guided throughout the body by the application of magnetic field gradients (Stimphil, 2017) (Stewart et al., 2018). Subsequently, these NPs could be localized using traditional image-guided magnetic processes such as MRI and magnetic particle imaging (Stewart et al., 2018) to facilitate drug delivery across the CNS.

This study focuses on the synthesis and characterization of $\text{CoFe}_2\text{O}_4 @ \text{BaTiO}_3$ core shell MENs, cytotoxicity studies of the MENs, determination of nanoporation in bEND5 cells by MENs and determination of the transportation of ethambutol across bEND5 cells facilitated by MENs. It was hypothesized that MENs will induce nanoporation to enable increased transportation of ethambutol. The intent is to investigate MENs as a drug delivery system for the transportation of ethambutol across the BBB to treat neuro TB and to eradicate TB in the brain.



CHAPTER TWO

LITERATURE REVIEW

2.1 The BBB and CNS TB

The BBB is formed by endothelial cells that line cerebral microvessels (Ulett and Beacham, 2014) and consists of enzymes, transporters, and physical barriers which together maintain a regulated microenvironment for reliable neuronal signaling (Daneman and Prat, 2015). There are three barrier sites between the blood and brain and these are (i) the BBB through tight junction formation located at the level of cerebral capillary endothelial cells which is the largest surface area for exchange, (ii) the blood-CSF barrier (BCSFB) situated at the choroid plexuses in the lateral, third and fourth ventricles of the brain, and (iii) the arachnoid barrier (Redzic, 2011). The BBB provides protection from circulating toxins or foreign substances that could cause brain infections while allowing vital nutrients to enter the brain. The CNS barriers prevent macromolecules or small molecules with unfavorable physicochemical properties from entering the brain, helps to keep the central and peripheral transmitter pools separate, keeps ionic composition optimal for synaptic signaling function and protects the CNS from neurotoxic substances circulating in the blood (Abbott et al., 2010) (Upadhyay, 2014). Tight junctions are vital in maintaining the integrity of endothelial cells lining the blood vessel in the brain. Further, tight junctions restrict paracellular diffusional pathway between endothelial cells to ions and other polar solutes thereby effectively inhibiting penetration of macromolecules (Figure 2.1) (Abbott et al., 2010). *M. tb* can reach the CNS causing CNS TB. This disease consists of a variety of neurological syndromes with high mortality and morbidity (Soleiman-Meigooni, 2018). CNS TB damages arachnoid, pia mater, brain parenchymal, nervi cerebrales, cerebrovascular, and the spinal cord (Soleiman-Meigooni, 2018) (Chen et al., 2020). Meningitis is the most common presentation of CNS TB (Soleiman-Meigooni, 2018). TBM is an inflammation of the meninges around the brain or spinal cord.

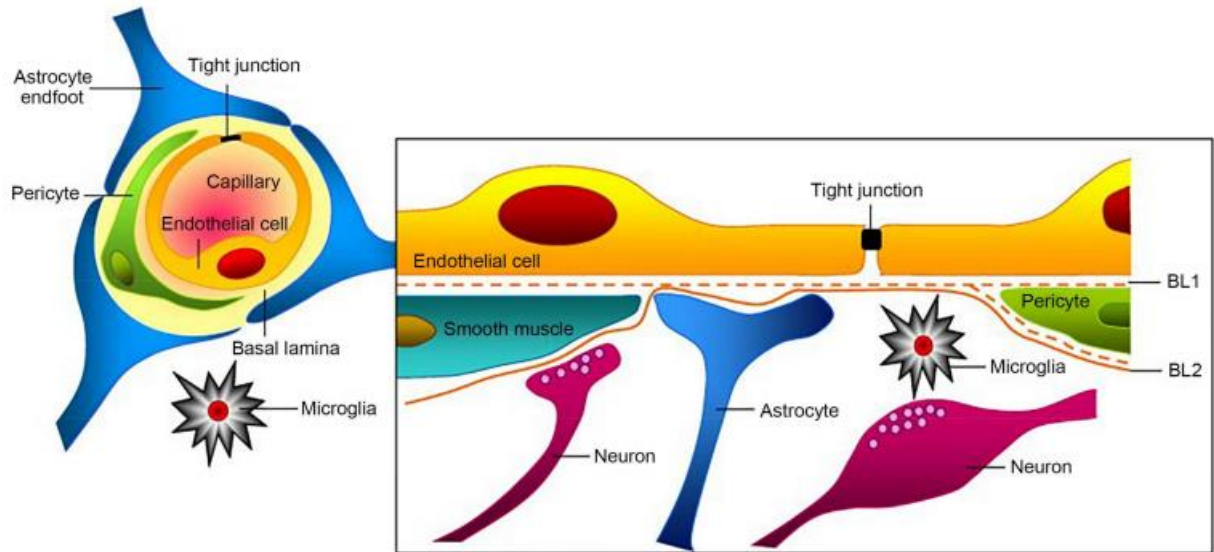


Figure 2.1. Schematic structure of the BBB with endothelial cells separated by a tight junction and surrounded by an astrocyte, microglia, neuron, pericytes and smooth muscle (BL1 is basal lamina 1, BL2 is basal lamina 2) (He et al., 2018).

2.2. Drug Permeation Challenges in CNS TB Treatment

The World Health Organization (WHO) guidelines suggest treatment of TBM with two months of rifampicin, isoniazid, pyrazinamide and ethambutol followed by ten months of rifampicin and isoniazid for all patients (Cherian et al., 2021). This guideline is based on the treatment guideline to treat pulmonary TB, which has been noted to not take into account the limited ability of anti-TB drugs to penetrate the BBB (Davis et al., 2018). Only lipophilic drugs can readily penetrate the BBB via lipid-mediated free diffusion provided that the drug has a molecular weight (M_w) <400 g/mol and forms less than 8 hydrogen bonds (Pardridge, 2012). Some antimicrobials (small hydrophilic molecules) like isoniazid and pyrazinamide are water-soluble agents and can cross the BBB paracellularly instead of transcellularly as seen with lipophilic agents (Azarmi et al., 2020). Optimal BBB penetration is achieved when the logP values of drugs are in the range of 1.5 to 2.7, with a mean value of 2.1 (Pajouhesh and Lenz, 2005). Isoniazid is hydrophilic (M_w 137.14 g/mol) and is, therefore, able to penetrate the BBB freely (Squibb and Index, 2008)(Lakshminarayana et al., 2015) and 80% to 90% of isoniazid penetrates the CSF (Davis., 2018). Isoniazid has proven potent bactericidal activity (Davis et al., 2018)(Mitchison, 2000). The CSF penetration of anti-infectives in humans is predicted by the ratio of the area under the concentration-time curve in CSF to that in serum (AUC_{CSF}/AUC_s) (Djukic et al., 2012). Isoniazid

has a logP value of -0.70 and is among some of the anti-infectives that achieve an AUC_{CSF}/AUC_S ratio close to 1.0 and is, therefore, a valuable drug for the treatment of CNS infections with susceptible pathogens (Nau et al., 2010). Rifampicin does not penetrate the BBB well. Rifampicin has a Mw of 822.9 g/mol and thus exceeds the Mw of 400 g/mol recommended to penetrate the BBB (Me, 2008). Rifampicin is however highly lipophilic (logP value of 2.7), and 80% of rifampicin is bound to plasma proteins (Sousa et al., 2008). Concentrations of rifampicin in the CSF are only 10% to 20% of those present in the plasma (Davis et al., 2018)(Donald, 2010). Thus, in plasma, most of the rifampicin is protein-bound and only the unbound portion is active, while in the CSF, very little protein is bound (Davis et al., 2018). Pyrazinamide is a hydrophilic therapeutic agent with a Mw of 123.11 g/mol and a logP value of -0.6 (Jenkin, 2017). Pyrazinamide has good CSF penetration (90–100%) (Davis et al., 2018); concentrations of pyrazinamide in the CSF are close to that of serum (Davis et al., 2018)(Donald, 2010). Approximately 10% of pyrazinamide is protein-bound (Jenkin, 2017).

The inclusion of ethambutol in the CNS TB treatment regimen has been debated as this drug exhibits the poorest BBB penetration even when the BBB is inflamed (Davis et al., 2018). Ethambutol (Mw 204.31 g/mol and logP value of -0.14), has CSF penetration of 20–30% (Davis et al., 2018)(Chiang and Starke, 2018). Increasing the dose and duration of treatment with ethambutol is not advised as this may lead to visual and neurological disturbances. Increased serum uric acid levels and acute gouty arthritis have been reported from the increased use of ethambutol (Allen, 2017).

There is, however, not enough information on how these drugs cross the BBB and the exact concentration-time profiles of these drugs in the CSF are also not clear.

2.3. Drug Delivery Across the BBB

Delivery of drugs to the CNS via the systemic route falls under two categories, i.e., invasive where deliberate access to the body is gained via incision, which may cause several complications such as damage to neurons and inflammatory reactions (Kasinathan et al., 2015). Invasive approaches require implantation of the devices such as osmotic pumps and depot formulations which therefore requires surgery and a sterile environment (Kasinathan et al., 2015). These techniques are therefore not suitable for chronic disease therapy such as in the case of HIV and TB.

Injection of drugs into the parenchyma of the brain (Figure 2.2A) is another example of an invasive technique. Disrupting the BBB with a hypertonic solution such as mannitol or using compounds such as bradykinin involved in the regulation of brain endothelial cellular junction can facilitate

drug delivery to the brain (Paul et al., 2019)(Dong, 2018). Temporal disruption of the BBB can be achieved through the infusion of hyperosmolar solutions of arabinose, saline, mannitol or urea into the internal carotid artery. This leads to a shrinkage of endothelial cells resulting in the formation of gaps in the endothelial junction (Kasinathan et al., 2015). Le and Blakley (2017) delivered gentamicin into the CSF of *in-vivo* guinea pigs by causing temporal disruption of the BBB through the administration of mannitol. The results showed that the rate of entry and exit of gentamicin was increased by mannitol through the blood labyrinth barrier significantly ($p = 0.0044$). The pharmacokinetic models for gentamicin showed no significant differences between the model without gentamicin and the model with gentamicin and mannitol ($p = 0.433$). This finding indicated that renal clearance of gentamicin from the blood was not altered by mannitol. The concentration of gentamicin in CSF and perilymph was always remarkably lower than that in blood (Le and Blakley, 2017). Focused ultrasound is another invasive delivery method of agents across the BBB. Focusing ultrasound in the area of interest with low intensity allows the reversible disruption of the BBB at target sites. There are currently no studies on the delivery of drugs for TB or HIV in the brain using focused ultrasound. Yang et al. (2012) developed an *in vitro* intracranial brain tumor model in NOD-*scid* mice using human brain glioblastoma multiforme 8401 cells to effectively deliver human atherosclerotic plaque-specific peptide-1 (AP-1)-conjugated liposomes containing doxorubicin (AP-1 Lipo-Dox) across the BBB. Yang and coworkers (2012) utilized pulsed high-intensity focused ultrasound (HIFU) to disrupt the BBB transcranially by delivering ultrasound waves in the presence of microbubbles. The authors reported that animals receiving drugs followed by pulsed HIFU presented with a significant accumulation of the drug in the tumor cells compared to control animals treated with injections of AP-1 Lipo-Dox or unconjugated Lipo-Dox (Yang et al., 2012). Focused ultrasound may be problematic in that it may cause subtle and elusive damage to DNA (Rosenblatt et al., 2020), may be time-consuming to administer, and may induce apoptosis (McMahon and Hynynen, 2017). Therefore, BBB disruption (Figure 2.2B) is not a preferred method of drug delivery. This technique causes the loosening of the tight junctions of the endothelium, allowing the movement of unwanted toxins into the brain in addition to the drugs.

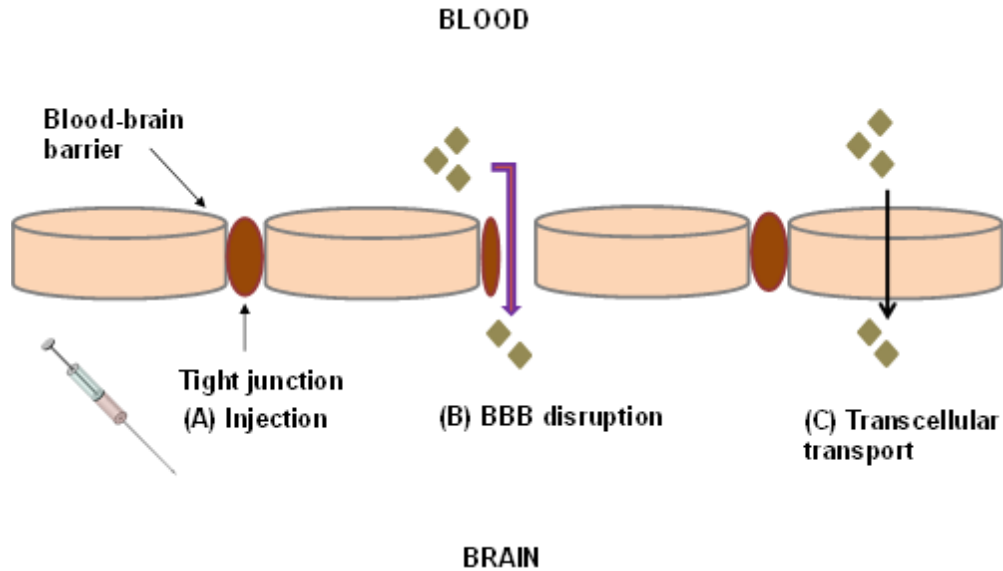


Figure 2.2. Strategies for crossing the BBB to deliver drugs. (A) Invasive approach: injection into the parenchyma of the brain is used to circumvent the BBB when treating patients. (B) BBB disruption is achieved by injection of chemical agents, osmolytes, or via focused ultrasound. This technique causes the loosening of the tight junctions of the endothelium, permitting access to the brain by conventional drugs. (C) Transcellular transport of drug molecules through a cell.

2.3.1. Noninvasive drug delivery approaches

Noninvasive approaches do not involve incision of the BBB, nor do they cause permanent alterations in the integrity of the BBB. Examples of non-invasive approaches that have been used for the delivery of drugs across the BBB include altering the solubility of the drug, NP drug delivery systems, chimeric peptides, enhanced transcellular transport, transport/carrier systems, Trojan horse approach, intranasal delivery, monoclonal antibody fusion proteins, peptidomimetics, immunophilins, efflux transporter inhibitors and prodrug approaches (Kasinathan et al., 2015)(Bellettato and Scarpa, 2018) (Table 2.1).

Chimeric peptides are a category of peptides and protein molecules that are coupled with suitable vectors (Kasinathan et al., 2015). The ability of chimeric peptides to impart properties from each “parent” protein to the subsequent chimeric protein has enabled their use in drug delivery (Kasinathan et al., 2015). Chimeric peptides are formed by the covalent coupling of a non-transportable peptide (e.g., beta-endorphin) to a transportable peptide that undergoes receptor- or absorptive-mediated transcytosis at the BBB (Das and Chakraborty, 2015). Immunophilins are

involved in processes such as protein folding, protein trafficking, receptor signaling, and transcription (Harikishore and Yoon, 2015) and these compounds display biological functions when complexed with their ligands (Harikishore and Yoon, 2015). Immunophilins are comprised of a family of conserved proteins which contain binding abilities to immunosuppressive drugs (Harikishore and Yoon, 2015). Hamilton (1998) reported that by binding with FK506-binding protein (FKBP), immunosuppressive agents, particularly tacrolimus and its analogues, could produce neuroprotective and neurogenerative effects. These small molecular immunosuppressive drugs are thus able to cross the BBB easily and are useful in treating brain and spinal cord injuries (Kasinathan et al., 2015). Peptidomimetics are small protein-like chains intended to mimic peptides (Deb et al., 2019). There are chemical modification methods that involve modifying the peptide structure to improve pharmacokinetic properties while simultaneously retaining a specific amino acid part(s) responsible for activity (Deb et al., 2019). The absorption of polar drugs can be achieved by increasing their hydrophobicity, however, the volume of distribution of the drug within the body will also increase (Kasinathan et al., 2015)(Jain, 2007). The transcellular pathway (Figure 2.3A) allows the passive diffusion of small, lipophilic molecules through the BBB and into the brain, while carrier-mediated transport (Figure 2.3B) is a type of facilitated transport that employs specific proteins to move molecules from the environment into and through the cell (Curley and Cady, 2018). Endocytosis and transcytosis (Figure 2.3C, D) are receptor-mediated drug delivery processes that aid in the uptake of molecules including drugs across the BBB (Kasinathan et al., 2015). Endocytosis and transcytosis are regulated by receptors including the insulin receptors, transferrin receptor, low-density lipoprotein receptor-related protein (LRP), neonatal Fc receptor present in the brain and the transferrin receptor (Kasinathan et al., 2015). Angiopep-2 is a synthetic peptide and a ligand for LRP1 receptors which is readily transported across the BBB. Conjugating drugs such as doxorubicin onto PEGylated oxidized multi-walled carbon nanotubes (O-MWNTs) modified with angiopep-2 (O-MWNTs-PEG-ANG) has been shown to enhance the uptake of doxorubicin into the brain (Ren et al., 2012). Endocytosis of materials can occur either through phagocytosis or pinocytosis (Kasinathan et al., 2015).

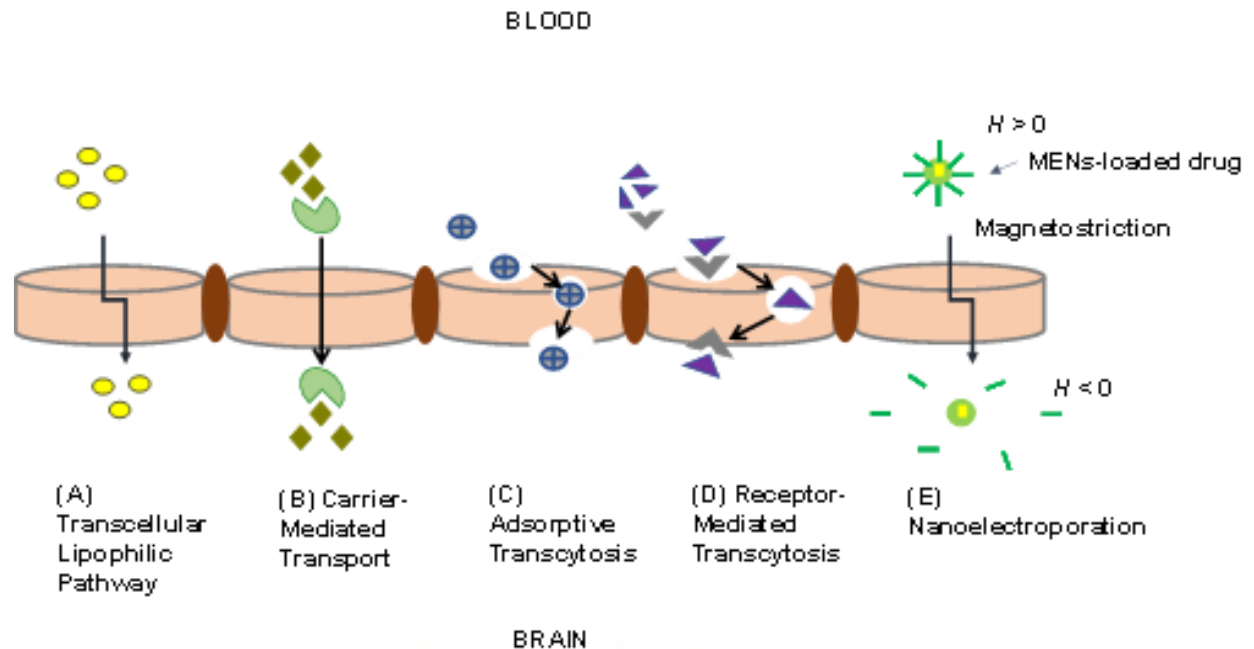


Figure 2.3. Illustration of transport pathways for BBB transport. (A) The transcellular lipophilic pathway allows the passive diffusion of small, lipophilic molecules across the BBB and into the brain. (B) Carrier-mediated transport employs specific proteins to move molecules from the environment into and through the cell. (C) Endocytosis of molecules via adsorptive transcytosis nonspecifically and transported through the cell. (D) Specific ligands bind receptors and are endocytosed and transported through the cell via receptor-mediated transcytosis. (E) Translocation of MENs across the BBB. Once MENs have been administered into the body, an externally applied magnetic field changes the shape of the inner core. Magnetostriction, changes the shape of the piezoelectric shell. The magnetic field induces the nanoelectroporation of the diseased cell (see Section 2.4).

Table 2.1. Non-invasive approaches for the delivery of drugs across the BBB.

Approach	Drug Delivered Across the BBB	Observations	Ref.
Intranasal drug delivery	α -L-idur-onidase (IDUA) encoding adeno-associated virus serotype 9 (AAV9) vector	Intranasal administration of α -L-idur-onidase (IDUA) encoding adeno-associated virus serotype 9 (AAV9) vector results in enzyme diffusion into deeper areas of the brain and reduction of tissue glycosaminoglycans storage materials in the brain.	(Belur et al., 2017)
Altered drug solubility	Doxorubicin	Conjugation of doxorubicin with angiopep-2 increased delivery of doxorubicin to the brain and showed good bioavailability and low toxicity.	(Ren et al., 2012)
NP drug delivery system	Zidovudine	Zidovudine was delivered via nanostructured lipid carriers into an <i>in vitro</i> human brain cell line (C6) and led to a significantly higher accumulation of the drug in the brain cells. The results suggest that these NPs could be a promising delivery system to enhance the brain uptake of zidovudine and other non-nucleotide ARVs.	(Joshy and Sharma, 2012)
NP drug delivery system	Atazanavir	<i>In vitro</i> delivery of atazanavir by solid lipid NPs into a hCMEC/D ₃ cell line demonstrated a significantly higher drug accumulation compared to the drug aqueous solution alone.	(Chattopadhyay et al., 2008)
Polymer drug conjugates	Ciprofloxacin	Increase in the uptake of PEGylated ciprofloxacin when the surfaces of the biologically active polymer core/shell NPs were modified with Tat peptide (TAT-PEG- <i>b</i> -Chol nanoparticles).	(Liu et al., 2008)
Peptidomimetics	HAYED peptide	A 16 lysine (K16) residue-linked low-density lipoprotein receptor-related protein (LDLR)-binding amino acid segment of apolipoprotein E (K16APoE) was used to deliver a therapeutic peptide (HAYED) into an Alzheimer's disease mouse model brain leading to reduced necrosis.	(Zou et al., 2019)
Viral vectors	Gadoteridol	Gadoteridol was co-infused with adeno-associated viral type 2 vectors and results showed that infusion of therapies directly into the disease- infected regions of the human brain with convection-enhanced delivery provides an effective strategy for treating neurological disorders.	(Su et al., 2010)
Trojan horse approach	HIRMAb-IDUA fusion protein	HIRMAb-IDUA fusion protein, also called valanafusp alpha has been administered to patients with mucopolysaccharidosis (MPS)	(Giugliani et al., 2018)

I. Patients were treated with HIRMAb-IDUA weekly by IV infusion for over a year. MPS I patients treated with HIRMAb-IDUA who suffered from severe mental retardation demonstrated stability in their IQ from further decline.



UNIVERSITY *of the*
WESTERN CAPE

The permeability of the BBB can be increased through use of pharmacological agents thus enabling cells to become more permeable. In view of the fact that the BBB controls material, nutrients and cell transfer from the blood to the brain and from the brain to the blood (Daneman and Prat, 2015)(Małkiewicz et al., 2019), vascular permeability is related to BBB permeability. Histamine and vasoactive peptides are agents responsible for inflammatory reactions causing a temporal increase in vascular permeability and vascular leakage (Abdulkhaleq et al., 2018). The vasodilator, bradykinin, increases vascular permeability by acting on bradykinin 2 receptors (Kasinathan et al., 2015). A 9-amino-acid peptide, labradimil (Cereport®; also known as RMP-7), is a formulated drug delivery system that shows selectivity for the bradykinin β_2 receptor designed to increase the permeability of the BBB. *In-vitro* studies have revealed that labradimil selectively binds to bradykinin β_2 receptor, has a longer plasma half-life than bradykinin, and initiates bradykinin-like second messenger systems such as an increase in the turnover of intracellular calcium and phosphatidylinositol (Emerich et al., 2001). Observations using electron microscopy showed that intravenous labradimil increases the permeability of the BBB by loosening the tight junctions of the endothelial cells (Emerich et al., 2001). The success of disrupting the BBB depends on the space created in the pores being large enough to permit the entry of molecules without damaging the structure of the cell (Kasinathan et al., 2015).

BBB pores are typically <1 nm; however, particles that are several nanometers in diameter can also cross the BBB via carrier-mediated transport (Balla and Goli, 2020). Any non-specific pores in the paracellular space nullifies the ability of the endothelial barrier to effectively regulate molecules and ions across the barrier. In essence passive permeability across the paracellular space would result in a short-circuit in the regulation of the BBB (Fisher and Mentor, 2020). Tight junctions have a size-selective permeability to uncharged particles of up to 4 nm and low permeability to larger particles (Daneman and Prat., 2015). This means that each tight junction forms a 4 nm pore and that molecules larger than 4 nm would pass through gaps in the junctions. NPs however may utilize a specific alternative lipophilic mechanism to cross the BBB (Fisher and Mentor, 2020). NPs larger than 4 nm can cross the BBB. Adams et al. (2007) successfully delivered fibrin γ 377–395 peptides conjugated to iron oxide (Fe_2O_3) NPs of 21 ± 3.5 nm in diameter to inhibit microglial cells in rTg4510 tau-mutant mice *in-vivo* (Adams et al., 2007)(Luo et al., 2020). Otani and Furuse. (2020) reported that the size-selective pathway of tight junctions is approximately 60 Å (equivalent to ~6 nm). The permeability of the BBB is more dependent on the molecular properties of the molecule than its size (Daneman and Prat., 2015). Small molecules can cross the BBB via lipid-mediated free diffusion, provided that they have a molecular weight

of <400 Da and form less than 8 hydrogen bonds (Bellettato and Scarpa, 2018)(Pardridge, 2020)(Islam et al., 2020)(Viscusi and Viscusi, 2020). Thus, lipophilic molecules can cross the membranes of the BBB even if their size is large. Typically, molecules less than 250 nm in diameter are taken up effectively by cells in the brain (Betzer et al., 2017)(Teleanu et al., 2018). However, the size of the NP that can cross the BBB greatly depends on the location of the brain (i.e., the pathway for crossing the BBB) and target tissue at the brain site (Teleanu et al., 2018).

2.3.2. Nanoporation

Nanoporation is a type of electroporation that generates very small holes (<2 nm) in plasma membranes (Roth et al., 2015). The pores formed are transient enabling transcellular drug uptake as opposed to an opening of tight junctions which is typical with non-invasive methods. Thus, there is no alteration of brain endothelial cells and the formation of gaps in the endothelial junction. Sridhara and Joshi (2014) studied the poration dynamics of lipid translocation driven by nanoporation due to multiple high-intensity (>100 kV/cm), ultrashort electrical pulses and to determine whether the pores, if formed, could remain open even after the electrical field had ceased. In their molecular dynamics (MD) simulations, the water–membrane system contained 37,157 water molecules and 512 dipalmitoylphosphatidylcholine (DPPC) lipid molecules for a total of 137,071 atoms in a 12.948 nm × 12.999 nm × 10.364 nm simulation box. The MD results displayed a gradual pore creation that began during the ‘ON-time’—start of the first pulse of the unruptured membrane patch. The existence of the first small nanopore was observed at the time (t) = 5 ns which grew larger by the 10 ns time instant. During the termination of the electrical pulse at 10 ns and 60 ns, the pore remained open without considerable changes or reduction. The pore was seen to be at its largest at the end of the second pulse. The results of this study coincide with the experimental study results of Pakhomov and colleagues (2009) using 600 ns pulses that have shown that nanopores are stable for many minutes. The use of multiple pulsing along with higher applied voltages could result in a larger pore density (Sridhara and Joshi, 2014). A larger pore density would be beneficial to pore coalescence and may promote the appearance of larger sized entry sites at the plasma membrane (Sridhara and Joshi, 2014). Sridhara and Joshi (2014) concluded that once nanopores are formed, they can remain open for long periods of time (there is no record of the duration of time the pores remained open in the study—the pore was still open at the beginning of the second electric pulse and there is no record of pore closure after $t = 70$ ns). The pore effects are expected to be much stronger with multiple pulsing. Nanopores that are stable for many minutes could significantly have an impact on cell electrolyte and water balance

(Sridhara and Joshi, 2014)(Mishra et al., 2017). Multiple nanosecond duration electric pulses (nsEPs) cause rapid cell swelling and blebbing (bulging out of the cell membranes), while substances such as digitonin (a mild detergent that permeabilizes plasma membranes) eradicates swelling and causes blebs to collapse (Pakhomov and colleagues, 2009). To date, most of the research has focused on controlled measurements using artificial lipid bilayer structures or indirect methods of nanoporation detection. Although both techniques provide useful insights, they are unable to directly detect and describe the dynamic nature of the poration and the recovery process in the affected living cells (Mishra et al., 2017)(Moen et al., 2016).

2.4. Nanoparticles and MENs

NPs are particles in the nanoscale range between 1 to 100 nm (in at least one dimension) whose properties vary depending on their size, surface area, uniformity, optical properties and functionalization (Lungu et al., 2015). NPs are effective delivery systems for a variety of payloads (Bellettato and Scarpa, 2018)(Shen et al., 2018). NPs are being investigated towards the delivery of drugs for infectious diseases (Dube, 2019). Apart from demonstrating good stability and tunability to carry cargo, NPs can cross biological barriers, providing controlled and sustained therapeutic effects at target sites (Patra et al., 2018).

Encapsulating drugs in suitable NP carrier systems can achieve higher drug concentrations at the target site (Figure 2.4.1). Nanospheres, nanocapsules and micelles are carriers that can be used to deliver drugs across the CNS (Kasinathan et al., 2015). Carriers should be biodegradable and should be able to deliver the drug at the specific site (Su and Kang, 2020). Polymeric NPs can be used to mask the physicochemical shortcomings of drugs to facilitate their transportation across biological barriers. Polymeric NPs accumulate in the brain via transcytosis (Ribovski, Hamelmann and Paulusse, 2021). In 2012, Kong and coworkers (2012) demonstrated that following systemic administration of magnetic iron oxide nanoparticles and application of an external magnetic field, the NPs were able to cross a mouse BBB via the transcellular pathway. Liposomal NP formulations can effectively cross the BBB due to their affinity for the lipid bilayer of the endothelial cell membrane (Song et al., 2021). Liposomal transport across the BBB occurs via the receptor-mediated transcytosis (RMT) and adsorptive-mediated transcytosis (AMT) pathways (Zhu et al., 2019). Conjugating metallic, polymeric and lipid NPs to targeting moieties facilitates their transcellular passage across the BBB by providing the following advantages: i) an increase in the stability of the NP, ii) a potential increase in the lipophilicity of the NP, iii) site-specific targeting and iv) endothelium uptake via RMT (Hersh, 2016).

Exosomes are becoming potential new brain-targeted drug delivery vectors for the treatment of CNS disease. These lipid biomolecular membrane vesicles with a diameter of 30 to 150 nm are secreted in all living cells and play a role in the diagnosis and treatment of TB infection (Chen et al., 2020). Jia et al. (2018) were able to effectively deliver superparamagnetic iron oxide NPs (SPIONs) and curcumin (Cur) into exosomes, and then conjugated the exosome membrane with neuropilin-1-targeted peptide via click chemistry and obtained glioma-targeting exosomes with imaging and therapeutic functions. The results of the study showed that the exosome complex could cross the BBB easily and further showed good results for targeted imaging and therapy of glioma (Jia et al., 2018). Exosomes have better drug loading capacity and lower immunogenicity compared to synthetic vectors with the ability to cross the BBB and demonstrate better targeting by membrane modification (Bellavia et al., 2017). Following transportation, the loaded drugs are released into the targeted cells through membrane fusion or endocytosis, in order to maximize the effect of the drug (Batrakova and Kim, 2015).

2.4.1. NPs as delivery systems for drugs across the CNS

2.4.1.1. Organic NPs as delivery systems for drugs across the CNS

2.4.1.1.1. Liposomes

Liposomes are showing promise as nanocarriers for drug delivery across the BBB. The size of liposomes ranges from 30 nm to 100 µm (Alexander et al., 2019). Liposomes can be divided into unilamellar vesicles (large and small unilamellar), multilamellar vesicles, and oligo-lamellar vesicles. A liposome can entrap hydrophilic compounds in the aqueous core and lipophilic compounds in the lipid bilayer (Figure 2.4.1). To assist drug targeting to the brain, liposomes are sometimes surface-modified with specific ligands or carrier molecules including glutathione, lactoferrin, monoclonal antibodies, polyethylene glycol and transferrin (Ross et al., 2018). Zheng et al. (2015) developed H102 peptide-loaded liposomes for intranasal delivery to the brain. Following intranasal administration, the concentration of H102 peptide loaded liposomes in the hippocampus was nearly three-fold larger than that of the solution group. In addition, the H102 liposomes increase the activities of choline acetyltransferase and insulin degrading enzyme and inhibited plaque deposition. These effects were observed in even lower dosages compared to the H102 intranasal solution (Zheng et al., 2015). Further, no toxicity on nasal mucosa was observed with the H102 liposome formulations. Asmari et al. (2016) developed donepezil loaded liposomes

and studied its brain targeting efficiency by comparing the drug concentration in rat brain and plasma. A significant increase in the bioavailability of donepezil loaded liposomes was observed in the brain following intranasal administration compared to conventional dosage forms and route of administration. Donepezil loaded liposomes were found to be stable with high encapsulation efficiency and displayed sustained release behavior (Asmari et al., 2016). Additionally, Xiao et al. (2019) synthesized ascorbic acid thiamine disulfide modified liposome to effectively achieve brain targeting of docetaxel through the glucose transporter 1 (GLUT1) and sodium ion-dependent vitamin C transporters. The authors reported an over three-fold higher brain uptake of docetaxel (Xiao et al., 2019).

2.4.1.1.2. Polymeric NPs as delivery systems for drugs across the CNS

The use of polymeric NPs as drug delivery carriers to the brain is also biologically favorable. Most polymeric NPs are biocompatible and biodegradable. The inert polymer, polyethylene glycol (PEG) can be covalently attached to the surface of NPs. The PEG coat is thought to reduce immunogenicity and limit the phagocytosis of NPs by the reticuloendothelial system, leading to increased blood levels of drug in the brain (Dikpati et al., 2012). The production and manufacturing of large-scale polymeric NPs is however, challenging (Ribovski, Hamelmann and Paulusse, 2021) (Muthu and Wilson, 2012). Studies have revealed that the coating of NPs with polysorbate surfactants result in the transport of drugs across the BBB (Dikpati et al., 2012). Most polymeric NPs are biocompatible and biodegradable.

NPs manufactured for brain targeting have typically used biodegradable polymers such as polylactic acid, chitosan, polylactic-co-glycolic acid (PLGA), polyacrylamide, polycaprolactone, poly(lysine) and poly (alkyl cyanoacrylate) (Alexander et al., 2019). Li et al. (2018) utilized PEG-PLGA nanoparticle to target the natural compound shikonin to the brain to treat glioma. The NP was coated with lactoferrin to improve targeting efficiency and higher drug targeting to the brain was demonstrated by the lactoferrin-modified NPs (Li et al., 2018). NPs coated with chitosan can also be used as carrier systems for drug delivery to the brain (Alexander et al., 2019). Fernandes et al. (2018) developed ascorbic acid conjugated chitosan NP for effective targeting of a dipeptidyl peptidase-4 enzyme inhibitor, saxagliptin. The study demonstrated 3.42 times higher area under the curve (AUC) in the brain than the plain drug (Fernandes et al., 2018).

2.4.1.1.3. Nanogels as delivery systems for drugs across the CNS

Nonogels are nanosized hydrogel, or chemically or physically cross-linked 3-dimensional network of polymers which swell in aqueous media (Li et al., 2017) (Figure 2.4.1). An increase in the water content of the hydrogel imparts excellent biocompatibility and facilitated drug diffusion from the swollen portion of the polymer (Li and Cui, 2008) (Alexander et al., 2019). Doxorubicin loaded pH-responsive PVA cyclo-(Arg-Gly-Asp) peptide (cRGD) decorated disulfide (SS) containing poly (vinyl alcohol) nanogels (cRGD-SS-NG) to target the human glioblastoma or tumor cells has been developed by Chen et al. (2017). The nanogel consists of disulfide and surface modification cycloRGD-peptide. In the study, the drug-carrier system was inactive in normal physiological condition and released the drug to the tumor site due to change in pH, thereby effectively targeting the drug (Chen et al., 2017). Warren et al. (2015) constructed biodegradable amphiphilic cationic nanogel (cholesterol- ϵ -polylysine nanogel) as a carrier system for brain delivery of triphosphorylated nucleoside reverse transcriptase inhibitor to treat HIV. The nanogel, made of cholesterol- ϵ -polylysine is said to decrease the unwanted peripheral side effect and neurotoxicity of the bioactive (Warren et al., 2015).

2.4.1.1.4. Dendrimers as delivery systems for drugs across the CNS

Nanosized dendrimers are attractive drug carrier systems for brain targeting. Dendrimers are highly branched, 3-dimensional shaped spheroidal, monodispersed, symmetric polymeric macromolecules with reactive groups on the surface (Yan et al., 2011) (Seo and Hawker, 2020) (Figure 2.4.1). Drugs can be loaded into the core of a dendrimer while the reactive ends allow for multifunctionality to improve drug loading ability (Alexander et al., 2019). Lu and coworkers synthesized arsenic trioxide-loaded Arg-Gly-Asp (RGD) -PEG-modified polyamidoamine (PAMAM) for targeting brain glioblastoma cells (Lu et al., 2018). The dendrimers modified with PEG decreased cytotoxicity to brain capillary endothelial cells (BCECs) in comparison to the unmodified PAMAM dendrimer. The dendrimer carrier system provided sustained drug release and a significant increase in the pharmacokinetic profile and therapeutic effectiveness of the drug (Lu et al., 2018). Furthermore, a fourth-generation transferrin modified PAMAM dendrimers for brain delivery of tamoxifen was developed by Li et al. (2012). A considerably higher drug loading and enhanced BBB permeation was observed in this study (Li et al., 2012).

2.4.2. Metallic NPs as delivery systems for drugs across the CNS

2.4.2.1. Metallic iron oxide NPs

Superparamagnetic iron oxide NPs (SPIONs) are chemically inert and possess properties such as biocompatibility, low toxicity, and potent magnetic and catalytic behavior (Vallabani and Singh, 2018). Iron oxide NPs in general offer easy tuning of surface properties and surface functionalization with the desired biomolecules (Vallabani and Singh, 2018). Their property of being chemically inert and easily tunable has enabled their use in imaging, biosensors, targeting and drug delivery.

Shi et al., (2016) established brain endothelial cells (b.End3) and astrocytes (C8-D1A) *in vitro* BBB model to determine the permeability of superparamagnetic iron oxide NPs as drug carriers across the BBB. The results from the study suggest a possibility to manipulate the penetration of superparamagnetic iron oxide NP (SPION) across the BBB via the creation of bioactive coatings (Shi et al., 2016). SPIONs coated with collagen, glycine and glutamic acid showed promising results for use in medication (Shi et al., 2016). The SPIONs coated with collagen were able to penetrate the BBB more significantly. It is suggested that they can be used for neural drug delivery applications (Shi et al., 2016). SPIONs coated with glycine and glutamine displayed limited BBB permeation, thus showing good possibility for use in drug delivery for minimizing neurotoxicity (because of their limited BBB penetration). Additionally, glycine and glutamine-coated SPIONs can be used in whole body magnetic resonance imaging (MRI) (Shi et al., 2016).

The use of an external magnetic field in combination with tight junction disruption in order to enhance the permeability of iron oxide NPs (IONPs) across an *in vitro* was examined by Sun et al., (2014). The results showed that none of the IONP formulations were permeable across intact cell monolayers. On the other hand, when the tight junctions were disrupted with D-mannitol, the 28% of the negatively charged N-(trimethoxysilylpropyl) ethylenediaminetriacetate [EDT]-IONPs were able to cross the bEND.3 cells monolayers. Further, penetration of EDT-IONPs across the monolayers increased to 44% in the presence of a magnetic field (Sun et al., 2014). Contrary to that, the permeability of positively charged aminosilane-coated [AmS]-IONPs after osmotic disruption was less than 5% (Sun et al., 2014). Cellular uptake of both the positively charged and negatively charged IONPs was not affected by the presence of mannitol (Sun et al., 2014).

Numerous studies have revealed that IONPs can induce toxic effects in vivo systems and *in vitro* cell cultures (Kilic et al., 2017). Other studies have showed that under specific conditions, depending on the surface properties and tested concentrations, IONPs can induce a number of

cytotoxic effects some of which include apoptosis, cell cycle alterations, and oxidative damage (Kilic et al., 2017).

2.4.2.2. Quantum dots

Quantum dots can be used as promising carrier systems for brain targeting. Ghaderi et al. (2011) have defined quantum dots as colloidal nanocrystalline semiconductor materials consisting of a metalloid crystal core and a nonreactive metallic shell covering the crystalline core (Figure 2.4.1). The inherent properties of quantum dots together with their small surface area enable the attachment of a wide variety of therapeutic and diagnostic agents (Alexander et al., 2019). Yang et al. (2017) utilized quantum dots to demonstrate their ability as promising diagnostic tools. Yang and coworkers used Cd-Se-Zns quantum dots, merged into pH-triggered polymeric micelle and used as fluorescent imaging nanoprobe to distinguish the region of the brain affected with cerebral ischemia (Yang et al., 2017). Likewise, Tang et al. (2017) designed a novel PEGylated quantum dot nanoprobe conjugated with aptamer 32 for fluorescent imaging of brain tumor. These NPs possess the ability to specifically bind to glioma cells and could therefore possibly be used as a promising contrivance for diagnosis, investigation, and surgical intervention of brain tumor (Tang et al., 2017) (Alexander et al., 2019).

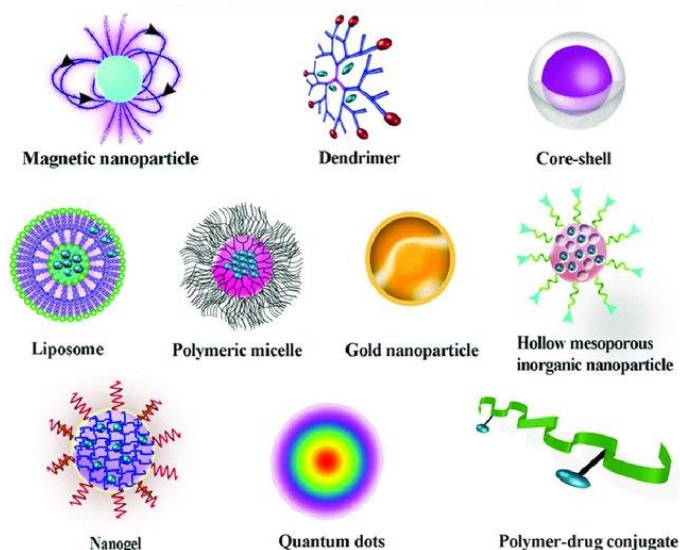


Figure 2.4.1 Schematic diagram showing different types of NPs (Karimi and Ghasemi, 2015).

MENs are a class of NPs that exhibit magnetic and electric properties that can be controlled utilizing magnetic and electric fields. MENs are typically 30 nm in diameter, however, these NPs can be as large as 600 nm (Hadjikhani et al., 2017). Calcination approaches have been investigated to determine the sizes of MENs. Hadjikhani et al. (2017) investigated the effect of alteration of calcination temperatures on the size of MENs. The authors reported that calcination at 600 °C resulted in 30 nm MENs, 700 °C for 100 nm MENs, 780°C for 200 nm MENs and 850 °C for 600 nm MENs. Thus, the higher the calcination temperature, the larger the size of the MENs (Hadjikhani et al., 2017). MENs are comprised of a lattice crystal structure with a magnetostrictive cobalt ferrite (CoFe_2O_4) core surrounded by a barium titanate (BaTiO_3) piezoelectric shell. The tetragonal crystal structure of the BaTiO_3 shell and the cubic structure of the CoFe_2O_4 core has been shown using X-ray diffraction (XRD) (Stimphil et al., 2017). Microscopy images of MENs show an irregular-sphere-like morphology (Pandey et al., 2021)(Corral-Flores et al., 2010). MENs offer advantages in that they are able/show potential to (i) achieve targeting driven by an external magnetic force, (ii) provide on-demand externally controlled drug release and (iii) provide image-guided precision drug delivery (Stimphil et al., 2017). These properties are advantageous towards drug delivery in the CNS for TB and HIV.

Externally applied magnetic fields can change the shape of the inner core of MENs. This phenomenon is known as magnetostriction and changes the shape of the piezoelectric shell (Figure 2.3E). The change in the shape of the piezoelectric shell creates an electric field at the surface of the MEN which induces temporal nanoelectroporation of the cells whereby holes less than 2 nm in the cell plasma membranes contributing to enhanced drug permeation and uptake of MENs in the diseased cells (Das and Chakraborty, 2015)(Zhang et al., 2021). From the literature, it is unclear whether phagocytosis/endocytosis is also a major uptake route for MENs, or whether MENs also transiently alter the size of the paracellular tight junctions across the BBB. The greater the magnetic field, the greater the electric field that is produced (Khizroev et al., 2018) (Guduru et al., 2013). Typically, diseased cells have a different electroporation than normal cells and, have a lower threshold for electroporation and are therefore more permeable when exposed to an electric field (Khizroev et al., 2018) (Guduru et al., 2013). Electroporation has been detected using dyes (fluorophores or color stains) or functional molecules by measuring the efflux of biomolecules, monitoring cell swelling and through conductivity measurements, impedance measurements and voltage-clamp techniques (Napotnik and Miklavčič, 2018). Any other

substance present at the blood-side of the BBB would also be taken up across the cells due to the altered permeability. Drug release has been described to be achieved through “shaking off” of the drug on the MENs as the induced alternating magnetic field shifts the magnetic dipole of the particle the drug is released intracellularly (Figure 2.4.2) (Khizroev et al., 2018).

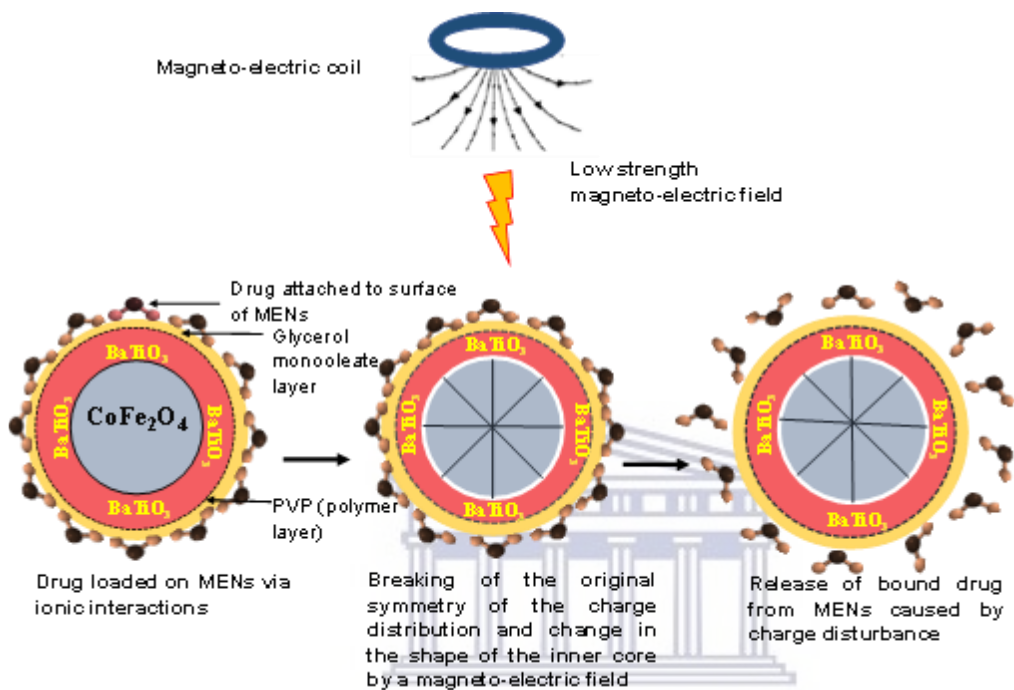


Figure 2.4.2. Schematic diagram of the effect of an applied magneto-electric field on core-shell MENs. MENs surrounded by a polyvinylpyrrolidone (PVP) polymer layer and glycerol monooleate layer with a drug loaded on the surface of MENs. Upon the introduction of low strength magneto-electric field, the original symmetry of the charge distribution breaks and the shape of the inner core of MENs changes (i.e., magnetostriction) and changes the shape of the piezoelectric shell resulting in the release “shaking off” of the drug bound to MENs caused by charge disturbance.

2.5. Synthesis and characterization of MENs

2.5.1. The co-precipitation method

Co-precipitation is an established synthesis method of NPs in aqueous solution (Varanda et al., 2019). Co-precipitation methods are used to obtain a uniform composition of two or more cations homogenous solution through a precipitation reaction (Liu et al., 2019). Co-precipitation is a useful method for the synthesis of composites containing two or more kinds of metal elements (Liu et al., 2019). The synthesized magnetic core is then coated with a ferroelectric material by a sol gel

method. These NPs are coated with polymers such as PNIPAm through radical polymerization. PNIPAm was selected by Lui et al. (2019) due to its pH-sensitive properties, and lower critical solution temperature (the temperature of phase change of PNIPAm is independent of molecular weights and concentrations at least in the range of 1 wt%). PNIPAm also shows reversible hydration and dehydration accompanied by dynamic conformational changes in the polymer chains by temperature change (Akiyama and Okano, 2015). In addition, this polymer molecule behaves as a flexible coil from the molecular weight dependence of these parameters (Akiyama and Okano, 2015). Advantages of co-precipitation methods include a high yield, high product purity, easily reproducibility, low cost, lack of necessity to use organic solvents, uses low temperature for simple and rapid preparation, energy efficient, easy control of particle size and composition, does not involve the use of organic solvents, offers various possibilities to modify the particle surface state and overall homogeneity (Rane et al., 2018). A limitation of the use of this method is that it is time-consuming, batch to batch reproducibility problems, does not work well if the reactants have very different precipitation rates, not applicable to uncharged species and trace impurities may get precipitated with the product (Rane et al., 2018).

2.5.2. The hydrothermal method

Another synthesis method was described by Stewart et al. (2018) for the delivery of antitumor peptides into glioblastoma cells. In this method, CoFe_2O_4 core particles were synthesized by a hydrothermal method. Cetyl Trimethyl Ammonium Bromide (CTAB) and Iron nitrate $\text{Fe}(\text{NO}_3)_3 \cdot 9\text{H}_2\text{O}$ were measured in equal quantities and dissolved in 70 mL of deionized water. Afterward, the contents were magnetically stirred for 5 minutes, then a stoichiometric amount of $\text{Co}(\text{NO}_3)_2 \cdot 6\text{H}_2\text{O}$ was added to the mixture and stirred for 10 minutes (Pervaiz et al., 2013). Next, a sodium hydroxide (NaOH) 6M solution was added and stirred vigorously for 10 minutes. The mixture in solution was placed in an ultrasonic water bath at room temperature for 15 minutes (Pervaiz et al., 2013). Thereafter, the mixture was poured into a Teflon-lined stainless steel autoclave of 100 mL capacity (Pervaiz et al., 2013). Without any stirring, the autoclave was placed in an electron oven at a temperature of 160 °C for 12 h. The autoclave was cooled to room temperature. The black precipitates were filtered out and washed numerous times (Pervaiz et al., 2013). The precipitates were dried at 80 °C overnight to obtain the powder (Pervaiz et al., 2013). The size distribution of MENs was confirmed using an atomic force microscope (AFM) imaging to assess grain height. Hydrothermal synthesis methods have many advantages in that it enables the synthesis of NPs which are not stable at elevated temperatures (Gan et al., 2020). NPs with

high vapour pressures can be produced by hydrothermal method with minimum loss of particles, the compositions of NPs to be synthesized can be well controlled through liquid phase or multiphase chemical reactions (Gan et al., 2020). The disadvantages of the hydrothermal method include the need to use expensive autoclaves, safety issues during the reaction process and the impossibility of observing the reaction process (black box) (Asim et al., 2014).

2.5.3. Characterization of MENs

Size, shape, structure, ζ - potential and magnetic moment are critical components of MENs that need to be measured. The recommended tool of measurement of MENs is the transmission electron microscope (TEM). The TEM has previously been used to confirm the structure and gives detail about the size distribution of the nanoparticle of the NPs (Stewart et al., 2018). This technique of measurement is useful as it will determine whether the size of the NP can be distributed through the blood-brain barrier for deposition into the disease-infected cells in the brain. TEM images of MENs show that MENs have an irregular-sphere- like morphology with an average size of 25 ± 5 nm (Pandey et al., 2020). The release kinetics and integrity of the drug following the magnetic field application can be measured using an AFM, mass spectrometry, Fourier transform infrared spectroscopy, and XRD (Amiz, 2017) (Islam et al., 2020). XRD is used to measure crystalline structure, the nature of the phase, lattice parameters, and crystalline grain size. Pandey and coworkers (2020) have used XRD to analyze the structure of MENs which have been confirmed to be crystalline and composed of CoFe_2O_4 and BaTiO_3 . XRD images further show that for each MENP, the magnetostrictive CoFe_2O_4 core is surrounded by a BaTiO_3 piezoelectric shell (Pandey et al., 2020). Size and ζ - potential can be measured with the use of dynamic light scattering (DLS). Through the use of DLS, ζ - potential measurements in 10 mM PBS (pH 7.1) solution, the mean ζ - potential of MENs was estimated to be $- 23.5 \pm 5.8$ mV (Pandey et al., 2020). Further, it has been reported that the ζ - potential of MENs becomes more negative after applying a direct current magnetic (B) field (Betel et al., 2016). Up to a 30% increase in ζ - potential of MENs was observed when the magnitude of the magnetic B field increases to 100 Oe (Pandey et al., 2020). A vibrating sample magnetometer was used to show the magnetic moment/coercivity (the ability of a ferromagnetic material to withstand an external magnetic field without becoming demagnetized) of CoFe_2O_4 core as well as that of core-shell particles (Stewart et al., 2018).

Piezomagnetic force microscopy can be used to assess magnetic response due to the external magnetic field. Scanning electron microscopy, transmission electron microscopy, and

piezoresponse force microscopy can be used to assess the morphology and topography of the MENs (Stewart et al., 2018). *In vitro* cytotoxicity assay can be measured using a colorimetric assay. *In vitro* studies should include atomic force microscopy (AFM)/ magnetic force microscopy (MFM) and scanning tunneling spectroscopy (STS) imaging of the NPs to understand their magnetic-field-dependent electric properties. Confocal and fluorescent microscopy can be used to measure cellular drug uptake under varying magnetic field strength (Amiz, 2017). Heat-dissipation experiments can be measured using infra-red camera after field-treatment (Rodzinski et al., 2016). Infrared spectroscopy measures the wavelength and intensity of the absorption of infrared light by a sample (Fujioka, 2011).

Although most MENs are approximately 30 nm in diameter (Nair et al., 2013) (Sagar et al., 2014) (Rodzinski et al., 2016), according to Yue et al. (2012), MENs must be less than 20 nm in order to penetrate the BBB for neural stimulation *in vivo* for delivery of the nanoparticle drug-complex to the specific regions of the brain (Yue et al., 2012).



Table 2.2. Techniques used to characterize the physicochemical properties of MENs.

Technique	Physicochemical properties characterized
Dynamic light scattering (DLS)	Extracts information about the Brownian Diffusion Coefficient (and hydrodynamic sizes) of NPs dispersed in a liquid phase (Zhang et al., 2020). DLS can also be used to measure aggregation state, biomolecular conformation, ζ - potential and PDI of particles.
Transmission electron microscopy (TEM)	Uses energetic electrons to give information about the morphology, crystallography, composition and confirmation of particle size of the samples.
X-ray Diffraction (XRD)	Commonly employed to characterize the crystalline phases present in a material and disclose information about the chemical composition (Guccione et al., 2021).
Atomic force microscopy (AFM)	Enables the imaging of a surface to measure and localize different forces which include strength, adhesion, magnetic forces and mechanical properties (Malwela and Sinha Ray, 2014).
Scanning electron microscopy (SEM)	Creates an image by scanning a focused beam of high-energy electrons over a surface. The interaction between the electrons in the beam and the sample produces signals that are used to obtain information about the surface topography and atomic composition of the specimen (Subramanian, 2019)(Reigoto et al., 2021).

2.6. *In vitro* models of the BBB and determining drug uptake across the BBB

Human immortalized endothelial cell lines (hCMEC/D3) and bEND5 cell lines are typically used *in vitro* cell lines. hCMEC/D3 cell lines are prepared from cerebral microvessel endothelial cells. hCMEC/D3 represent stable, easily grown BBB cellular model in drug discovery for drug uptake, active transport and drug permeability, screening of CNS drug candidate and brain endothelium biology study during inflammatory stimuli or infectious disease (Tetu, 2016). An hCMEC/D3 BBB cell line forms a spindle-shaped, elongated morphology similar to primary culture of brain endothelial cells (Tetu, 2016). It demonstrates contact inhibition at confluence when cultured on collagen type I or IV expressing brain endothelial biomarkers with adherence, tight junction proteins and functional ABC transporters (Tetu, 2016). Under optimized cell culture conditions, hCMEC/D3 cells are able to maintain unique BBB properties until the 35th subculture (Tetu, 2016). The hCMEC/D3 cell line is well characterized and easy to use. These cells convey functional efflux transporters (ABC transporters because they contain ATP-binding cassette (s) for active transport), for brain endothelium as observed in freshly isolated human brain microvessels, including P-glycoprotein, breast cancer resistance protein, and multidrug resistance-associated proteins (MRP) -4 and -5 (Weksler et al., 2013). hCMEC/D3 cells express MRP-1 with primary human brain endothelial cells in culture thus suggesting that *in vitro* culturing may non-physiologically induce the expression of this gene (Weksler, Romero and Couraud, 2013). hCMEC/D3 monolayers display restricted permeability to lucifer yellow (a low molecular weight diffusion marker) and to various hydrophobic and hydrophilic low molecular weight drugs which as demonstrated by Weksler et al., (2005) correlate with *in vivo* permeability coefficients (Weksler, Romero and Couraud, 2013). hCMEC/D3 monolayers also show restricted permeability to low and high molecular weight dextrans that are similar to primary CECs and lower than non-cerebral endothelium, especially under conditions of flow (Weksler, Romero and Couraud, 2013). The permeability profile of compounds of MW>4000 is similar to that of bovine and porcine CECs. Extracellular stimuli and stress conditions have been shown to increase paracellular permeability of hCMEC/D3 via signaling pathways such as JNK, PKC or NFκB (Weksler et al., 2013), including oxygen and glucose deprivation, mannitol treatment and pro-inflammatory cytokines such as TNFα and CCL₂ chemokines (Weksler et al., 2013). Its low junctional tightness is a challenge for its use for vectorial transport of small molecule compounds and requires further optimization (Helms et al., 2016). On the other hand, hCMEC/D3 cell lines are stable and consist of easy grown and transferable population of human microvascular CEC that maintains a stable BBB phenotype (Weksler et al., 2013).

BEnd5 cell lines are well characterized for the expression of endothelial cell specific proteins, namely claudin-5, endoglin, platelet endothelial cell adhesion molecule-1, ICAM-2, vascular endothelial-cadherin and von Willebrand factor (Steiner et al., 2010)(Vinciguerra & Tagliatela, 2018). bEnd5 cells exhibit a spindle-shaped cell morphology and F-actin stainings show that F-actin of bEnd5 cells are presented as parallel fibers oriented longitudinally throughout the cell body (Steiner et al., 2010). bEnd5 cells do not form as tight a barrier as the primary brain endothelial cells, the transepithelial/endothelial electrical resistance (TEER) values are low, permeability measured by paracellular markers are considerably high compared to brain endothelial cells systems (Toth et al., 2019). The limitations of bEnd cells are the presence of incomplete tight junctions and poor barrier function (Jamieson et al., 2017). bEnd cells are however stable over numerous channels, commercially available and can be transfected to express human efflux pumps (MDCK) (Jamieson et al., 2017). Moreover, permeability experiments show that bEnd5 cells form a tight barrier that compares to well-established *in vitro* BBB models, such as the bovine brain endothelium cell model (BBMEC) (Mossu et al., 2019). bEnd5 cells have also been documented to be sensitive to hypoxia/glycemia treatment than BBMECs – hyperpermeability was seen in bEnd5 endothelial monolayer after short intervals of hypoxia/aglycemia compared to later time periods for BBMECs (Yang et al., 2007).

Persidsky et al. (1997) reported the development of an *in vitro* BBB model comprised of an upper and lower compartment separated by polyethylene terephthalate membrane with a pore size of 3µm. 2×10^5 human brain microvascular endothelial cells were grown to link on the upper side of the insert, the same amount were grown underneath. The extent of intactness of the BBB was measured using transendothelial electrical resistance (Guduru et al., 2013). The average transendothelial electrical resistance value individual BBB was approximately 150-200 ohms cm^{-2} and is thus consistent with the formation of BBB (Guduru et al., 2013).

The results of the *in vitro* BBB model study conducted by Kaushik et al. (2019) revealed that the release of Cas9/gRNA –nanoformulation bound to MENs across the BBB reduced HIV-LTR expression levels in latent HIV-1 infected cells (Kaushik et al., 2019). Furthermore, these results showed that the Cas9/gRNA release nanoformulation exhibits superior therapeutic efficacy in comparison to treatment with Cas9/gRNA on its own (Kaushik et al., 2019). The increased uptake of the nanoformulation bound moiety stems from electroporation and the ability of the nanoformulation to target latent HIV-1 genome showing good promise as therapeutic approach (Kaushik et al., 2019).

In addition, two endothelial cell lines: human brain endothelial capillary cell line (hCMEC/D3) and human brain microvascular endothelial cells (HBMVE) have been isolated, cultured and validated (Weksler et al., 2013). hCMEC/D3 are excellent *in vitro* models for studies of BBB function, responses of brain endothelium to inflammatory and infectious stimuli, and the interaction of brain endothelium tumor cells (Weksler et al., 2013)(Helms et al., 2016). hCMEC/D3 monolayers show restricted permeability to lucifer yellow and to numerous hydrophobic and hydrophilic low molecular weight drugs which correlate with *in vivo* permeability coefficients (Weksler et al., 2013). This model also shows a restriction in the permeability to low and high molecular-weight dextrans (Weksler et al., 2013). For compounds with a molecular weight greater than 4000, the permeability profile is similar to that of bovine and porcine CECs (Weksler et al., 2013). On the contrary, stress conditions and extracellular stimuli have shown to increase paracellular permeability of hCMEC/D3 cells via signaling pathways (Weksler et al., 2013).

According to Weksler and coworkers (2013) hCMEC/D3 cells maintain the expression of most receptors and transporters expressed *in vivo* at the human BBB including insulin receptor, Glut-1, BCRP, MDR1, MRP4, transferrin receptor. hCMEC/D3 cells also mimic metabolizing enzymes and TJ proteins (Weksler et al., 2013).

TEER can be used to calculate the electrical resistance of the barrier. TEER is a non-invasive technique for testing *in vitro* barrier tissue integrity. TEER measurements are performed by applying an alternating current (AC) electrical signal across electrodes placed on both sides of a cellular monolayer, thereby measuring the voltage and current to calculate the electrical resistance of the barrier (Elbrecht et al., 2016).

In this study, brain endothelial cell-based *in vitro* models (bEnd5 cell lines) will be used to test the permeability of MENs to the CNS. bEnd cells are useful models for evaluating BBB function, particularly the paracellular barrier (Watanabe et al., 2013)(Erickson, Wilson and Banks, 2020). MDCK cells can also be used to determine the permeability of MENs across the BBB. The increased tightness of the monolayer of the MDCK cells produces permeability values which correlate well with *in vivo* brain permeation thus imitating tight cell junctions (Reichel, 2010). In addition, an efflux ratio can be determined allowing the identification and rejection of compounds with strong recognition by the MDR1-glycoprotein drug efflux pump (Reichel, 2010).

2.7. Application of MENs to deliver drugs across the BBB

MENs have been investigated for drug delivery for CNS HIV. Nair et al. (2013) demonstrated the *in-vitro* on-demand release of zidovudine (AZTTP) from 30 nm $\text{CoFe}_2\text{O}_4 @ \text{BaTiO}_3$ MENs by applying a low AC-magnetic field. Nair et al. (2013) demonstrated that the MEN-AZTTP nanoformulation showed 100% drug release at low alternating current (44 Oe at 100 Hz) without losing drug integrity and further showed HIV-p24 inhibition *in vitro* with good transendothelial BBB transmigration efficiency. An *in vitro* BBB model made from layers of brain microvascular endothelial cells (BMVEC) on the one side and astrocytes on the other side was used in this study. Approximately 40% of the MENs-AZTTP could penetrate the BBB under low-energy DC-magnetic field, this is three times higher than the free drug (Nair et al., 2013). An AC-magnetic field generated through electromagnetic coils as external stimuli were used to demonstrate the on-demand release of AZTTP (100% at 64 Oe). The AC-magnetic field could cause polarization changes on the MENs surface bringing about the release of AZTTP without hindering efficacy. The authors also showed that AC-magnetic field stimulation on MENs produced a localized electric field and sufficient ultrasound to open the cell membrane pore and deliver the MENs-AZTTP complex intracellularly. According to an investigation performed by Kaushik et al. (2017) MENs (50 μg) and AC-magnetic field (60 Oe) do not affect the viability of brain microglial cells. In this study, the uptake of MENs into the cells was demonstrated through nanoelectroporation using AC-magnetic field stimulation. MENs were taken up by microglial cells without affecting the health of the cell (viability > 92%) following optimization of AC-magnetic field at 60 Oe at 1 kHz (Kaushik et al., 2017). Furthermore, focused ion beam transmission electron microscope (FIB-TEM) analysis of microglial cells demonstrated a non-agglomerated distribution of MENs inside the cell and no loss of their elemental crystalline characteristics (Kaushik et al., 2017). Pandey et al. (2020) demonstrated that MENs displayed enhanced cell uptake (via microglial brain cells) and controlled drug release. The authors further confirmed that the AC-magnetic field stimulated at 60 Oe confirmed the localized surface potential enhancement of MENs.

In another study, the delivery of Beclin1 siRNA across the BBB using MENs was demonstrated by Rodriguez et al. (2017) towards control of the inflammatory effect of HIV infection. $\text{CoFe}_2\text{O}_4 @ \text{BaTiO}_3$ NPs bound to small interfering ribonucleic acid (siRNA) targeting Beclin1 to cross the BBB and to decrease the neurotoxic effects of HIV-1 infection in the CNS brought by an on-demand release of siRNA using an *in vitro* primary human BBB model (Rodriguez et al., 2017). The result of this research showed that Beclin1 siRNA attached to MENs was released through AC-magnetic stimulation (Rodriguez et al., 2017).

MENs can be designed with a coating layer. As can be seen in chromites, ferromagnetic materials due to their magnetic nature, have a high tendency to agglomerate (Kamran et al., 2017) (Biehl et al., 2018). To avoid agglomeration, the NPs can be coated or dispersed in a non-magnetic matrix (Kamran et al., 2017). Coating layers consisting of either glycerol monooleate (GMO), polyethylene glycol, or poly-L-Lysine have been reported (Khizroev et al., 2018). Kaushik et al. (2019) reported the effective controlled on-demand release of a nanoformulation composed of clustered regulatory interspaced short palindromic repeat (CRISPR)—associated 9, also known as Cas9/gRNA bound with MENs across the BBB to inhibit latent HIV-1 infection in microglial (hµglia)/HIV (HC69) cells. This approach led to the eradication of latent HIV in the cells (Kaushik et al., 2019). While the above studies demonstrate efficacy *in vitro*, there are no studies demonstrating the effectiveness of this approach using *in vivo* animal models.

To date, no studies have been reported on the application of MENs for delivery of drugs for eradication of *M. tb* in a CNS infection model. However, from reports on the delivery and efficacy of HIV drugs such as zidovudine delivered using MENs, we can expect similar observations for TB drugs.



CHAPTER THREE

AIMS, HYPOTHESIS, OBJECTIVES, RATIONALE

3.1. Problem statement

Although anti-infective drugs effective against *M.tb* are known, the effective delivery of such drugs across the BBB remains a major challenge. There is, therefore, need to effectively deliver anti-infective drugs across the BBB, particularly for a drug such as ethambutol. MENs could effectively facilitate transport of drugs across the BBB to reach infected cells.

3.2. Aims

The aim of this study is to synthesize $\text{CoFe}_2\text{O}_4 @ \text{BaTiO}_3$ core-shell MENs and characterize their physicochemical properties, induction of nanoporation and capabilities to facilitate the uptake for an anti-TB drug (ethambutol as a model drug) across an *in vitro* model of the BBB.

3.3. Hypothesis

We hypothesize that $\text{CoFe}_2\text{O}_4 @ \text{BaTiO}_3$ core shell MENs will induce nanoporation on bEND5 cells leading to enhanced uptake of ethambutol across the cells.

3.4. Objectives

1. To synthesize $\text{CoFe}_2\text{O}_4 @ \text{BaTiO}_3$ core shell MENs.
2. To characterize the physicochemical properties of the MENs.
3. To characterize cytotoxicity and nanoporation of the MENs on bEND5 cells *in vitro*.
4. To determine the transportation of ethambutol across bEND5 cells in the presence of MENs.

3.5. Rationale

Anti-TB drugs penetrate the CSF at very low concentrations and are therefore unable to effectively eradicate neuro-resident bacteria in the brain. Treatment with conventional anti-TB therapy is achieved after several months of treatment while bearing a risk of side effects. In this study MENs

will be applied to anti-TB drugs for the first time. We anticipate that exposing the BBB cell lines to sub-nanosecond electric pulses will lead to the formation of pores (nanoporation) in the BBB cells. In this study, the presence of nanoporation will be characterized using an electron microscope. In previous studies, the drug has been coated on the surface of MENs, whereas in this study the uptake of an anti-TB drug will be determined in the presence of MENs. There is a great need for non-invasive drug delivery systems or TB drugs across the BBB. MENs promise to improve cell-targeted delivery thereby improving the treatment of CNS diseases without affecting other organs in the body. Treatment with MENs can be life-changing and improve the quality of life of patients diagnosed with CNS TB compared to treatment with conventional methods which present with side effects.



CHAPTER FOUR

SYNTHESIS AND CHARACTERIZATION OF MENs

4.1. Introduction

This chapter describes the synthesis of MENs and their characterization for size, ζ - potential, shape, magnetic properties and crystallinity. Various synthesis approaches have been employed to obtain the MENs. Two methods of synthesis were used in this study - hydrothermal and liquid phase evaporation (Stewart et al., 2018)(Hadjikhani et al., 2017). The methods of synthesis were chosen based on their ability to obtain ~30 nm MENs and the availability of equipment for synthesis. Various parameters of the synthesis methods were evaluated: calcination temperatures, heat rate, outer and inner core of gel, and probe sonication time. These NPs were used in the next set of studies, using an *in vitro* BBB model. We looked into characterizing the magnetic properties and crystallinity of the MENs. We looked particularly at the magnetic properties of MENs to determine if MENs can be navigated into a targeted region in the brain with a magnetic field, in this case *in vitro*. Using XRD, we were able to measure the crystallinity of the MENs to determine the orderly arrangement of the atoms. MENs were synthesized and characterized at the University of the Western Cape (UWC), Cape Town. Synthesis and characterization of these NPs was performed at the School of Pharmacy and Department of Biotechnology, respectively. Cell culture studies were carried out at the Department of Medical Biosciences. Work involving scanning electron microscopy was conducted at electron microscopy unit (EMU) at the Department of Physical Science, UWC. All work involving a KSL-1100x high furnace was performed at the Department of Chemistry, UWC. All work involving AFM and XRD was carried out at iThemba LABS, Cape Town.

4.2. Materials

Table 4.1. Materials used in the study.

Material	Manufacturer	Catalogue Number
Barium carbonate	Sigma-Aldrich® (Cape Town, South Africa)	513-77-9
Citric acid 99%	Sigma-Aldrich® (Cape Town, South Africa)	77-92-9

Cobalt (II) nitrate hexahydrate	Sigma-Aldrich® (Cape Town, South Africa)	10026-22-9
Ethanol (99%)	Kimix® (Cape Town, South Africa)	
Iron (III) nitrate nonahydrate	Sigma-Aldrich® (Cape Town, South Africa)	7782-61-8
Polyvinylpyrrolidone K60, 45% in water	Sigma-Aldrich® (Cape Town, South Africa)	9003-39-8
Sodium borohydride	Sigma-Aldrich® (Cape Town, South Africa)	16940-66-2
Titanium (IV) isopropoxide 97% solution	Sigma-Aldrich® (Cape Town, South Africa)	546-68-9
Tissue Culture		
b.END.5 cells	Sigma-Aldrich® (Cape Town, South Africa)	96091930
Dulbecco Modified Eagle's Medium (DMEM)	WhiteSci (Whitehead Scientific (Pty) Ltd)	12-719F
Phosphate buffer saline (PBS)	WhiteSci (Whitehead Scientific (Pty) Ltd)	BE17-517Q
Sodium pyruvate (1%)	WhiteSci (Whitehead Scientific (Pty) Ltd)	13-115E
Non-essential amino acids (1%)	BioWhittaker™ Lonza™	13-114E
Fetal bovine serum (FBS) (10%)	Sigma-Aldrich® (Cape Town, South Africa)	SV30160.02
Penicillin/Streptomycin amphotericin B mixture (1%)	Whitehead Scientific (Pty) Ltd	17-745E
Trypsin	WhiteSci (Whitehead Scientific (Pty) Ltd)	BE02-007E
Trypan blue stain (0.4%)	Lasec® (Cape Town, South Africa)	17-942E
Plastic consumables		

Disposable folded capillary cell (DTS1070)	Malvern Ltd, UK	DTS1070
Disposable plastic cuvette (12 mm square polystyrene, DTS0012)	Malvern Ltd, UK	DTS0012
12-well plates TC treated	Adcock Ingram (Midrand, South Africa)	30012
24-well plate TC treated	Adcock Ingram (Midrand, South Africa)	3524
Conical tubes (15 ml)	Biosmart Scientific®	PBIOCT15
Conical tubes (50 ml)	Sigma-Aldrich® (Cape Town, South Africa)	CLS430290-500EA
Eppendorfs 1.5 ml	Biosmart Scientific®	PBIOTM
b.End5 cell line	American Type Culture Collection (ATCC)	Gift from Medical Bioscience Department, University of the Western Cape

4.3. Methods

4.3.1. Synthesis of MENs (hydrothermal method)

MENs were synthesized by adapting the hydrothermal method developed by Stewart et al. (2018). The hydrothermal method was chosen because the synergistic effect of high temperature and pressure provides a one-step process to produce highly crystalline materials without the need of post-annealing treatments. A 0.5 g of $\text{Co}(\text{NO}_3)_2 \cdot 6\text{H}_2\text{O}$ and 0.16 g of $\text{Fe}(\text{NO}_3)_3 \cdot 9\text{H}_2\text{O}$ were dissolved in 150 ml of an aqueous solution. Sodium borohydride (0.9 g) and an aqueous mixture of polyvinylpyrrolidone (0.2 g) were added and stirred at 70 °C for 12 h. The precursor solution of BaTiO_3 was prepared by mixing 174 mg of BaCO_3 and 5 g citric acid with 240 μl of titanium isopropoxide in an ethanolic solution. CoFe_2O_4 cores were then added to BaTiO_3 precursor solution and sonicated until fully dispersed for approximately 2 h. The mixture was then heated at 90 °C with continuous stirring overnight until a milky opaque gel formed. The gel was placed in a KSL-1100x high furnace to calcine at 400 °C, 500 °C, 550 °C, 600 °C and 700 °C for 5 h with controlled temperatures to obtain the MENs. To determine the effect of furnace heating rate on MENs, the gels were calcined at 700 °C for 2 h under the following conditions: (a) heating rate of

1.8 °C min⁻¹ from room temperature to 350 °C; (b) heating rate of 1.5 °C min⁻¹ from 350 °C to 700 °C and (c) cooled at a rate of 4 °C min⁻¹ from 700 °C to room temperature.

4.3.2. Synthesis of MENs (liquid phase evaporation method)

MENs were synthesized by utilizing the method developed by Hadjikhani et al. (2017). Co(NO₃)₂•6H₂O (0.5 g) and 0.16 g of Fe(NO₃)₃•9H₂O were dissolved in 150 ml of aqueous solution. Sodium borohydride (0.9 g) and an aqueous mixture of polyvinylpyrrolidone (0.2 g) were added dropwise to the above solution and the mixture was stirred at 120 °C until the solution evaporated. After the solution had evaporated, the cores (CoFe₂O₄) were recovered, dispersed in distilled water and centrifuged thrice. The purified cores (CoFe₂O₄) were dried at 37 °C for 24 h and stored at room temperature for further use. The precursor solution of BaTiO₃ was prepared by mixing 174 mg of BaCO₃ and 5 g citric acid with 284 µl of titanium isopropoxide in an ethanolic solution. The BaTiO₃ precursor solution was then added to CoFe₂O₄ cores and sonicated until fully dispersed for approximately 1 h. The mixture was then heated at 70 °C until the liquid phase evaporated. A hard gel formed on the outer surface of the beaker, while a soft gel formed on the inner surface of the beaker. The different textures of gel were recovered as two separate samples (MENs Outer gel and MENs Inner gel). The gels were placed in a KSL-1100x high furnace to calcine at 600 °C for 5 h with controlled temperatures to obtain the core-shell of MENs.

4.4. Physicochemical characterization of MENs

Particle size and distribution of the MENs synthesized under the various synthesis conditions was measured using AFM imaging to assess grain height. Hydrodynamic size was measured alongside PDI and ζ- potential using dynamic light scattering techniques with the use of the Malvern Zetasizer (Malvern Instruments, Malvern, UK). TEM was used to assess the morphology and size of the MENs. The crystal orientations and the crystal structure of the BaTiO₃ shell and that of CoFe₂O₄ cores were confirmed by using XRD.

4.4.1. Size, polydispersity index, ζ- potential and shape

The hydrodynamic size, PDI and ζ- potential of each suspension of MENs was measured using a Malvern Zetasizer Nano-ZS90 instrument. MEN granules were weighed post calcination on an

analytical balance and dissolved in distilled water by vortex mixing at a concentration of 0.1 mg/ml. To measure hydrodynamic size and PDI, 1 ml of each solution of MENs was pipetted into a disposable cuvette cell (DTS0012), the cell was wiped clean of dust and fingerprints and the cell was analyzed at 25 °C. To determine ζ - potential, 0.8 ml of each solution of MENs was pipetted into a disposable cuvette cell (DTS1070), again, the cells were wiped clean and the cells were analyzed at 25 °C. The samples were measured for 30 runs and 3 samples of the same MENs solution were analyzed.

4.4.2. TEM analysis

A transmission electron microscope (FEI T20 TEM, Germany) was used to provide information on the morphology, crystallography, composition and confirmation of particle size of the samples. During TEM analysis, an energetic electron beam was used to interact with the MENs sample to form an image on a specialized camera. The MENs samples were able to withstand the electron beam and the high vacuum chamber that the samples were introduced to.

4.4.3. pXRD analysis

XRD analysis was performed using the Bruker AXS (Germany) instrument to determine the crystalline phases present in the MENs and to disclose information about their chemical composition. An X-ray beam was directed at a MENs sample, and the scattered intensity was measured as a function of the outgoing direction. Scattering occurs when the x-rays collide with atoms in a crystal (Hosseini et al., 2021). Bragg's law of diffraction was used to calculate the atomic layer distances (Ameh, 2019)(Hosseini et al., 2021). The diffraction pattern indicates the sample's crystalline structure (Ameh, 2019). The diffraction patterns of NPs are considerably broader than their bulk counterparts. The broadening of the pattern makes it possible to calculate the crystallite size (Ahsan et al., 2018).

4.4.4. AFM analysis

AFM was used to determine the particle size and grain height of the MENs. Samples were prepared by dropping 50 mg of MENs in 1 ml of deionized water onto glass slides. The slides were transported to iThemba Labs, S.A where they were analyzed using an AFM (Nano-Man V Atomic Force Microscope hybrid XYZ, cpi®, United Kingdom).

4.4.5. Determination of the magnetic properties and atomic forces of MENs.

The magnetic forces of MENs were tested on paper with the use of magnets. A blank A4 white paper was placed horizontally on top of a magnet on to which the post-calcinated MENs powder were placed on the upper side of the A4 paper.

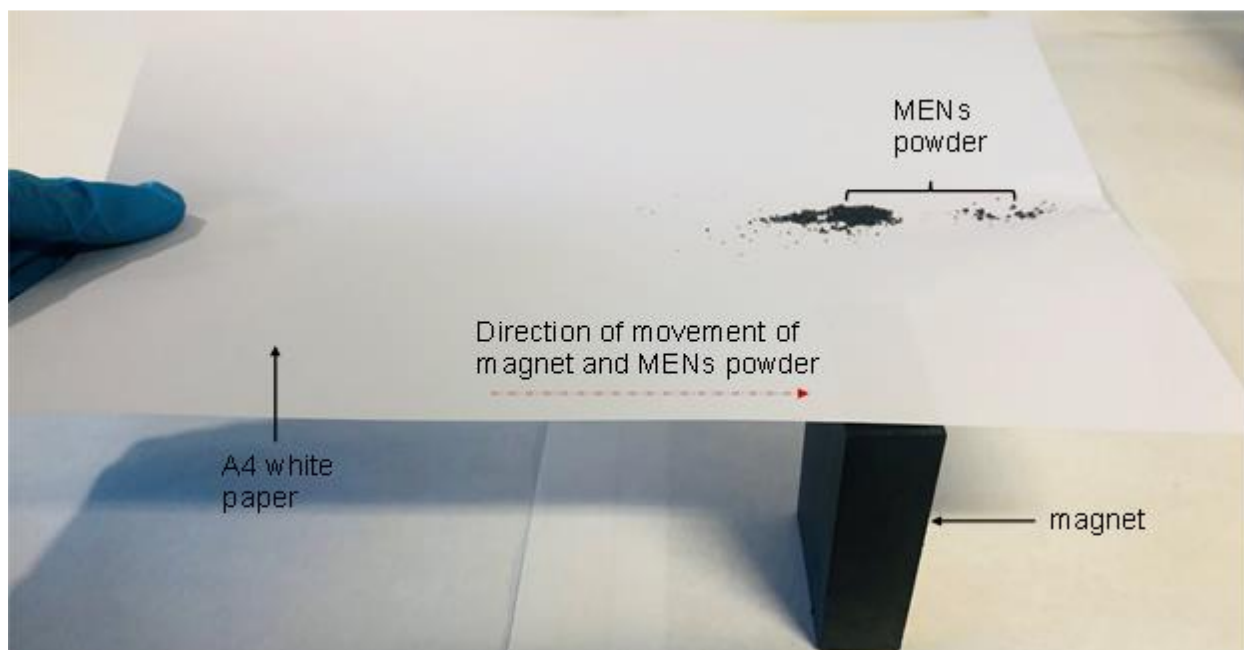


Figure 4.1. Magnetic test on paper. MENs powder on the upper side of blank A4 paper placed horizontally under a mobile magnet.

4.5. Statistical analysis

The data for particle size, polydispersity index (PDI) and ζ - potential is presented as the mean \pm standard deviation (SD). GraphPad Prism (version 8.4.2) was used to capture and analyze the data. One-way ANOVA analysis was used to perform a statistical comparison between set data groups. Two-way ANOVA analysis was used where necessary. The results of chemical synthesis methods are aggregates of experiments performed in triplicate; the p-values were calculated from the averages of each independent experiment. A p-value less than 0.05 indicates a significant

difference between the means of two groups (Kimulwo et al., 2017). The Tukey test (or Tukey's Honest Significant Difference test) in conjunction with an ANOVA was used to determine significant levels of the data. The degree of significance is represented by an asterisk (*) next to the p-value; $p < 0.05$ (*), $p < 0.01$ (**), $p < 0.001$ (***) and $p < 0.0001$ (****).

4.6. Results and discussion

4.6.1. MENs synthesized using the hydrothermal method

Physicochemical characterization of NPs is important in determining and predicting the biological behaviour of NPs (Canta M and Cauda V. 2020). These physical attributes namely: hydrodynamic size (nm), PDI and ζ -potential determine the efficacy, stability, safety, and the *in vitro* and *in vivo* behaviour of NPs (Danaei et al., 2018). The aim of this study was to synthesis 30 nm MENs according to literature (Stewart et al., 2018). MENs were synthesized according to the methods described in section 4.3 and each sample was read using the Malvern Zetasizer Nano ZS90 instrument where each sample was analyzed for hydrodynamic size, polydispersity index and ζ -potential (see section 4.3.1).

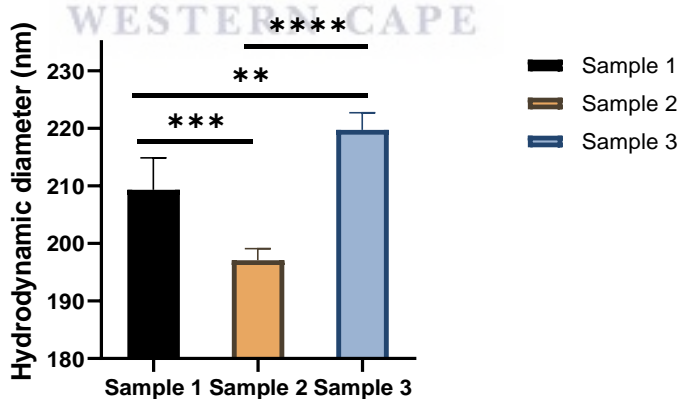


Figure 4.2. Hydrodynamic diameter (nm) of MENs synthesized by means of the hydrothermal method, in triplicate (sample 1, sample 2 and sample 3) calcined at 600 °C for 5 h. The degree of statistical significance is annotated with an asterisk (*); $p < 0.05$ (*), $p < 0.01$ (**), $p < 0.001$ (***) and $p < 0.0001$ (****).

All the samples were statistically significant. The average hydrodynamic diameter of MENs produced from the hydrothermal method of synthesis was 208.7 ± 4.30 nm.

Additionally, these samples (Figure 4.2) had good PDI values with an average PDI of 0.254 ± 0.025 . This value is suggestive of NPs which are monodisperse. In addition, these NPs had a good average ζ - potential reading of -34.41 ± 4.99 mV.

Three samples of MENs were produced in triplicate using the hydrothermal method of synthesis. These MENs were first calcined at 600 °C for 5 h, then read using the Malvern Zetasizer Nano ZS90 instrument where each sample was analyzed for hydrodynamic size, polydispersity index and ζ - potential. We expected the MENs to have an average size of 30 nm in accordance to reference articles of MENs. The average hydrodynamic diameter of MENs produced from the hydrothermal method of synthesis was 208.7 ± 4.30 nm. Furthermore, these samples had good ζ - potential and PDI readings i.e., -34.41 ± 4.990 mV and 0.254 ± 0.025 , respectively. A smaller ζ - potential results in particle aggregation and flocculation due to van der Waals forces of attraction between them which in turn result in physical instability, while a larger ζ - potential indicates that particles have sufficient repulsive forces to attain better physical colloidal stability (Ramli et al., 2021). From this explanation, we can deduce that the MENs in these samples (Figure 4.2) have good dispersion stability and are more likely to repel each other due the NPs having a large ζ - potential. From the results of the MENs produced during the hydrothermal method of synthesis, we can conclude that the MENs produced were stable and monodispersed based on the ζ - potential and PDI readings. Because we did not achieve a hydrodynamic diameter of 30 nm, we used the same method but changed the calcination temperatures (section 4.2.1) aiming to produce 30 nm MENs as suggested by Hadjikhani et al. (2017). We found that the MENs calcined at 600 °C still produced the smallest average hydrodynamic size (208.7 ± 4.30 nm) of NPs (Figure 4.4). The largest MENs hydrodynamic size (379.8 ± 35.38 nm) was obtained following calcination of the gels at 550 °C. The smallest MENs size produced during this method was larger than the MENs produced from the hydrothermal method. Furthermore, no linear relationship in the size of MENs was seen from calcinating the MENs gels at different temperatures and the DLS readings indicated that the MENs were greater than 30 nm in diameter.

Although DLS readings indicate that the hydrodynamic diameter of MENs synthesized during this first method of synthesis were larger than 30 nm, TEM and AFM images confirmed the presence of 30 nm MENs and the presence of MENs as small as 10 nm from these same samples (Figure 4.5). It is possible that smaller sized MENs clustered in suspension and were therefore 'visible' as larger sized particles under DLS analysis. In addition, it is possible that the MENs being

superparamagnetic may have enabled magnetization from the instrument to randomly flip the direction of MENs under the influence of temperature (Nagesetti et al., 2017)(Ganapathe et al., 2020). In the paramagnetic state, an external magnetic field is able to magnetize the NPs which resulted in the observation of larger sizes of MENs (Ganapathe et al., 2020). Alternatively, the differences in TEM and DLS sizes may have been a result of the Rayleigh theory. The Rayleigh theory states that the intensity of scattered light is proportional to the sixth power of the diameter and thus larger particles are given more weight, thus making the average size appear larger (Maguire et al., 2018). Both theories are possible, but the latter becomes more acceptable and is justified throughout the discussion in the sections below.

4.6.2. MENs synthesized using the liquid phase evaporation method

MENs manufactured from the liquid evaporation method produced a gel with different textures (Figure 4.3). The inner gel in the beaker was a runny liquid, while the outer gel seemed harder and rubber-like.

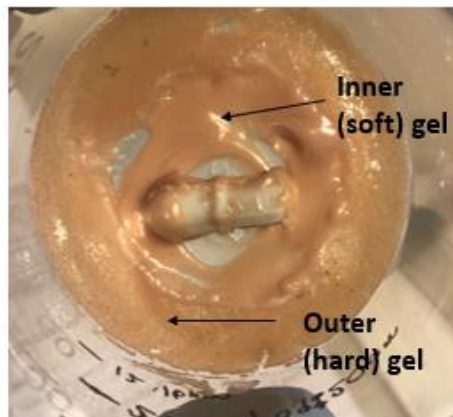


Figure 4.3. Gel recovered from the liquid evaporation method of synthesis of MENs. The inner gel appears soft in texture while the outer surface of the gel appears hard.

Table 4.2. Hydrodynamic size (nm), PDI and ζ - potential of MENs synthesized using the liquid phase evaporation method of synthesis under various conditions.

	MENs inner gel 20 min post probe sonication	MENs outer gel 20 min post probe sonication	MENs inner gel 1 hr 20 min post probe sonication	MENs outer 1 hr 20 min post probe sonication
Size (nm)	301.47 \pm 6.90	284.63 \pm 9.19	338.23 \pm 11.58	312.53 \pm 24.01
PDI	0.265 \pm 0.06	0.186 \pm 0.07	0.383 \pm 0.04	0.264 \pm 0.04
ζ - potential (mV)	-33.3 \pm 0.1	-30.73 \pm 0.25	-27.7 \pm 0.78	-33.67 \pm 1.78

The average size of the MENs inner gel increased from 301.47 nm upon probe sonicating for 20 min to 338.23 nm after probe sonicating for an hour and 20 min. The same can be seen with the MENs outer gel. Following probe sonication for 20 min, the MENs outer gel increased from 284.63 nm to 312.53 nm in size when the probe was sonicated for an hour and 20 min. The ANOVA test results from this study indicate that the MENs outer gel probe sonicated for 20 min are statistically significant ($p = 0.0084$) to the MENs inner gel probe sonicated for 1 h and 20 min. Further, these test results show no statistical significance between the rest of the groups ($p > 0.05$). The PDI values indicate that the MENs inner gel became less stable 1 h 20 min post probe sonication while the MENs outer gel became more stable 1 h 20 min post probe sonication. Good stability was observed when the MENs outer gel was probe sonicated for 20 min (-30.73 mV).

The average hydrodynamic size of the NPs produced from this method was larger than that produced from the hydrothermal method of synthesis. After 20 min of probe sonication, the inner gel had an average size of 301.47 \pm 6.90 nm, while the outer gel had an average size of 284.63 \pm 9.19 nm after the same period of probe sonication. The sizes of the NPs did not decrease after the NPs had been probe sonicated for an hour and 20 min (MENs inner gel: 338.23 \pm 11.58 nm, MENs outer gel: 312.53 \pm 24.01 nm). The PDI and ζ - readings signified that these MENs have good colloidal dispersion stability (Table 4.2). Based on the comparison of the two methods, we have concluded that the hydrothermal method of synthesis is the ideal method of synthesis as it was able to produce the smallest sizes of MENs.

4.6.3. The effect of calcination temperatures and heating rate on the hydrodynamic sizes of MENs

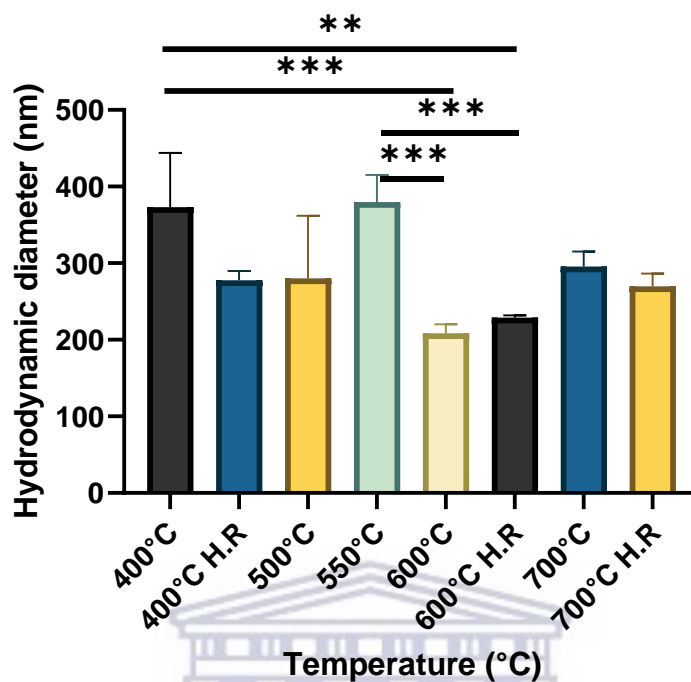


Figure 4.4. Average sizes (nm) of MENs calcined at different temperatures (°C) were measured using dynamic light scattering produced using the hydrothermal method of synthesis. H.R denotes MENs calcined using the heat rate method (see section 4.2.1). Statistically significant samples are annotated with an asterisk (*).

The smallest hydrodynamic NP size was 208.7 ± 11.32 nm obtained from MENs calcined at 600 °C for 6 h, followed by 228.93 ± 2.95 nm at 600 °C H.R. The largest NP size was 379.8 ± 35.38 nm at 550 °C. Results at 400 °C and 600 °C ($p= 0.0036$), 400 °C and 600 °C H.R ($p= 0.0115$), 550 °C and 600 °C ($p= 0.0024$), as well as 550 °C and 600 °C H.R ($p= 0.0078$) were statistically significant.

MENs calcined at 400 °C and 400 °C H.R were not statistically significant and therefore had a p-value of 0.1645. There was no statistical significance between MENs calcined at 400 °C and 500 °C, and those calcined at 400 °C and 550 °C. MENs calcined at 400 °C and 600 °C, and 400 °C and 600 °C H.R were significantly different (p-value of 0.0036 and 0.0115). MENs calcined at 550 °C and 600 °C ($p= 0.0024$), and 550 °C and 600 °C H.R ($p= 0.0078$) were significantly different in size.

Samples synthesized by altering the heat rate of the furnace were analyzed by use of the Malvern Zetasizer. The same effect discussed in section 4.5.2 may have been experienced during DLS analysis. Based on these findings, we decided to work with the MENs calcined at 600 °C for 5 h without the application of the heat rate method (sample 2) (Figure 4.2) as these MENs were the smallest average size (197.07 ± 2.45 nm) of the MENs we had synthesized.



4.7. Transmission electron microscopy of MENs.

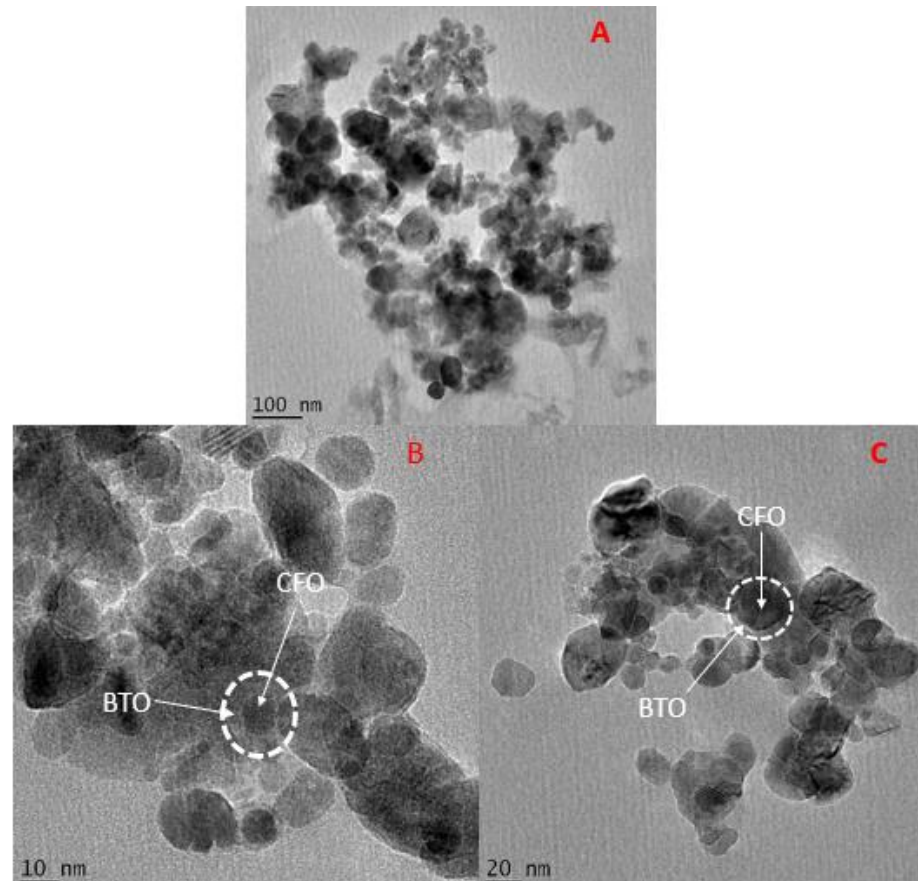


Figure 4.5. TEM images of the morphology of MENs at (A) 100 nm scale. The BTO (shell) and CFO (core) structure of MENs at (B) 10 nm scale and (C) 20 nm scale. A, B and C show that MENs vary in size from as small as 5 nm and showing an average of 36.5 nm (see Figure 4.6). The MENs are almost spherical with a dark inner core surrounded by a light outer shell.

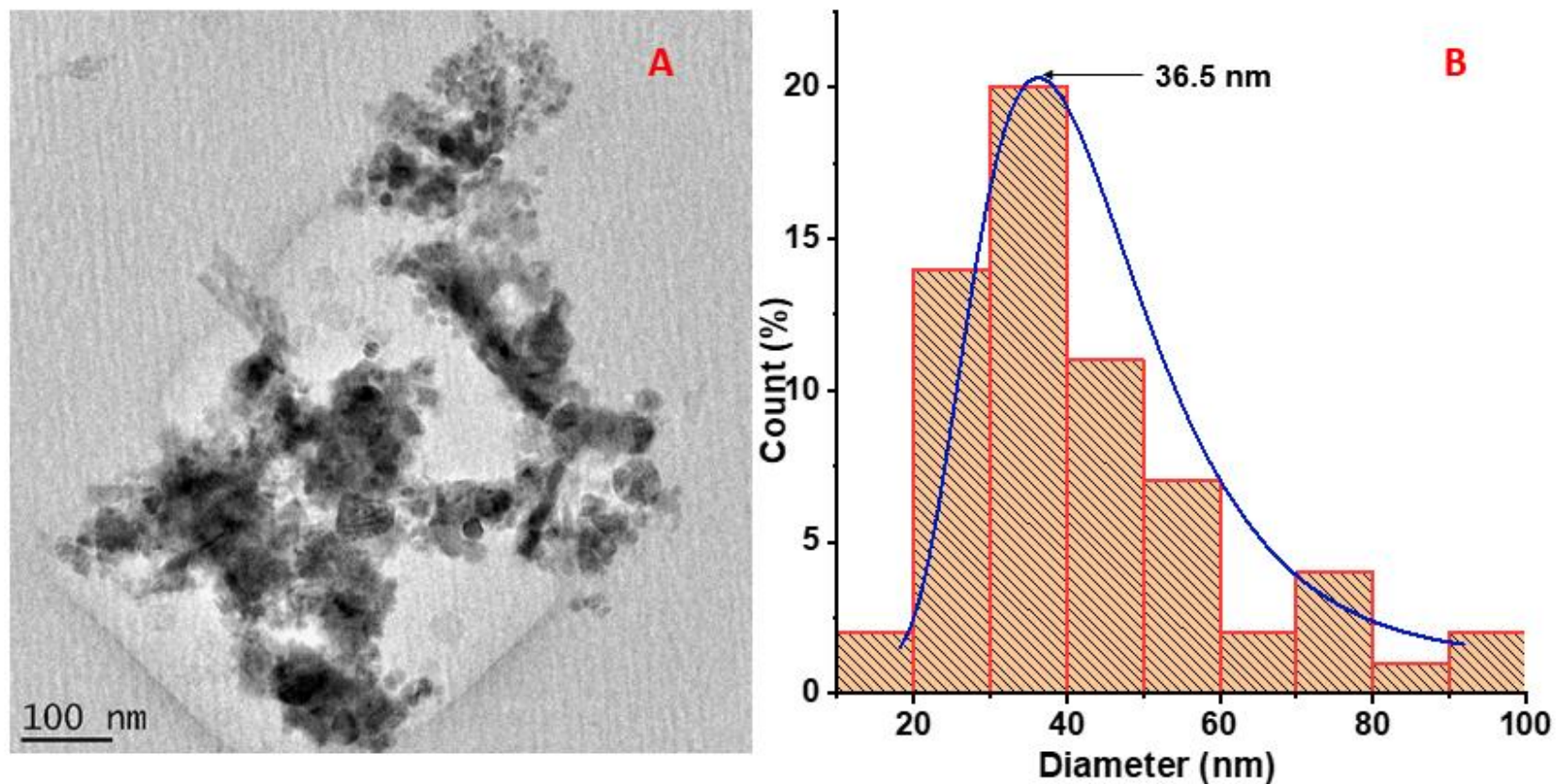
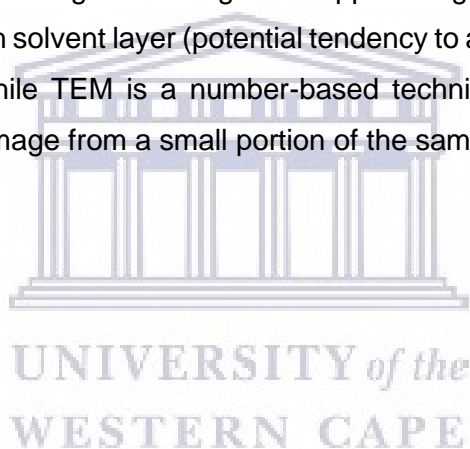


Figure 4.6. The morphology and average core-shell diameter of MENs. (A) TEM images of MENs at 100 nm scale, (B) the number size distribution of MENs measured using ImageJ Software.

TEM images of the MENs synthesized using the hydrothermal method calcined at 600 °C for 5 h showed that MENs of 5 nm, 20 nm and 100 nm in size were synthesized (Figure 4.5 A, B&C). These images also confirmed the BTO (shell) and CFO (core) structure of the MENs. The MENs in the images appeared clustered and spherical in shape (Figure 4.5 and 4.6 A). ImageJ Software was used to

determine the magnitude (%) of the diameter of MENs from the TEM image. The histogram data from the ImageJ Software (Figure 4.6 B) showed that the highest percentage (~20%) of the sizes of these MENs was an average of 36.5 nm. The second highest count (14%) showed that the MENs sizes were an average of 28 nm. 2.5% of the MENs were between 90 to 100 nm (Figure 4.6 B) and represented the largest NP size in the image. The size differences measured by TEM and DLS may have resulted from particle agglomeration thus giving larger DLS values than TEM. These NPs may have agglomerated in the aqueous solution while measuring DLS while TEM gives the sizes of NPs in dried form. DLS is an intensity-based technique and therefore puts more emphasis on larger particle sizes. According to the Rayleigh theory, the intensity of scattered light is proportional to the sixth power of the diameter and thus larger particles are given more weight, thus making the average size appear larger (Maguire et al., 2018). DLS gives an average particle size of all particles in solution and thus with solvent layer (potential tendency to agglomerate) including any artifacts or impurities present in the solution (Zhang et al., 2020). While TEM is a number-based technique and puts more emphasis on the smallest components in the size distribution, it shows an image from a small portion of the sample.



4.8. Atomic force microscopy of MENs

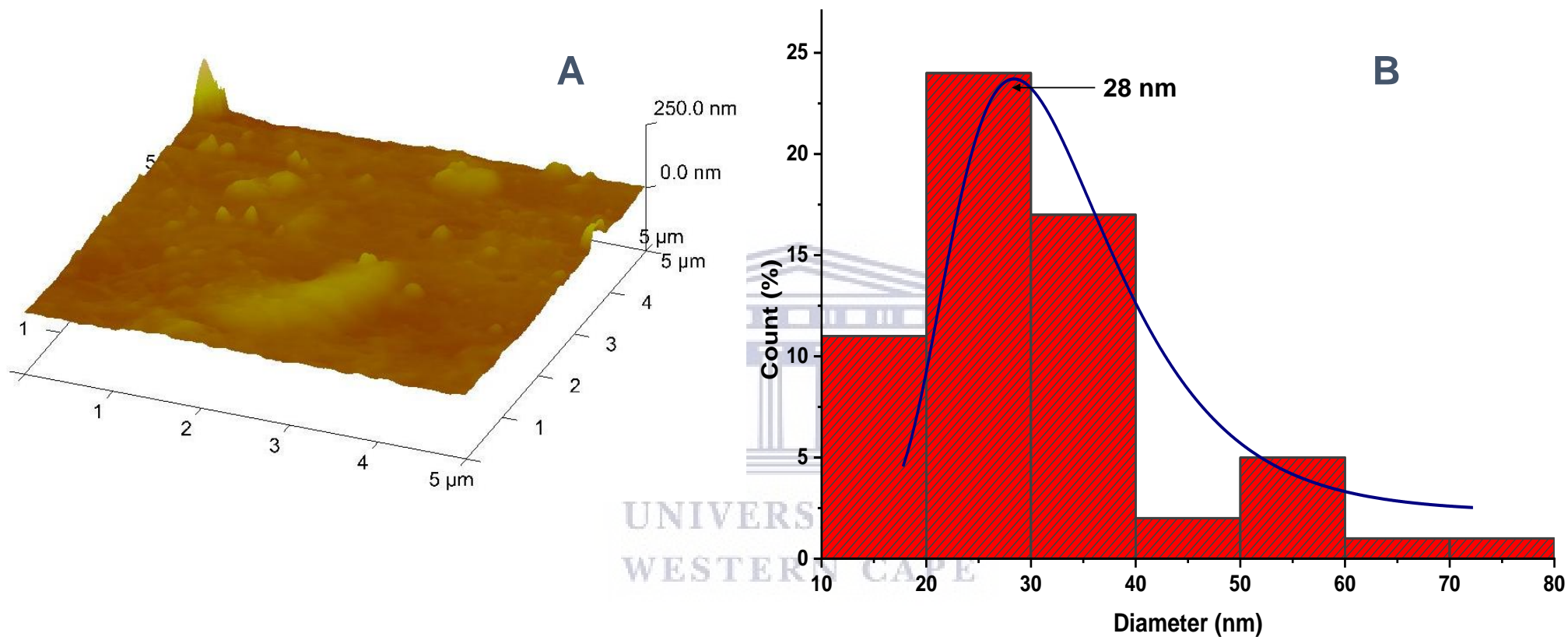


Figure 4.7. (A) AFM image of BTO (shell) CFO (core) MENs. The particle distribution of the MENs was inhomogeneous and most of the MENs had an almost spherical appearance which further confirmed the morphology and size distribution seen in the TEM images. (B) the number of size distribution of MENs measured using ImageJ software. From the AFM images, the average size of MENs was 28 nm and represented the largest percentage of the population.

The 3-dimensional AFM image of MENs (Figure 4.7A) showed that the MENs produced post-calcination were different in size. From the AFM image, we could clearly see the physical properties of MENs which included morphology, size, grain height, the texture of the surface, and surface roughness. Figure 4.7B confirmed that most of the MENs had an average size of 28 nm in diameter and represented 23% of the MENs in the sample which closely matches sizes observed from TEM. The scale in the image showed that the maximum grain height of the MENs was 250 nm. Though it was evident that some of the MENs were spherical, there were some MENs that were shaped like a Reuleaux triangle. Figure 4.7A also showed that these MENs formed ridges and had a very rough surface.

Electrostatic forces of MENs cannot be directly measured. They can only be measured using indirect methods. However, it is understood that the electrostatic strength decreases with increasing distance from the particles (Hu et al., 2018). Figure 4.7A showed that the MENs were in close proximity with each other, which meant that the MENs had very strong electrostatic forces between them. This supported the explanation by (Nagesetti et al., 2017) that MENs have a non-zero electric dipole and therefore the electric bonds between MENs and cells are expected to be strong.

4.9. Magnetic properties of MENs

The paper test (Figure 4.1) was used to evaluate the magnetic properties of MENs. MENs powder was placed on the upper side of the A4 paper and moved in the direction of the magnets that were placed on the bottom of the A4 paper (section 4.3.5). From this we concluded that MENs possess magnetic properties. This finding is in agreement with the work demonstrated by Guduru et al. (2015) and Stewart et al. (2018). Ideally an MFM is used to determine the magnetic properties of MENs. The paper test was used due to the unavailability of an MFM during this study. MFM is a method used to study the surface magnetic properties of materials. MFM is a type of AFM that uses a sharp magnetized tip to scan a magnetic sample. The interaction between the tip and the magnetic sample is detected and used to reconstruct the magnetic structure of the surface of the sample. The light regions indicate repulsion while the dark regions indicate attraction forces experienced by the MFM magnetized tip (Betal et al., 2016).

4.10. XRD analysis of MENs

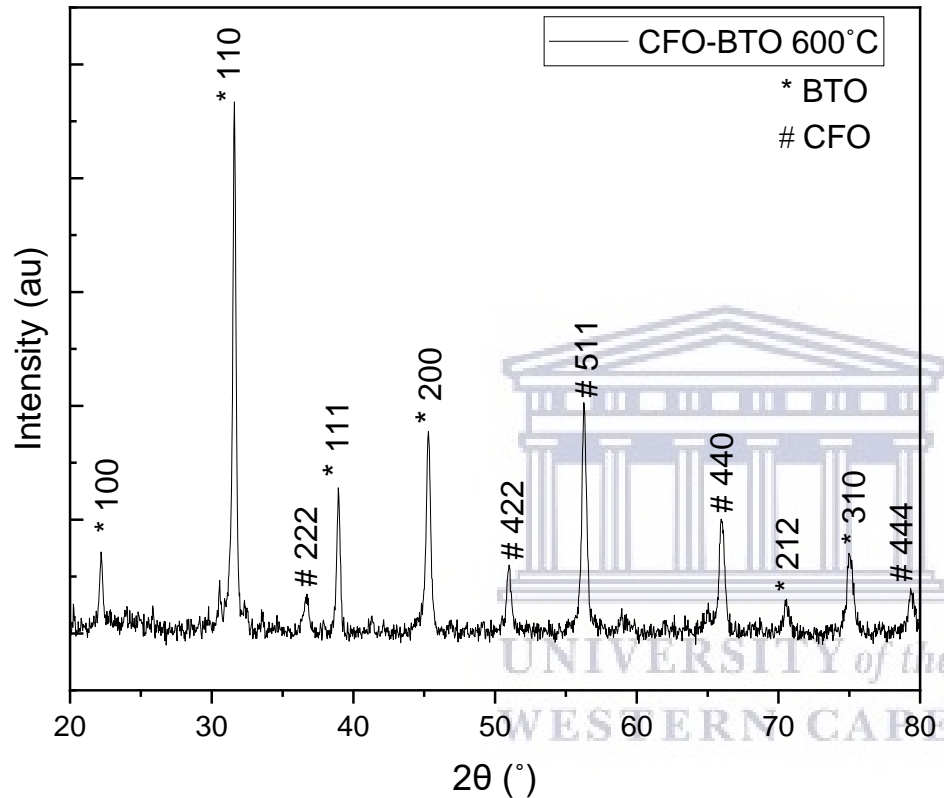
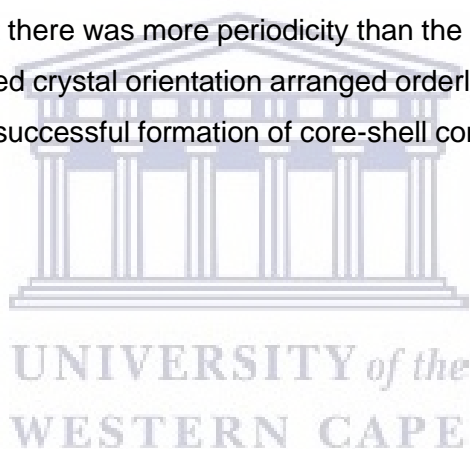


Figure 4.8. XRD pattern of tetragonal crystalline cobalt ferrite (CFO) – barium titanate (BTO) MENs calcined at 600°C. These MENs showed the presence of both CFO (#) and BTO (*). The diffraction peaks in the curve could be indexed to tetragonal MENs.

The XRD diffraction pattern (Figure 4.8) probed the crystallinity features of MENs calcined at 600°C without any trace of impurity phase. These results show that the synthesized MENs were crystalline. Successive diffraction peaks from low to high Bragg angle (Figure 4.8) corresponded to the (100), (110), (111), (200), (212) and (310) planes of (BTO) and (222), (422), (511), (440) and (444) planes of

(CFO). The diffraction peaks were found to be in agreement with the standard data of Joint Committee on Powder Diffraction Standards (JCPDS) (Analytical Chemistry, 1970) for BTO (JCPDS Card No. 05-0626) and CFO (JCPDS Card No. 22-1086).

The phase purity and crystallinity of MENs (600 °C) synthesized using the hydrothermal method were examined by XRD technique (Figure 4.8). The values met precisely with the standard data for BTO (JCPDS Card No. 05-0626) and CFO (JCPDS Card No. 22-1086). CFO (#) was present at 36.789 °, 51.571 °, 56.684°, 66.355° and 79.783°, and BTO (*) at 22.234°, 31.648°, 38.889°, 45.366°, 70.335° and 75.141°. The results further indicated that the MENs were tetragonal crystalline materials represented by the narrow peaks where some peaks were higher which means that there was more periodicity than the other directions (Figure 4.8). The height of most of the peaks appeared high indicative of a preferred crystal orientation arranged orderly. There were no traces of impurity phases. The absence of impurity phases was indicative of the successful formation of core-shell composite MENs and therefore the compatibility of magnetic CFO and ferroelectric BTO.



CHAPTER FIVE

CYTOTOXICITY, NANOPORATION AND DRUG TRANSPORTATION STUDIES OF MENs

5.1. Introduction

The aim of this part of the study was to establish a comparative analysis of *in vitro* cytotoxicity of the different concentrations of MENs (alone and in the presence of ethambutol) and free drug (ethambutol) on the BBB in the presence of AC and DC magnetic fields. Further, the aim was to determine the transportation of ethambutol across the BBB in the presence of the MENs. SEM was used to determine the occurrence of nanoporation. The *in vitro* cytotoxicity effects of the different concentrations of MENs and free drug were compared in the presence of a magnetic field by creating nanopores on the BBB cells (nanoporation) thereby increasing the penetration of the drug across the BBB monolayer.

5.2. Materials

Table 5.2. Materials used in this study.

Material	Manufacturer	Catalogue Number
Barium carbonate	Sigma-Aldrich® (Cape Town, South Africa)	513-77-9
Citric acid 99%	Sigma-Aldrich® (Cape Town, South Africa)	77-92-9
Cobalt (II) nitrate hexahydrate	Sigma-Aldrich® (Cape Town, South Africa)	10026-22-9
Ethanol (99%)	Kimix (Cape Town, South Africa)	
Iron (III) nitrate nonahydrate	Sigma-Aldrich® (Cape Town, South Africa)	7782-61-8
Polyvinylpyrrolidone K60, 45% in water	Sigma-Aldrich® (Cape Town, South Africa)	9003-39-8

Sodium borohydride	Sigma-Aldrich® (Cape Town, South Africa)	16940-66-2
Titanium (IV) isopropoxide 97% solution	Sigma-Aldrich® (Cape Town, South Africa)	546-68-9
immortalized mouse brain endothelioma (bEnd5) cells	Highveld Biological agents, American Type Culture Collection (ATCC)	96091930
Trypsin	WhiteSci (Whitehead Scientific (Pty) Ltd)	BE02-007E
Trypan blue stain (0.4%)	Lasec® (Cape Town, South Africa)	17-942E
Millicell™ inserts	Merck (Gauteng, South Africa)	R5CA86745
Countess™ Automated Cell Counter	Thermo Fisher Scientific (United States of America)	
12-well plates TC treated	Adcock Ingram (Midrand, South Africa)	13485
24-well plate TC treated	Adcock Ingram (Midrand, South Africa)	3524
Water bath	Lasec® (Cape Town, South Africa)	SKU ILAUL001101
Incubator	Memmert (Durban, South Africa)	
microscope (Type 120c NIKON Instruments Inc	NIKON (Missouri, United States of America)	MRD01994
DC- magnetic field power supply	Kikusui electronics corporation, Japan	
AC- magnetic field power supply	BMS Education, Cape Town	

5.3. bEnd5 cell culture and seeding

The immortalized mouse brain endothelioma (bEnd5) cells were obtained from Highveld Biological agents from American Type Culture Collection (ATCC). These endothelial cells are a subculture isolated from the cerebral cortex of mice. The bEnd5 cells were stored at a -80 °C freezer and thawed at 37 °C in a water bath (Mettler, Lasec®, South Africa) and then centrifuged for 5 min at 2500 rpm. The supernatant was then discarded, and the pellet was resuspended with 1 ml of DMEM: F-12 containing 10% FBS, 1% non-essential amino acids, 1% sodium pyruvate and 1% penicillin/streptomycin amphotericin B mixture. 1 ml of the cell suspension and 10 ml of the growth media were transferred into a 75 cm² TC flask and incubated at 37°C (95% humidity and 5% CO₂). After 24 h, cell attachment occurred (bEnd5 monolayer formation) and was confirmed with the use of a microscope (Type 120c NIKON Instruments Inc, USA).

When the cells became confluent, DMEM (containing 10% FBS) was discarded from the 75 cm² TC flask and the monolayer was washed with 3 ml of PBS. The monolayer was then exposed to 2 ml of 0.25X Trypsin and incubated at 37 °C, 5% CO₂ for 5 min to facilitate the detachment of the proteins that were adherent to the flask. 2 ml of DMEM was added to the flask to neutralize the trypsin and the flask was checked for cell movement under a microscope. The cells were centrifuged at 2500 rpm for 5 min after which the pellet was collected and resuspended with the same volume of fresh DMEM. The trypan blue cell counter was used to quantify the number of cells within the flask and amount of DMEM to be used for subsequent seeding. The cells were incubated for 3 days to enable the formation of a monolayer representing the tightness of the BBB.

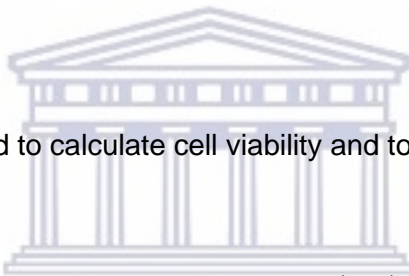
5.4. Evaluation of the cytotoxicity effects of MENs on bEnd5 cells

To determine the highest non-toxic dose of ethambutol, bEnd5 cells were seeded in 12-well plates (Adcock Ingram, Cat no. 30012) at a seeding density of 50 000 cm³. The treatment groups: primary control (C1): bEnd5 cells only (thawed bEnd5 cells without growth media, previously stored in a -80°C freezer), second control (C2): DMEM growth media only, 50 µg/ml, 100 µg/ml and 150 µg/ml concentrations of ethambutol were each exposed to the cells for 48 h into 3 wells

per column. After 48 h, the contents from each well plate were transferred into an Eppendorf tube. Thereafter, 500 µl of PBS was added into each well and transferred into the previous eppendorf tubes corresponding to each well. Then 0.25X trypsin was added into each well and the plates were incubated at 37 °C for 10 min to facilitate complete detachment of the cells. After 10 min the cells were checked under the microscope for movement. A volume of 500 µl of DMEM was added to each well to neutralize the trypsin. The cells were centrifuged at 2500 rpm for 5 min after which the pellet was collected and resuspended with 400 µl of fresh DMEM. Cells (20 µl) from the Eppendorf tubes and 20 µl of trypan blue stain were added in a new Eppendorf tube corresponding to the previous Eppendorf tubes. The contents (10 µl) from the Eppendorf tube with cells and trypan blue were placed on each side of the Countess™ glass slide upon which cell counts were performed on the cell counter (Countess™ Automated Cell Counter, Thermo Fisher Scientific, USA). Data was recorded and viability and toxicity values were calculated.

The following formulas were used to calculate cell viability and toxicity:

Equation 5.1:


$$\text{Viability (\%)} = \frac{\text{Number of unstained (live) cells}}{\text{total number of cells}} \times 100$$

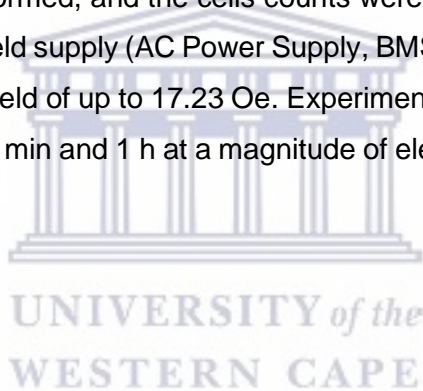
$$\text{Toxicity (\%)} = \frac{\text{Number of stained (dead) cells}}{\text{total number of cells}} \times 100$$

5.5. Determination of cytotoxicity in the presence of DC and AC-magnetic field stimulation

The cytotoxicity of the MENs in the presence of an applied DC and AC- magnetic field on the BBB cells was also determined. According to the results of the cytotoxicity studies (conducted in 5.4), the lowest non-toxic dose of MENs was selected, i.e. 0.1 mg/mL MENs. Cell culture studies were performed using the trypan blue method described in section 5.4. The cell plates (5 x 10⁴ cells per well) were arranged such that there were 3 controls and 3 samples of MENs (0.1 mg/mL) (one sample in each plate for the different magnetic field) in triplicate. The cells were seeded and the plates were stored in an incubator at 37 °C for 72 h instead of 24 h to form a BBB monolayer. After exposing the cells to MENs for 48 h, DC-magnetic field studies were performed on the cells

using a Helmholtz coil and cell counts were completed thereafter. The DC-magnetic field supply (Regulated DC power supply, Kikusui electronics corporation, Japan) could measure a maximum magnetic field magnitude of up to 22 Oe which supplied a maximum magnitude of the electric current of 3.71 A. Experiments were conducted for 0 Oe, 10 Oe, 20 Oe and 22 Oe magnetic field magnitudes for 30 minutes each at a magnitude of electric current of 0 A, 1.69 A, 3.37 A and 3.71 A, respectively.

Cell culture studies were performed using the trypan blue method described in section 5.4. The cell plates were arranged such that there were 5×10^4 cells per well, 3 controls, 3 samples of MENs (0.1 mg/mL) and another three samples of MENs 0.05 mg/ml (one sample in each plate for the different magnetic field) in triplicate. As with DC-magnetic field stimulation, cells were seeded and incubated at 37 °C for 72 h to form a BBB monolayer, thereby representing an *in vitro* BBB model. After the cells had been exposed to the different concentrations of MENs, AC-magnetic field studies were performed, and the cells counts were completed. The Helmholtz coil connected to the AC-magnetic field supply (AC Power Supply, BMS Education, Cape Town) could measure a maximum magnetic field of up to 17.23 Oe. Experiments were conducted for 0 Oe, 10 Oe and 17.23 Oe at 50 Hz for 30 min and 1 h at a magnitude of electric current of 0 A, 1.69 A and 2.91 A, respectively.



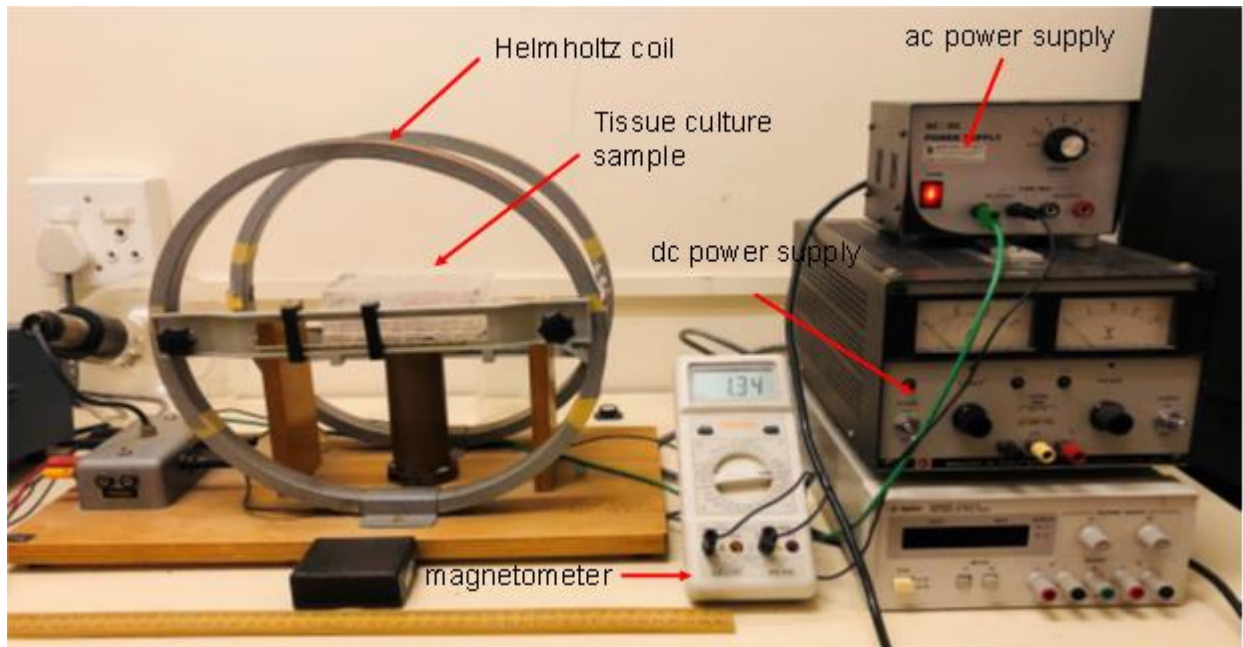


Figure 5.1. Helmholtz coil connected to an ac power supply where cell culture samples were exposed to a magnetic field. The current was measured and read on the magnetometer.

The formula for the magnitude of magnetic field (B) below, was used to determine the magnitude of the electric current (I) in amperes (A) that is displayed on the magnetometer which is adjusted on the AC and/or DC powers supply during magnetic field studies. This formula is particularly used when the magnitude of magnetic field is recorded in Tesla (Oe). μ_0 is the permeability of free space ($4\pi \times 10^{-7} \text{ T} \cdot \text{m} / \text{A}$) (Fishbane et al., 2005). R (0.15 m) is the distance recorded in meters and the number of coil turns is denoted with the symbol, N (130).

Equation 5.2:

Formula for the magnitude of the magnetic field (B) (Fishbane et al., 2005) (Ghosh et al., 2019):

$$1) B = \frac{8 \mu_0 N}{5\sqrt{5} R} \times [I]$$

$$2) I = \frac{5\sqrt{5} B R}{8 \mu_0 N}$$

Where,

B = magnetic field magnitude in Tesla (T)

μ_0 = permeability of free space ($4 \pi \times 10^{-7} \text{ T} \cdot \text{m} / \text{A}$)

I = magnitude of the electric current in amperes (A)

R = distance in meters (m)

N = number of coil turns

5.6. Ethambutol transportation across bEnd5 cells in the presence of MENs

The bEnd5 cells were seeded at a density of 50 000 cm^3 cells per insert/well in a 24-well microtiter plate on Millicell™ inserts with an area of 0.6 cm^2 and incubated at 37 °C and 5% CO_2 . Cells were left to grow to confluence in the incubator and allowed to attach to the bottom of the filter insert for 48 h to form a BBB monolayer. After 48 h cells were removed from the incubator and left at room temperature to acclimatize for 20 min in the laminar flow cabinet. 0.1 mg/ml MENs and the highest concentration of ethambutol (150 $\mu\text{g}/\text{ml}$) that did not show effect on cell growth during cytotoxicity studies were used. Cells were exposed for 48 h to a primary control (bEnd5 cells only), ethambutol free drug (150 $\mu\text{g}/\text{ml}$), MENs only (0.1 mg/ml), 150 $\mu\text{g}/\text{ml}$ ethambutol, and 150 $\mu\text{g}/\text{ml}$ ethambutol and 0.1 mg/ml MENs. The cells were later exposed to DC and AC- magnetic field stimulation. All experiments were performed in triplicate. Samples from the donor and receptor compartments were frozen at – 80 °C and analyzed later using liquid chromatography (LC) system coupled with mass spectrometer (MS) system. The following equation was used to calculate the % drug penetration:

Equation 5.3:

$$\begin{aligned} & \% \text{ drug penetration} \\ & = \frac{\text{conc. of drug in the receptor chamber}}{\text{sum of conc. of drug in the receptor chamber and conc. of drug in the donor chamber}} \times 100 \end{aligned}$$

5.7. LC-MS analysis of ethambutol

Ethambutol was analyzed on a Waters Xevo TQ-S (Milford, MA, USA) triple quadrupole mass spectrometer (MS), fitted with a Waters Accuity ultra-high pressure liquid chromatograph

(UHPLC). The precursor ion monitored for ethambutol was m/z 204.4 and the product ion m/z 116. A cone voltage of 15 V, a collision energy of 15 V and capillary voltage of 3.5 kV was used. Nitrogen was used as desolvation gas at 800 L/hr and the desolvation temperature was 500 C. The rest of the settings of the mass spectrometer was optimised for best sensitivity. A Waters BEH C18, 2.1x100mm, 1.7 μ m column was used to achieve separation at a column temperature of 50 C. The mobile phase was 0.1% ammonium hydroxide in MilliQ water (Solvent A) and 0.1% ammonium hydroxide in acetonitrile (Solvent B) and a flow rate of 0.3 mL/min was applied. A gradient was used starting at 95% solvent A for the first 0.5 min and changing to 100% solvent B over 6.5 min, washing the column for 1 min at 100% B, followed by a re-equilibration step of 2 min to make a total run time of 10 min. A calibration curve for ethambutol standard (Supplier XX) was constructed using the Targetlynx Application manager of Masslynx 4.1 (Waters, Milford, MA, USA) with a formula of $y=464338x$ and R^2 of 0.996. The retention time of the ethambutol peak was 1 min.



UNIVERSITY of the
WESTERN CAPE

5.8. Statistical analysis

GraphPad Prism (version 8.4.2) was used to capture and analyze the data. One-way ANOVA analysis was used to perform statistical comparison between set data groups. Two-way ANOVA analysis was used where necessary. The results of cell culture assays are aggregates of experiments performed in triplicate; the p-values were calculated from the averages of each independent experiment. A p-value less than 0.05 indicates a significant difference between two groups (Kimulwo et al., 2017). The Tukey test (or Tukey's Honest Significant Difference test) in conjunction with an ANOVA was used to determine significant levels of the data. The degree of significance is represented by an asterisk (*) next to the p-value; $p < 0.05$ (*), $p < 0.01$ (**), $p < 0.001$ (***) and $p < 0.0001$ (****).

5.9. Results and Discussion

5.9.1. Cytotoxicity of MENs in the absence of magnetic field stimulation

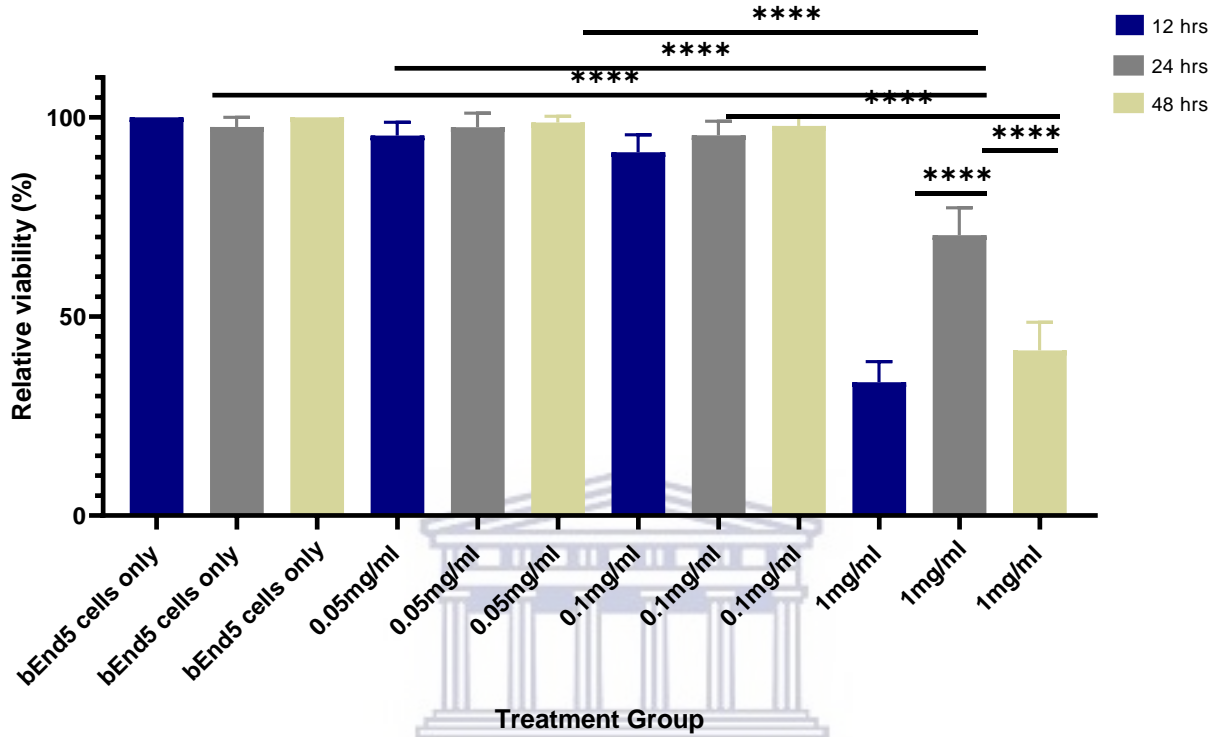


Figure 5.2. Viability of cells exposed to a control (bEnd5 cells only) and different concentrations of MENs for 12 h, 24 h and 48 h in the absence of DC and AC- magnetic field stimulation. The purpose of this study was to determine the cytotoxicity of the different concentrations of MENs in order to determine the least cytotoxic concentration for further studies.

The primary control showed 99.2 – 100 % cell viability (Figure 5.2). Cell viability (%) was observed to decrease with increasing concentrations of MENs (0.05 – 1 mg/ml). MENs at a concentration of 0.05 mg/ml had the highest percentage of cell viability ($97.21 \pm 1.67\%$) of samples exposed to MENs, followed by 0.1 mg/ml ($94.85 \pm 3.35\%$) while 1 mg/ml showed the lowest ($48.46 \pm 4.63\%$) cell viability and therefore the highest toxicity. There was a statistically significant difference in viability of cells treated with the 0.05 mg/ml MENs and 0.1 mg/ml MENs for 12, 24, and 48 h to the cells treated with 1 mg/ml of MENs for 12 h ($P < 0.0001$), 24 h ($P < 0.0001$) and 48 h ($P < 0.0001$). Cells treated with MENs 1 mg/ml for 24 h were significantly less viable than cells treated with the same concentration of MENs for 48 h ($P < 0.0001$).

5.9.2. Relative cell viability of MENs post-exposure to varying DC- magnetic fields

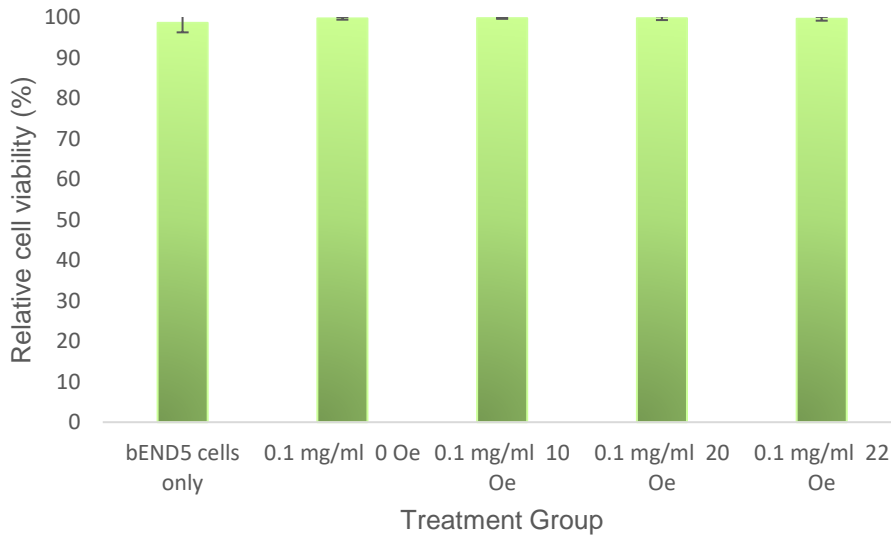


Figure 5.3. Relative cell viability (%) of cells exposed to 0.1 mg/mL MENs (the highest non-toxic dose observed) for 48 h after 30 min exposure to a DC-magnetic field stimulation (0 Oe – 22 Oe). All the treatment groups achieved relative cell viability of 99 %.

Cells were exposed to MENs (0.1 mg/ml) under varying DC-magnetic fields for 48 h. Post exposure to a DC-magnetic field, the primary control (bEnd5 cells only) showed an average of $98.61 \pm 2.35\%$ cell viability, which is the lowest cell viability of the treatment groups. The rest of the treatment groups i.e., 0.1 mg/ml at 0 Oe ($99.70 \pm 0.32\%$), 0.1 mg/ml at 10 Oe ($99.77 \pm 0.17\%$), 0.1 mg/ml at 20 Oe ($99.76 \pm 0.46\%$) and 0.1 mg/ml at 22 Oe ($99.62 \pm 0.47\%$) showed an average cell viability of over 99 %. Over the range of 10 – 22 Oe the MENs showed subminimum cytotoxicity.

5.9.3. Relative cell viability of MENs exposed to bEnd5 cells post-exposure to varying ac-magnetic fields

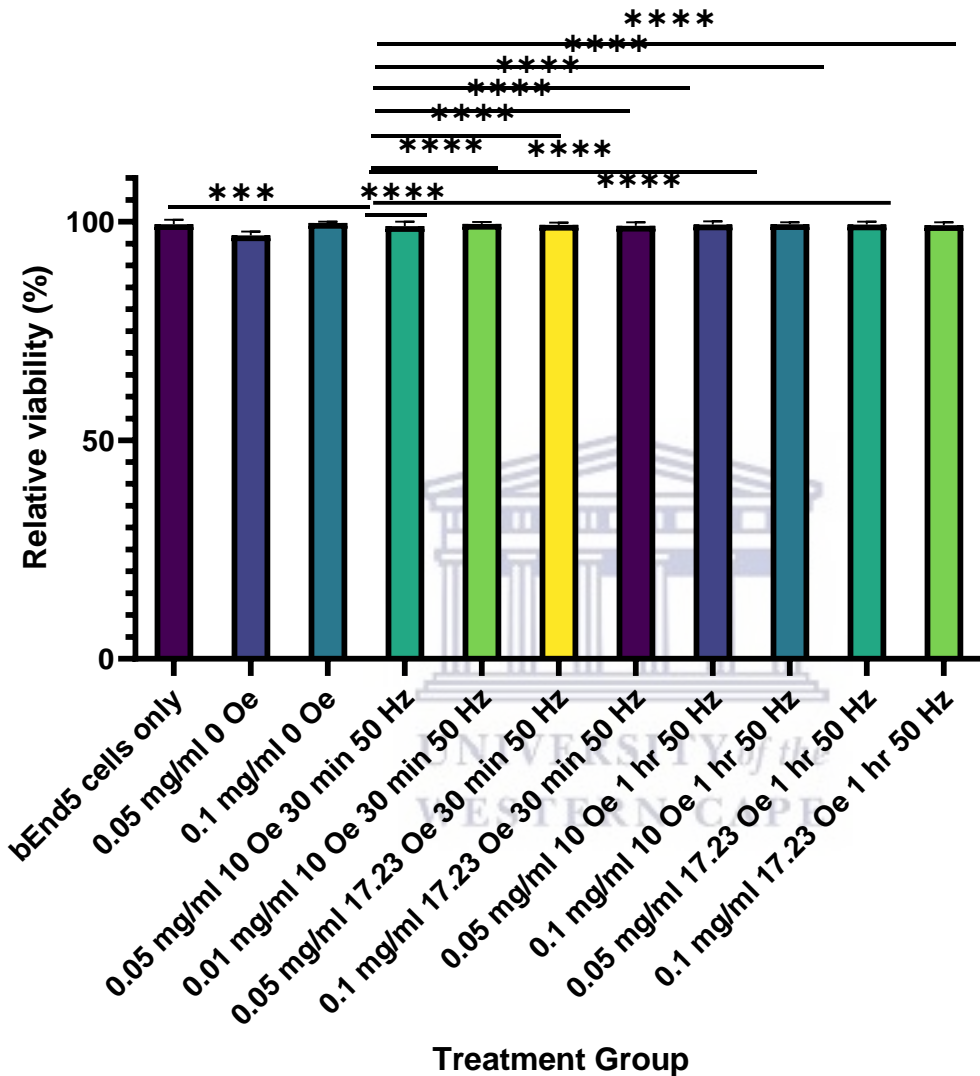


Figure 5.4. The effect of varying AC-magnetic fields on cell viability of MENs exposed to bEnd5 cells at set time points.

0.05 mg/ml MENs and 0.1 mg/ml MENs were exposed to bEnd5 cells to 0, 10 and 17.23 Oe ac-magnetic field for 0 min, 30 min and 1 h at 50 Hz. All the treatment groups showed more than 96.62 % cell viability in the presence of 0 (no magnetic field stimulation) - 17.23 Oe. All the treatment groups were nontoxic to cells. The lowest cell viability was observed at a concentration

of 0.05 mg/ml MENs at 0 Oe. Furthermore, no significant differences in cell death *were* observed between 0.05 -0.1 mg/ml MENs and between 0 – 17.23 Oe. bEnd5 cells only, cells exposed to growth media only, and cells exposed to deionized water and growth media without the presence of magnetic field stimulation were statistically significant to MENs 0.05 mg/ml not exposed to a magnetic field ($P < 0.0001$). From these results it was concluded that exposure to varying AC-magnetic field stimulation did not affect the cell viability of the cells. In addition, all the treatment groups displayed a high degree of statistical significance ($P < 0.0001$ and $p=0.0002$, ****) and therefore we can reject the null hypothesis.

In figure 5.4, 0.05 mg/ml MENs at 0 Oe and 0.1 mg/ml MENs at 0 Oe were statistically significant ($P < 0.0001$). 0.05 mg/ml MENs at 0 Oe and 0.05 mg/ml 10 Oe 30 min at a frequency of 50 Hz were statistically significant ($P = 0.0002$). 0.05 mg/ml MENs at 0 Oe was statistically significant to 0.01 mg/ml MENs at 10 Oe 30 min 50 Hz, 0.05 mg/ml MENs at 17.23 Oe 30 min 50 Hz, 0.1 mg/ml MENs at 17.23 Oe 30 min 50 Hz, 0.05 mg/ml MENs at 10 Oe 1 hr 50 Hz, 0.1 mg/ml MENs at 10 Oe 1 hr 50 Hz, 0.05 mg/ml MENs at 17.23 Oe 1 hr 50 Hz, and 0.1 mg/ml MENs at 17.23 Oe 1 hr 50 Hz ($P < 0.0001$).

Ideally, MENs are exposed to high DC- magnetic fields i.e., 80 Oe, 100 Oe and 450 Oe (Kaushik et al., 2017)(Pandey et al., 2020). However, due to the unavailability of a DC-power supply that can generate high currents, we used the only available DC-magnetic field power supply (Regulated DC power supply, Kikusui electronics corporation, Japan) which supplied a maximum magnitude of the electric current of 3.71 A. The results of this study showed that all the treatment groups had relatively 99% cell viability after exposure to the different DC-magnetic field currents for 30 min. It was concluded that these static and low-level magnetic fields are not cytotoxic to bEnd5 cells (Stewart et al., 2018).

5.9.4. Cytotoxicity of different concentrations of ethambutol

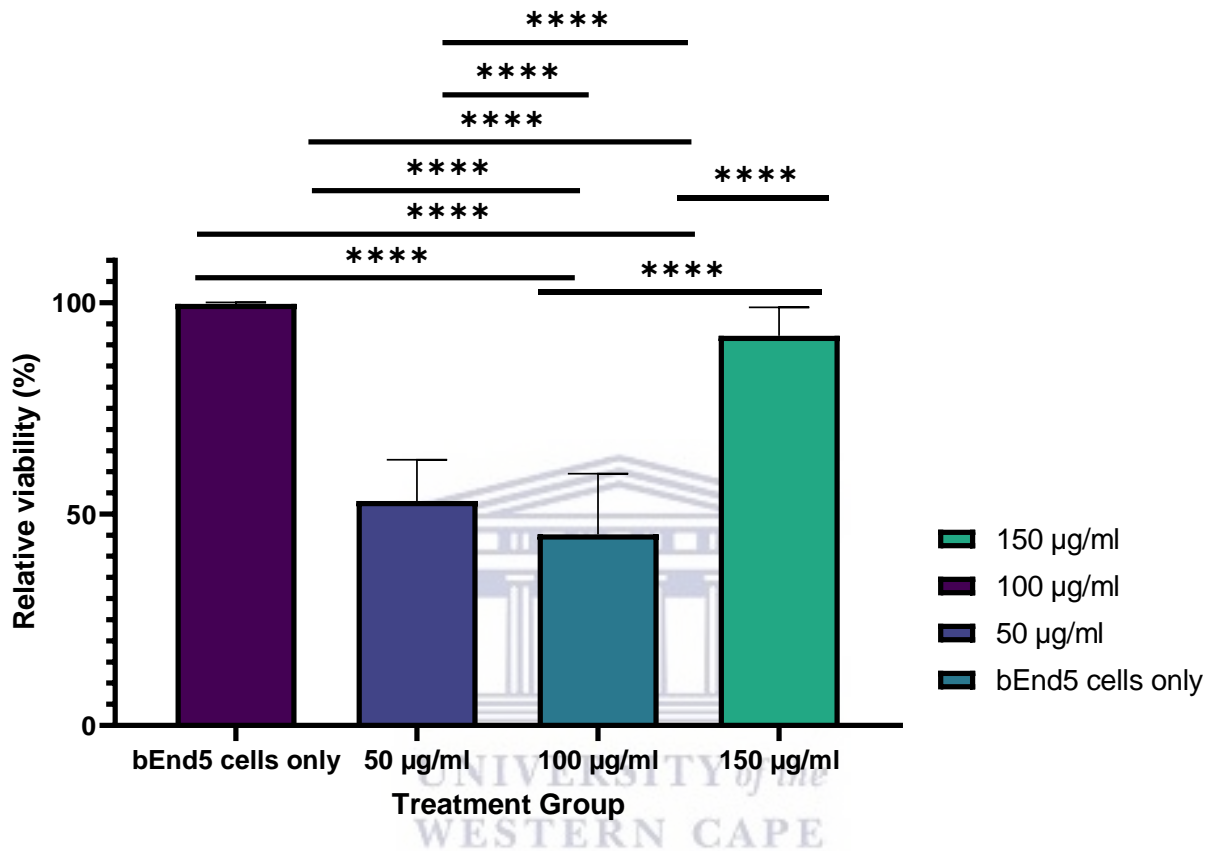


Figure 5.5. Relative cell viability (%) of ethambutol: 50 µg/ml, 100 µg/ml, and 150 µg/ml. These samples were not exposed to a magnetic field. The purpose of this study was to determine the least cytotoxic concentration of ethambutol to use in further studies. This test was performed in triplicate and the averages of the three tests are plotted in this figure.

bEnd5 cells were exposed to concentrations of 50, 100 and 150 µg/ml for 48 h to determine the highest non-toxic concentration of ethambutol to use in transportation studies (Figure 5.5). Interestingly, the highest concentration of ethambutol (150 µg/ml) showed the highest cell viability ($92.16 \pm 6.71\%$) and thus the least cytotoxic of the three concentrations. The 100 µg/ml concentration of ethambutol exhibited significant cytotoxicity ($45.19 \pm 14.36\%$) viability as did the 50 µg/ml where $53.11 \pm 9.77\%$ cell viability was observed. This suggests that ethambutol may have a protective effect on the cells. The neuroprotective potential of ethambutol may have

occurred as a result of the drug's ability to modulate the cytoprotective cell monolayer thus increasing the survival of the cells. This supports the findings on previous studies on the neuroprotective response of ethambutol to increase cell survival and balance homeostatic processes (Usman et al., 2022). However, in large concentrations, ethambutol can cause visual disturbance and toxic optic neuropathic and is therefore toxic to retinal ganglion cells (Irma et al., 2022).



5.9.5. Determination of nanoporation on bEnd5 cells

Control

MENs only

Drug only

Drug and MENs

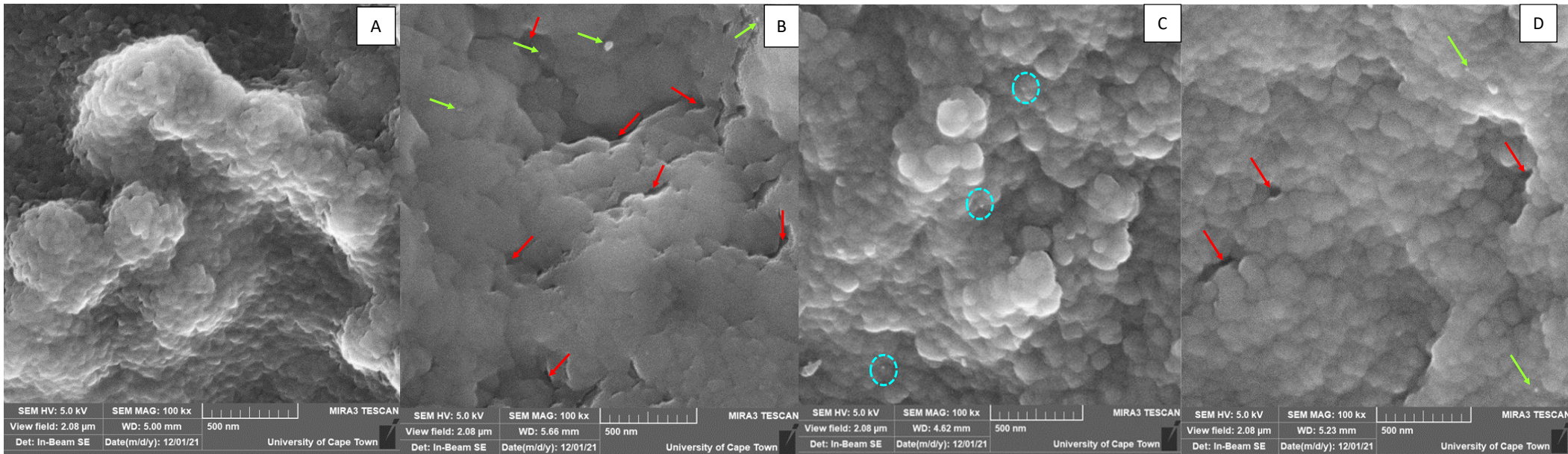


Figure 5.6.1. SEM images showing the interaction of MENs and drug (150 µg/ml ethambutol) with the bEnd5 monolayer seeded at 50 000 cm³ cells per well on a Transwell insert membrane (12 mm diameter with a 0.45 µm pore size) (Millicell™) for 48 h on a 500 nm scale. The contents of the cell wells were not exposed to a magnetic field. A is the control cell in DMEM only. B is cells exposed to MENs only. C is cells exposed to the drug only. D is cells exposed to both MENs and drug. Arrows GREEN; MENs only. RED; cell protrusions between adjacent endothelia. There are no clear cell protrusions in image A. The images with MENs only (B), and drug and MENs (D) show visible nanopores which are more prominent in image D while the cells exposed to drug only do not show visible cell protrusions.

Control

MENs only

Drug only

Drug and MENs

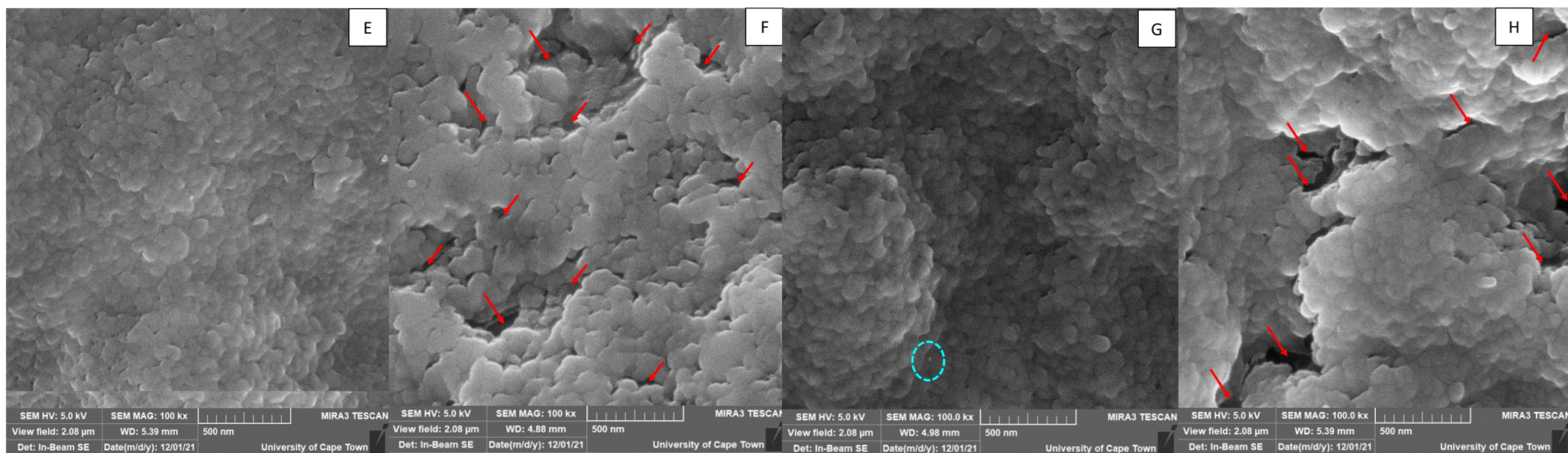
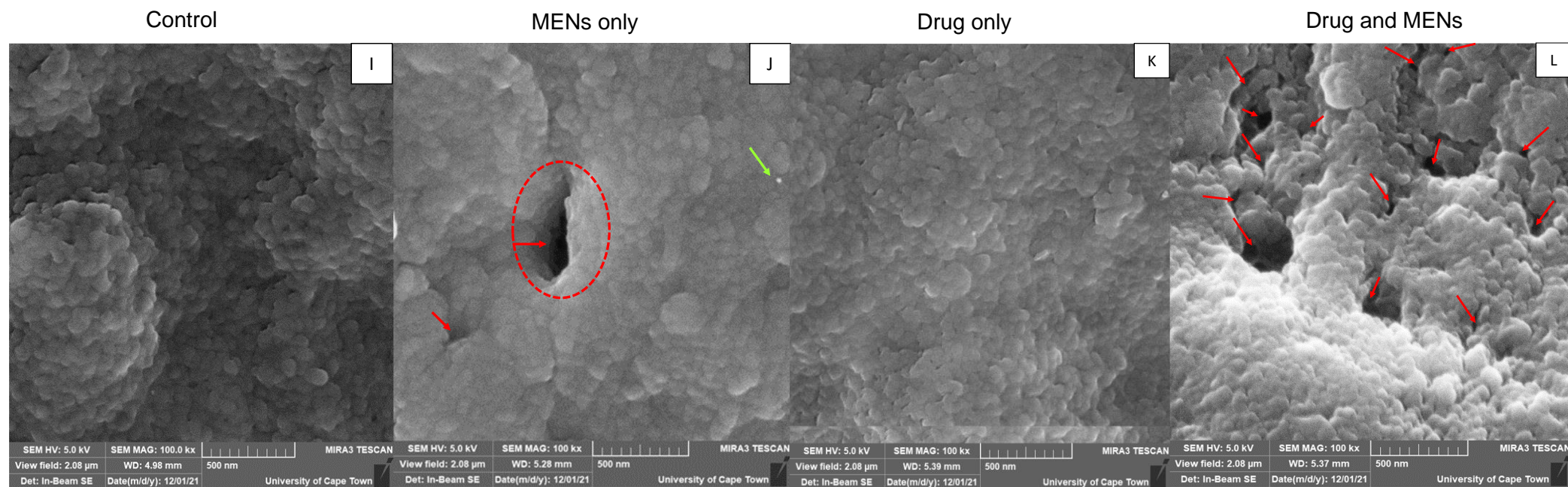


Figure 5.6.2. SEM images showing the interaction of MENs and drug (150 μ g/ml ethambutol) with the bEnd5 monolayer seeded at 50 000 cm³ cells per well on a Transwell insert membrane (12 mm diameter with a 0.45 μ m pore size) (Millicell™) for 48 h on a 500 nm scale. The contents of the cell wells were exposed first to 4.13 A DC-magnetic field for 30 min and then to AC-magnetic field (1.33 A, at 50 Hz frequency) for another 30 min. E is the control cell in DMEM only. F is cells exposed to MENs only. G is cells exposed to the drug only. H is cells exposed to both MENs and drug. Arrows RED; cell protrusions between adjacent endothelia. Image E shows cell protrusions of less than 50 nm. The images with MENs only (F), and drug and MENs (H) show the formation of nanoporation. Image H shows the largest sizes of nanopores. No noticeable cell protrusions are shown in the cells exposed to drug only (G). The effect of nanoporation in the image with drugs only is very similar to that with the control only.



WESTERN CAPE

Figure 5.6.3. SEM images showing the interaction of MENs and drug (150 μ g/ml ethambutol) with the bEnd5 monolayer seeded at 50 000 cm³ cells per well on a Transwell insert membrane (12 mm diameter with a 0.45 μ m pore size) (Millicell™) for 48 h on a 500 nm scale. The contents of the cell wells were exposed first to 4.13 A DC-electric current magnetic field for 1 h and then to AC-magnetic field (1.33 A, at 50 Hz frequency) for another 1 h. I is the control cell in DMEM only. J is cells exposed to MENs only. K is cells exposed to the drug only. L is cells exposed to both MENs and drug. Arrows GREEN; MENs only. RED; cell protrusions between adjacent endothelia. Image I shows cell protrusions of approximately 35 nm. The image with MENs only (J) shows cell protrusions one of which is 500 nm in size and thus the formation of nanoporation. Image L shows the largest sizes of nanopores. The largest pore size in image L is 300 nm. The cells exposed to drug only (K) do not show clearly visible cell protrusions.

Treatment groups (control, drug only, MENs only, drug and MENs) (Figure 5.6.1) were seeded in a bEnd5 monolayer at 50 000 cm³ cells per well on a Transwell insert membrane (12 mm diameter with a 0.45 µm pore size) (Millicell™) for 48 h and were exposed to room temperature without AC and DC- magnetic field stimulation. Nanopores between adjacent endothelial cells were observed in monolayers exposed to MENs only (image B) and in monolayers exposed to drug and MENs (image D) (Figure 5.6.1B&D RED arrows). Nanoporation formation was much more prominent in the cells exposed to drugs and MENs and showed the largest sizes of nanopores compared to the other cells in this treatment group. As per the results, it was not expected to see the presence of nanoelectroporation (the use of a focused electric pulse to generate pores in the cell membrane forming a nanopore) in Figure 5.6.1A&C because these cells were not exposed to MENs nor to a magnetic field but were rather exposed to a control and ethambutol and instead were subjected to room temperature. From this, it was concluded that nanoporation occurs in cells in the presence of MENs even without AC and DC-magnetic field stimulation.

The aim was to determine the formation of nanoporation *in vitro* from the effects of exposing a known concentration of MENs (empty and MENs loaded) and free drug (ethambutol) to a DC and AC-magnetic field. The purpose of DC-magnetic field stimulation is to trigger penetration of the drug-loaded MENs into the cells. AC-magnetic field stimulation triggers the release of the drug off the MEN carriers into the cells (Rodzinski et al., 2016)(Yang et al., 2021). In clinical practice, MENs are delivered into the bloodstream and guided to penetrate the CNS through the induction of a DC-magnetic field (Yang et al., 2021). The formation of nanopores in the cell membrane is facilitated by CoFe₂O₄ @ BaTiO₃ core shell MENs that induce transient nanoporation on bEnd5 cells leading to enhanced uptake of ethambutol across the cells. Wireless stimulation of an external alternating magnetic field enables the delivery of MENs into the brain without inducing a neuroinflammatory response (Yang et al., 2021).

It was decided to work with the maximum magnitude of electric current in order to see the largest nanopore formation and induce nanoelectroporation from generating the maximum electric current and thereby support the hypothesis. There is evidence that nanoelectroporation occurred after the treatment groups had been exposed to DC (4.13 A) and AC-magnetic field (1.33 A at 50 Hz frequency) for 30 mins (Figure 5.6.2). In figure 5.6.2H, an absence of drugs and MEN particulates at the surface of the BBB was observed and there was a greater number of nanopores present at the surface of the BBB. The formation of nanopores had caused most of the drug and MENs to slip into the BBB thereby penetrating the BBB monolayer. This explanation is in agreement with the work demonstrated by Hossain, Guo and Bhalla et al., 2021. This was

evidence that nanoelectroporation had occurred and that the drugs and MENs had successfully penetrated the BBB monolayer.

5.9.6. Transportation of ethambutol across the BBB

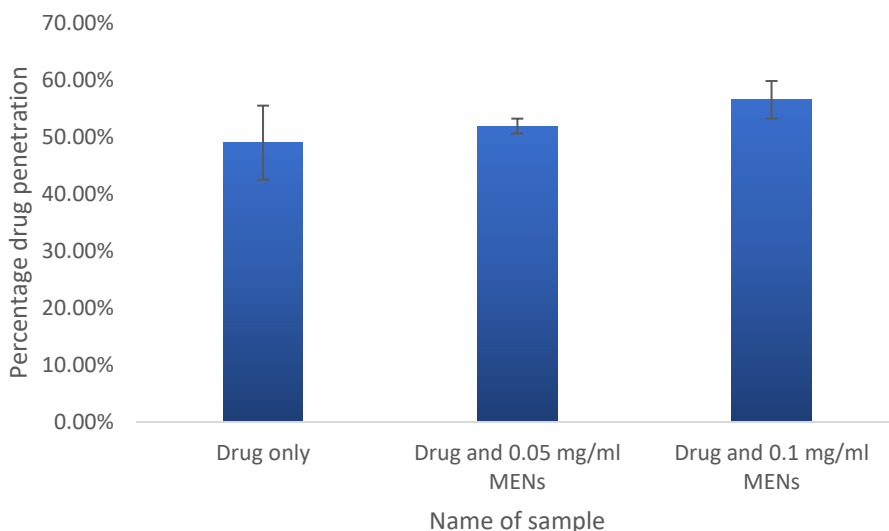


Figure 5.7. The effect of exposure of 150 µg/ml ethambutol only, ethambutol (150 µg/ml) and 0.05 mg/ml, and ethambutol (150 µg/ml) and 0.1 mg/ml MENs to an hour of DC and AC-magnetic field stimulation. This data shows the average % of the drug and MENs collected from the receptor compartment.

The samples shown in Figure 5.7 contain either ethambutol alone or ethambutol with two different concentrations of MENs (0.05 mg/ml MENs and 0.1 mg/ml MENs) exposed to a DC and AC magnetic field stimulation (Figure 5.7). The samples exposed to drug only show a percentage of ethambutol collected from the receptor compartment (49.01 ± 0.07%). It was expected that the BBB cells exposed to the drug only to have a significantly lower % concentration of drug in the receptor compartment compared to the drug samples in the presence of 0.05 mg/ml or 0.1 mg/ml MENs (Figure 5.7). There is no statistical significant difference between the control (drug only) and those with MENs 0.05 mg/ml and 0.1 mg/ml ($p > 0.05$). It could be that the transport of ethambutol is not dependent on the nanopores formed. It is also possible that greater

transportation of the drug could have been observed if larger magnetic fields were available for use in this study. However, there were limitations based on instrumentation on magnetic fields that could be investigate.



CHAPTER SIX

CONCLUSION

This study reports the synthesis and characterization of $\text{CoFe}_2\text{O}_4 @ \text{BaTiO}_3$ core shell MENs, the formation of nanopores and their efficacy in the *in vitro* transportation of ethambutol across the BBB. The physicochemical properties of hydrodynamic diameter, polydispersity index and ζ -potential, atomic forces, magnetic forces, structure and composition of MENs were determined. The cytotoxicity of the MENs against bEnd5 cells, induction of nanoporation and transportation of ethambutol in the presence of DC and AC-magnetic field stimulation was measured. It was hypothesized that $\text{CoFe}_2\text{O}_4 @ \text{BaTiO}_3$ core shell MENs will induce poration on bEND5 cells leading to enhanced uptake of ethambutol across the cells.

$\text{CoFe}_2\text{O}_4 @ \text{BaTiO}_3$ core shell MENs were synthesized. Through the use of TEM and AFM analyses, it was established that these MENs were almost spherical core shell NPs with an average size of ~ 30 nm and according to XRD analysis these were crystalline nanomaterials. In this study, an *in vitro* BBB model was used to evaluate the penetration of ethambutol across a BBB monolayer in the presence of MENs. *In vitro* BBB studies showed that the presence of MENs alone was enough to induce nanoelectroporation and facilitate the transportation of ethambutol across the BBB monolayer. Although not statistically significant to transportation of drug in the absence of MENs. It was observed that $\text{CoFe}_2\text{O}_4 @ \text{BaTiO}_3$ core shell MENs induce nanoporation on bEnd5 cells and lead to enhanced uptake of ethambutol across the cells. The results from this study have demonstrated that $\text{CoFe}_2\text{O}_4 @ \text{BaTiO}_3$ core shell MENs could be used for externally controlled targeted drug delivery and release.

In summary, the data shows that MENs are biologically compatible with bEnd5 cells. The data also shows that low-level magnetic fields do not have an effect on the cytotoxicity of bEnd5 cells *in vitro*. Though the $\text{CoFe}_2\text{O}_4 @ \text{BaTiO}_3$ core shell MENs were able to effectively induce transient electroporation on bEND5 cells leading to enhanced uptake of ethambutol across the cells, it is recommended that future studies could investigate larger electric currents as large as 100 Oe (12.832A), 200 Oe (25.664A), 500 Oe (64.16A) and 1000 Oe (128.32A) and also other anti-TB drugs.

Future studies could access transient pore formation and test whether the nanopores close after exposure to both AC and DC- power supply. *In-vivo* studies in relevant animal studies could be performed as well.

CHAPTER SEVEN

REFERENCES

- Abdulkhaleq, L. A., Assi, M.A., Abdullah, R., Zamri-Saad, M., Taufiq-Yap, Y.H., & Hezmee, M.N.M. (2018) 'The crucial roles of inflammatory mediators in inflammation: A review', *Veterinary World*, 11(5), pp. 627–635.
- Adams, R. A., Bauer, J., Flick, M.J., Sikorski, S.L., Nuriel T., Lassmann, H., Degen, J.L., & Akassoglou, K. (2007) 'The fibrin-derived γ 377-395 peptide inhibits microglia activation and suppresses relapsing paralysis in central nervous system autoimmune disease', *Journal of Experimental Medicine*, 204(3), pp. 571–582.
- Ahsan, R., Mitra, A., Omar, S., Khan, M.Z.R., & Basith, M.A. (2018) 'Sol-gel synthesis of DyCrO₃ and 10% Fe-doped DyCrO₃ nanoparticles with enhanced photocatalytic hydrogen production abilities', *RSC Advances*, 8(26), pp. 14258–14267.
- Akiyama, Y., & Okano, T. (2015) 'Temperature-responsive polymers for cell culture and tissue engineering applications', *Switchable and responsive Surfaces and Materials for Biomedical Applications*, pp. 203-233.
- Alexander, A., Agrawal, M., Uddin, A., Siddique, S., Shehata, A.M., Shaker, M.A., Rahman, A.U. Mim, A., & Shaker, M.A. (2019) 'Recent expansions of novel strategies towards the drug targeting into the brain', *International Journal of Nanomedicine* 14, pg. 5895-5909.
- Allen, L.V. (2017) 'Ethambutol Hydrochloride Compounded Oral Suspension USP (100mg/mL)', *US Pharm* 42 (8), pg.48-49.
- Alvarez-Uria, G., Midde, M., Pakam, R., & Naik, P.K. (2013) 'Initial Antituberculous Regimen with Better Drug Penetration into Cerebrospinal Fluid Reduces Mortality in HIV Infected Patients with Tuberculous Meningitis: Data from an HIV Observational Cohort Study', *Tuberculosis Research and Treatment*, 2013, pp. 1–7.
- Ameh, E. S. (2019) 'A review of basic crystallography and x-ray diffraction applications', *International Journal of Advanced Manufacturing Technology*, 105(7–8), pp. 3289–3302.

Amiz, H.A.E. (2017) 'Magneto-electric nanocarriers for drug delivery: An overview', *Journal of Drug Delivery Science and Technology* 37, pg.46-50.

Asim, N., Ahmadi, S., Alghoul, M.A., Hammadi, F.Y., Saeedfar, K., & Sopian, K. (2014) 'Research and Development Aspects on Chemical Preparation Techniques of Photoanodes for Dye Sensitized Solar Cells', *International Journal of Photoenergy*.

Asmari, A.K., Ullah, Z., Tariq, M., & Fatani, A. (2016) 'Preparation, characterization, and in vivo evaluation of intranasally administered liposomal formulation of dopenezil', *Drug design, development and therapy* 10, pg. 205-215.

Azarmi, M., Maleki, H., Nikkam, N., & Malekinejad, H. (2020) 'Transcellular brain drug delivery: A review on recent advancements', *International Journal of Pharmaceutics*, 586(March), p. 119582.

Balla, A., & Goli, D. (2020) 'Formulation & evaluation of PLGA nanoparticles of ropinirole HCl for targeting brain', *Indian Journal of Pharmaceutical Sciences*, 82(4), pp. 622–631.

Batrakova, E.V., & Kim, M.S. (2015) 'Using exosomes, naturally-equipped nanocarriers, for drug delivery', *Journal of Controlled Release* 219, pg. 396-405.

Bellavia, D., Raimondo, S., Calabrese, G., Forte, S., Cristaldi, M., Patinella, A., Memeo, L., Manno, M., Raccosta, S., Diana, P., Cirrincione, G., Giavaresi, G., Monteleone, F., Fontana, S., De Leo, G., & Alessandro, R. (2017) 'Interleukin 3- receptor targeted exosomes inhibit in vitro and in vivo Chronic Myelogenous Leukemia cell growth', *Theranostics* 7 (5), pg. 1333-1345.

Bellettato, C. M. & Scarpa, M. (2018) 'Possible strategies to cross the blood–brain barrier', *Italian Journal of Pediatrics*, 44(S2).

Belur, L.R., Temme, A., Podetz-Pedersen, K. M, Riedl, M., Vulchanova, L., Robinson, N., Hanson, L.R., Kozarsky, K.F., Orchard, P.J., Freyll, W.H., Low, W.C., & McIvor, R.S. (2017) 'Intranasal adeno-associated virus mediated gene delivery and expression of human iduronidase in the central nervous system: a noninvasive and effective approach for prevention of neurologic disease in mucopolysaccharidosis type I', *Hum Gene Ther*, 28(7):576–87.

Betal, S., Shrestha, B., Dutta, M., Cotica, L., Khachatryan, E., Nash, K., Tang, L., Bhalla, A.S., & Guo, R. (2016) 'Magneto-elasto-electroporation (MEEP): In-vitro visualization and numerical characteristics', *Scientific Reports* 6, 32019.

Betzer, O., Shilo, M., Opoichinsky, R., Barnoy, E., Motiei, M., Okun, E., Yadid, G., & Popovtzer, R. (2017) 'The effect of nanoparticle size on the ability to cross the blood-brain barrier: An in vivo study', *Nanomedicine*, 12, pp. 1533–1546.

Canta, M., & Cauda, V. (2020) 'The investigation of the parameters affecting the ZnO nanoparticle cytotoxicity behaviour: a tutorial review', *Biomater Sci*, 8(22), pg. 6157-6174.

Chakaya, J., Khan, M., Ntoumi, F., Aklillu, E., Fatima, F., Mwaba, P., Kapata, N., Mfinanga, S., Hasnain, S.E., Katoto, P.D.M.C., Bulabula, A.N.H., Sam-Agudu, N.A., Nachega, J.B., Tiberi, S., McHugh, T.D., Abubakar., I & Zumla, A. (2021) 'Global Tuberculosis Report 2020 – Reflections on the Global TB burden, treatment and prevention efforts', *International Journal of Infectious Diseases*, (xxxx), pp. 4–9.

Chen, W., Zou, Y., Zhong, Z., & Haag R. (2017) 'Cyclo(RGD)-decorated reduction-responsive nanogels mediate targeted chemotherapy of integrin overexpressing human glioblastoma in vivo', *Small* 13 (6), pg. 1-9.

Chen, W., Huang, L., Tang, Q., Wang., S., Hu, C., & Zhang, X. (2020) 'Progress on diagnosis and treatment of central nervous system tuberculosis', *Radiology of Infectious Diseases*, 7(4), pp. 160–169.

Cherian, A., Ajitha, K.C., Iype, T., & Divya, K.P. (2021) 'Neurotuberculosis: an update', *Acta Neurologica Belgica*, 121(1), pp. 11–21.

Cherian A., & Thomas, S.V. 2011. 'Central nervous system tuberculosis', *African Health Sciences* 11 (1), 116-127.

Chiang, S. S., & Starke, J. R. (2018) 'Mycobacterium tuberculosis', *Principles and Practice of Pediatric Infectious Diseases*. Fifth Edit. Elsevier Inc.

Corral-Flores, V., Bueno-Baqués, D., & Ziolo, R. F. (2010) 'Synthesis and characterization of novel CoFe₂O₄-BaTiO₃ multiferroic core-shell-type nanostructures', *Acta Materialia*, 58(3), pp. 764–769.

Cucullo, L., Couraud, P.O., Weksler, B.B., Romero, I.A., Hossain, M., Rapp, E., & Janigro, D. (2008) 'Immortalized human brain endothelial cells and flow-based vascular modeling: a marriage of convenience for rational neurovascular studies', *Journal of Cerebral Blood Flow & Metabolism* 28 (2), pg. 312-328.

Curley, S.M., & Cady, N.C. (2018) 'Biologically- derived nanomaterials for targeted therapeutic delivery to the brain', *Science Progress* 101 (3), pg. 276 and 278.

Danaei, M., Deghankhold, M., Ataei, S., Davarani, F.H., Javanmard, R., Dokhani, A., Khorasani, S., & Mozafari, M.R. (2018) 'Impact of particle size and polydispersity index on the clinical applications of lipidic nanocarrier systems', *Pharmaceutics*, 10(2), pp. 1–17.

Daneman, R., & Prat A. 2015. 'The Blood –Brain Barrier', *Cold Spring Harb Perspect Biol* 2015; 7:a020412 pp. 1–23.

Das, M. K., & Chakraborty, T. (2015) 'Progress in brain delivery of Anti-HIV drugs', *Journal of Applied Pharmaceutical Science*, 5(7), pp. 154–164.

Davis, A., Meintjes, G., & Wilkinson, R. J. (2018) 'Treatment of Tuberculous Meningitis and Its Complications in Adults', *Current Treatment Options in Neurology*, 20(3).

Deb, P.K., Al-Attraqchi, O., Chandrasekaran, B., Paradkar, A., & Tekade, R.K. (2019) 'Protein/Peptide Drug Delivery Systems: Practical Considerations in Pharmaceutical product Development', *Basic Fundamentals of Drug Delivery*, pg. 651-684.

Dikpati, A., Madgulkar, A.R., Kshirasagar, S.J., Bhalekar, M.R., & Chahal, A.S. (2012) 'Targeted Drug Delivery to CNS using Nanoparticles', *Journal of Advanced Pharmaceutical Sciences* 2 (1), pg.180.

Djukic, M., Munz, M., Sorgel, F., Holzgrabe, U., Eiffert, H., & Nau, R. (2012) 'Overton's rule helps to estimate the penetration of anti-infectives into patients' cerebrospinal fluid', *Antimicrobial Agents and Chemotherapy*, 56(2), pp. 979–988.

Donald, P. R. (2010) 'Cerebrospinal fluid concentrations of antituberculosis agents in adults and children', *Tuberculosis*, 90(5), pp. 279–292.

Dong, X. (2018) 'Current strategies for brain drug delivery', *Theranostics*, 8(6), pp. 1481–1493.

Dube, A. (2019) 'Nanomedicines for infectious diseases', *Pharmaceutical Research*, 36(11), pp. 1-2.

Elbrecht, D.H., Long, C.J., & Hickman, J.J. (2016) 'Transepithelial/endothelial Electrical Resistance (TEER) theory and applications for microfluidic body-on-a-chip devices', *Journal of Rare Diseases Research & Treatment* 1 (3), pg.46-52.

Emerich, D.F., Dean, R.L., Osborn, C., & Bartus, R.T. (2001) 'The Development of the Bradykinin Agonist Labradimil as a Means to Increase the Permeability of the Blood-Brain Barrier: From Concept to Clinical Evaluation', *Clinical Pharmacokinetics* 40 (2), pg. 105-123.

Erickson, M. A., Wilson, M. L. & Banks, W. A. (2020) 'In vitro modeling of blood-brain barrier and interface functions in neuroimmune communication', *Fluids and Barriers of the CNS*, 17(1), pp. 1–16.

Fernandes, J., Ghate, M.V., Mallik, S.B., & Lewis, S.A. (2018) 'Amino acid conjugated chitosan nanoparticles for the brain targeting of a model dipeptidyl peptidase-4 inhibitor', *International Journal of Pharmaceutics* 547(1-2), pg. 563-571.

Fisher, D., & Mentor, S. (2020) 'Are claudin-5 tight-junction proteins in the blood-brain barrier porous?', *Neural Regeneration Research*, 15(10), pp. 1838–1839.

Fujioka, Y. (2011) 'Infrared emission spectroscopy and its application to analyze non-smooth metallic materials surface', *Nippon Steel Technical Report*, (100), pp. 78–84.

Gan, Y.X., Jayatissa, A.H., Yu, Z., Chen, X., & Li, M. (2020) 'Hydrothermal Synthesis of Nanomaterials', *Journal of Nanomaterials*, Article ID 8917013, 3 pages.

Ganapathe, L. S., Mohamed, M.A., Yunus, R.M., & Berhanuddin, D.D. (2020) 'Magnetite (Fe₃O₄) nanoparticles in biomedical application: From synthesis to surface functionalisation', *Magnetochemistry*, 6(4), pp. 1–35.

Ghaderi, S., Ramesh, B., & Seifalian, A.M. (2011) 'Fluorescence nanoparticles "quantum dots" as drug delivery system and their toxicity: a review', *Journal of drug targeting* 19 (7), pg. 475-486.

Ghosh, S., Sonker, P.K., & Chowdhury, S.R. (2019) 'Sensors & Transducers Modeling and Simulation of Low-Cost and Low-Magnetic Field Magnetic Resonance Imaging', 231(3), pp. 25–

30.

Giugliani, R., Giugliani, L., Poswar, F.O., Donis, K.C., Corte, A.D., Schmidt, M., Boado, R.J., Nestrasil, I., Nguyen, C., Chen, S., & Pardridge, W.M. (2018) 'Neurocognitive and somatic stabilization in pediatric patients with severe Mucopolysaccharidosis Type i after 52 weeks of intravenous brain-penetrating insulin receptor antibody-iduronidase fusion protein (valanafusp alpha): An open label phase 1-2 trial', *Orphanet Journal of Rare Diseases*, 13(1), pp. 1–11.

Guccione, P., Lopresti, M., Milanesio, M., & Caliandro, R. (2021) 'Multivariate analysis applications in x-ray diffraction', *Crystals*, 11(1), pp. 1–21.

Guduru, R., Liang, P., Runowicz, C., Nair, M., Atluri, V., & Khizroev, S. (2013) 'Magneto-electric Nanoparticles to Enable Field-controlled High-Specificity Drug Delivery to Eradicate Ovarian Cancer Cells', *Scientific Reports* 3 (2953).

Guduru, R., Liang, P., Hong, J., Rodzinski, A., Hadjikhani, A., Horstmyer, J., Levister, E., & Khizroev, S. (2015) 'Magnetolectric "spin" on stimulating the brain', *Nanomedicine*, 10(13), pp. 2051–2061.

Hadjikhani, A., Rodzinski, A., Wang, P., Nagesetti, A., Guduru, R., Liang, P., Runowicz, C., Shahbazmohamadi, S., & Khizroev, S. (2017) 'Biodistribution and clearance of magnetolectric nanoparticles for nanomedical applications using energy dispersive spectroscopy', *Nanomedicine*, 12(15), pp. 1801–1822.

Hamilton, G.S. (1998) 'Immunophilin ligands for the treatment of neurological disorders', *Expert Opin Ther Pat* 8:1109–24.

Harikishore, A., & Yoon, H.S. (2015) 'Immunophilins: Structures, Mechanisms and Ligands', *Curr Mol Pharmacology* 9 (1), pg. 37-47.

Helms, H.C., Abbott, N.J., Burek, M., Cecchelli, R., Couraud, P.O., Deli, M.A., Forster, C., Galla, H.J., Romero, I.A., Shusta, E.V., Stebbins, M.J., Vandenhoute, E., Weksler, B., & Brodin, B. (2016) 'In vitro models of the blood-brain barrier: An overview of commonly used brain endothelial cell culture models and guidelines for their use', *Journal of Cerebral Blood Flow & Metabolism* 36 (5), pg. 862-890.

Hersh, D., Wadajkar, A.S., Roberts, N., Perez, J.G., Connolly, N.P., Frenkel, V., Winkles, J.A.,

Woodworth, G.F., & Kim, A.J. (2016) 'Evolving drug delivery strategies to overcome the blood brain barrier', *22*(9), pp. 1177–1193.

Hossain, S., Guo, R. & Bhalla, A. (2021) 'Analysis using physics model to understand magnetoelectric nanorobotic structures for targeted cell manipulation', *Ferroelectrics*, *585*(1), pp. 70–87.

Hosseini, M., Arif, M., Keshavarz, A., & Iglauer, S. (2021) 'Neutron scattering: A subsurface application review', *Earth-Science Reviews*, *221*(August), p. 103755.

Hu, F., Liu, J., Xu, C., Wang, Z., Liu, G., Li, H., & Zhao, S. (2018) 'Soil internal forces initiate aggregate breakdown and splash erosion', *Geoderma*, *320*(26), pp. 43–51.

Irma, J., Kartika, A., Rini, M., Setiohadji, B., & Salim, J. (2022) 'A Protective Role of Coenzyme Q10 in Ethambutol-Induced Retinal Ganglion Cell Toxicity: A Randomised Controlled Trial in Mice', *Neuro-Ophthalmology*.

Islam, Y., Leach, A.G., Smith, J., Pluchino, S., Coxon, C.R., Sivakumaran, M., Downing, J., Fatokun, A.A., Teixido, M., & Ehtezazi, T. (2020) 'Peptide based drug delivery systems to the brain', *Nano Express*, *1*(1), p. 012002.

Jain, K.K. (2007) 'Nanobiotechnology-based drug delivery to the central nervous system', *Neurodegenerative Diseases* *4* (4), pg. 287-291.

Jamieson, J.J., Searson, P.C., & Gerecht, S. (2017) 'Engineering the human blood-brain barrier in vitro', *Journal of Biological Engineering* *11*(37).

Jenkin, G. (2017) 'Pyrazinamide', *Kucers the Use of Antibiotics: A Clinical Review of Antibacterial, Antifungal, Antiparasitic, and Antiviral Drugs, Seventh Edition*, *88*, pp. 2361–2368.

Jia, G., Han, Y., An, Y., Ding, Y., He, C., Wang, X., & Tang, Q. (2018) 'NRP-1 targeted and cargo-loaded exosomes facilitate simultaneous imaging and therapy of glioma in vitro and in vivo', *Biomaterials*, *178*, pp. 302–316.

Joint Committee on Powder Diffraction Standards. (1970) *Analytical Chemistry* *42* (11), 81A.

Joshy, K.S., & Sharma, C.P. (2012) 'Blood compatible nanostructured lipid carriers for the enhanced delivery of azidothymidine to brain', *Adv. Sci. Lett.* *6*, 47–55.

Kamran, M., Ullah, A., Mehmood, Y., Nadeem, K., & Krenn, H. (2017) 'Role of SiO₂ coating in multiferroic CoCr₂O₄ nanoparticles', *AIP Advances* 7(2), 025011.

Kasinathan, N., Jagani, H.V., Alex, A.T., Volety, S.M., & Rao, J.V. (2015) 'Strategies for drug delivery to the central nervous system by systemic route', *Drug Delivery*, 22(3), pp. 243–257.

Kaushik, A., Jayant, R., Sagar, V., & Nair, M. (2014) 'The potential of magnetoelectric nanocarriers for drug delivery.' *Expert Opin. Drug Deliv.* 11(10), 1635-1646.

Kaushik, A., Nikkah-Moshaie, R., Sinha, R., Bhardwaj, V., Atluri, V., Jayant, R.D., Yndart, A., Kateb, B., Pala, N., & Nair, M. (2017) 'Investigation of ac-magnetic field stimulated nanoelectroporation of magneto-electric nano-drug-carrier inside CNS cells', *Scientific Reports*, 7(April), pp. 1–12.

Kaushik, A., Yndart, A., Atluri, V., Tiwari, S., Tomitaka, A., Jayant, R.D., Gupta, P., Alvarez-Carbonell, D., Khalili, K., & Nair, M. (2019) 'Magnetically guided non-invasive CRISPR-Cas9/gRNA delivery across blood-brain barrier to eradicate latent HIV-1 infection', *Scientific Reports* 9 (3928).

Khizroev, S., Nair, M., Liang, P., Runowicz, C., & Guduru, R. (2018) 'On-demand release using magneto-electric nanoparticles', *The Florida International University Board of Trustees*, United States, 9895549.

Kilic, G., Fernandez-Bertolez, N., Costa, C., Brandao, F., Teixeira, J.P., Pasaro, E., Laffon, B., & Valdiglesias, V. (2017) 'The Application, Neurotoxicity, and Related Mechanism of Iron Oxide nanoparticles', *Neurotoxicity of Nanomaterials and Nanomedicine*, pg. 127-150.

Kimulwo, M.J., Okendo, J., Aman, R.A., Ogutu, B.R., Kokwaro, G.O., Ochieng, D.J., Muigai, A.W.T., Oloo, F.A., & Ochieng, W. (2017) 'Plasma nevirapine concentrations predict virological and adherence failure in Kenyan HIV-1 infected patients with extensive antiretroviral treatment exposure', *PLoS ONE*, 12(2), pp. 1–14.

Kong, S.D., Lee, J., Ramachandran, S., Eliceiri, B.P., Shubayev, V.I., Lal, R., & Jin, S. (2012) 'Magnetic targeting of nanoparticles across the intact blood-brain barrier', *J. Control. Release* (164), pg.49–57.

Lakshminarayana, S. B., Haut, T.B., Ho, P.C., Manjunatha, U.H., Dartois, V., Dick, T., & Rao,

S.P.S. (2015) 'Comprehensive physicochemical, pharmacokinetic and activity profiling of anti-TB agents', *Journal of Antimicrobial Chemotherapy*, 70(3), pp. 857–867.

Le, T.N., & Blakley, B.W. (2017) 'Mannitol and the blood-labyrinth barrier', *Journal of Otolaryngology-Head & Neck Surgery* 46 (66).

Leonard, J.M. (2017) 'Central Nervous System Tuberculosis', *Tuberculosis and Nontuberculous Mycobacterial Infections, Seventh Edition*, pg. 331-341.

Global tuberculosis report 2020. Geneva: World Health Organization; 2020. Licence: CC BY-NC-SA 3.0 IGO.

Li, H., Tong, Y., Bai, L., Ye, L., Zhong, L., Duan, X., & Zhu, Y. (2018) 'Lactoferrin functionalized PEG-PLGA nanoparticles of shikonin for brain targeting therapy of glioma', *International Journal of Biological Macromolecules* 107 (Pt A), pg. 204-211.

Li, X., Tsibouklis, J., Weng, T., Zhang, B., Yin, G., Feng, G., Cui, Y., Savina, I.N., Mikhalovska, L.I., Sandeman, S.R., Howel, C.A., & Mikhalovsky, S.V. (2017) 'Nanocarriers for drug transport across the blood-brain barrier', *Journal of drug targeting* 25 (1), pg.17-28.

Li, Y., He, H. Jia, X., Lu, W.L., Lou, J., & Wei, Y. (2012) 'A dual-targeting nanocarrier based on poly(amidoamine) dendrimers conjugated with transferrin and tamoxifen for treating brain gliomas', *Biomaterials* 33 (15), pg. 3899-3908.

Liu, L., Guo, K., Lu, J., Venkatraman, S.S., Luo, D., Ng, K.C., Ling, E., Moochhala, S., & Yang, Y. (2008) 'Biologically active core/shell nanoparticles self-assembled from cholesterol-terminated PEG-TAT for drug delivery across the blood-brain barrier', *Biomaterials* 29 (10), pg.1509-1517.

Liu, S., Ma, C., Ma, G., & Xu, F. (2019) 'Magnetic Nanocomposite Adsorbents. Composite Nanoadsorbents', *Micro and Nano Technologies*, pg. 295-316.

Lu, Y., Han, S., Zheng, H., Ma, R., Ping, Y., Zou, J., Tang, H., Zhang, Y., Xu, X., & Li, F. (2018) 'A novel RGDyC/PEG co-modified PAMAM dendrimer-loaded arsenic trioxide of glioma targeting delivery system', *International Journal of Nanomedicine* 13, pg. 5937-5952.

Lungu, M., Neculae, A., Bunoiu, M., & Biris, C. (2015) 'Nanoparticles' promises and risks: Characterization, manipulation, and potential hazards to humanity and the environment', *Nanoparticles' Promises and Risks: Characterization, Manipulation, and Potential Hazards to Humanity and the Environment*, pp. 1–355.

Luo, S., Ma, C., Z, M., Ju, W., Yang, Y., & Wang, X. (2020) 'Application of Iron Oxide Nanoparticles in the Diagnosis and Treatment of Neurodegenerative Diseases With Emphasis on Alzheimer's Disease', *Frontiers in Cellular Neuroscience*, 14(February), pp. 1–11.

Maguire, C. M., Rosslein, M., Wick, P., & Prina-Mello, A. (2018) 'Characterisation of particles in solution—a perspective on light scattering and comparative technologies', *Science and Technology of Advanced Materials*, 19(1), pp. 732–745.

Małkiewicz, M. A., Szarmach, A., Sabisz, A., Cubula, W.J., Szurowska, E., & Winkelwski, P.J. (2019) 'Blood-brain barrier permeability and physical exercise', *Journal of Neuroinflammation*, 16(1), pp. 1–16.

Malwela, T. & Sinha, Ray, S. (2014) 'Investigating the crystal growth behavior of biodegradable polymer blend thin films using in situ atomic force microscopy', *Macromolecular Materials and Engineering*, 299(6), pp. 689–697.

McMahon, D. & Hynynen, K. (2017) 'Acute inflammatory response following increased blood-brain barrier permeability induced by focused ultrasound is dependent on microbubble dose', *Theranostics*, 7(16), pp. 3989–4000.

Me, M. (2008) 'Rifampin', *Tuberculosis*, 88(2), pp. 151–154.

Mishra, V., Kesharwani, P., Amin, M. C. I. M., & Iyer, A. (2017). 'Nanotechnology-based approaches for targeting and delivery of drugs and genes' *Academic Press*, pp. 506.

Mitchison, D.A. (2000) 'Role of individual drugs in chemotherapy of tuberculosis', *The international journal of tuberculosis and lung disease* 4 (9), pg. 796-806.

Sousa, M., Pozniak, A., & Boffito, M. (2008) 'Pharmacokinetics and pharmacodynamics of drug interactions involving rifampicin, rifabutin and antimalarial drugs', *Journal of Antimicrobial Chemotherapy* 62 (5), pg.872-878.

Moen, E. K., Ibey, B.L., Beier, H.T., & Armani, A.M. (2016) 'Quantifying pulsed electric field-induced membrane nanoporation in single cells', *Biochimica et Biophysica Acta - Biomembranes*,

1858(11), pp. 2795–2803.

Mossu, A., Rosito, M., Khire, T., Chung, H.L., Nishihara, H., Gruber, I., Luke, E., Dehouck, L., Sallusto, F., Gosselet, F., McGrath, J.L., & Engelhardt, B. (2019) 'A silicon nanomembrane platform for the visualization of immune cell trafficking across the human blood–brain barrier under flow', *Journal of Cerebral Blood Flow and Metabolism*, 39(3), pp. 395–410.

Muthu, M. S., & Wilson, B. (2012) 'Challenges posed by the scale-up of nanomedicines', *Nanomedicine*, 7(3), pp. 307–309.

Nagesetti, A., Rodzinski, A., Stimphil, E., Stewart, T., Khanal, C., Wang, P., Guduru, R., Liang, P., Agoulnik, I., Horstmyer, J., & Khizroev, S. (2017) 'Multiferroic coreshell magnetoelectric nanoparticles as NMR sensitive nanoprobe for cancer cell detection', *Scientific Reports*, 7(1), pp. 1–9.

Nair, M., Guduru, R., Liang, P., Hong, J., Sagar, V., & Khizroev, S. (2013) 'Externally on-demand release of anti-HIV drug using magnetoelectric nanoparticles as carriers', *Nat. Commun.*, 4, 1707.

Napotnik, T.B., & Miklavčič, D. (2018) 'In vitro electroporation detection methods- An overview', *Bioelectrochemistry* 120, pp. 166-182.

Nau, R., Sörgel, F., & Eiffert, H. (2010) 'Penetration of drugs through the blood-cerebrospinal fluid/blood-brain barrier for treatment of central nervous system infections', *Clinical Microbiology Reviews*, 23(4), pp. 858–883.

Vinciguerra, A., & Tagliatela, M. (2018) 'PhD PROGRAM IN NEUROSCIENCE PhD Thesis : ' Role of Autophagy in the regulation of Angiogenesis in Stroke '.

Otani, T. & Furuse, M. (2020) 'Tight Junction Structure and Function Revisited', *Trends in Cell Biology*, 30(10), pp. 805–817.

Pajouhesh, H., & Lenz, R.G. (2005) 'Medicinal Chemical Properties of Successful Central Nervous System Drugs', *NeuroRx* 2 (4), pp. 541-553.

Pakhomov, A.G., Bowman, A.M., Ibey, B.L., Andre, F.M., Pakhomova, O.N., & Schoenbach, K.H. (2009) 'Analysis of conductance of forward-rectifying membrane pores induced by nanosecond electric pulses in GH3 (murine pituitary) and CHO-K1 cells', *Biochem. Biophys. Res. Commun.* 385, pp. 181–186.

Pandey, P., Ghimire, G., Garcia, J., Rubfiaro, A., Wang, X., Tomitaka, A., Nair, M., Kaushik, A., & He, J. (2020) 'Single-Entity Approach to Investigate Surface Charge Enhancement in Magnetoelectric Nanoparticles Induced by AC Magnetic Field Stimulation', *ACS sensors*. ISSN: 2379-3694.

Pardridge, W.M. (2012) 'Drug transport across the blood-brain barrier', *Journal of Cerebral Blood Flow & Metabolism* 32 (11), pg. 1959-1972.

Pardridge, W. M. (2020) 'Treatment of alzheimer's disease and blood-brain barrier drug delivery', *Pharmaceuticals*, 13(11), pp. 1–25.

Patra, J. K., Das, G., Fraceto, L.F., Campos, E.V.R., Rodriguez-Torres, M.P., Acosta-Torres, L.S., Diaz-Torres, L.A., Grillo, R., Swamy, M.K., Sharma, S., Habtemariam, S., & Shin, H. (2018) 'Nano based drug delivery systems: Recent developments and future prospects 10 Technology 1007 Nanotechnology 03 Chemical Sciences 0306 Physical Chemistry (incl. Structural) 03 Chemical Sciences 0303 Macromolecular and Materials Chemistry 11 Medical and He', *Journal of Nanobiotechnology*, 16(1), pp. 1–33.

Paul, A., Zhang, B., Mohapatra, S., Li, G., Li, Y., Gazit, E., & Segel, D. (2019) 'Novel mannitol-based small molecules for inhibiting aggregation of α -synuclein amyloids in Parkinson's disease', *Frontiers in Molecular Biosciences*, 6(MAR), pp. 1–10.

Persidsky, Y., Stins, M., Way, D., Witte, M.H., Weinand, M., Kim, K.S., Bock, P., Gendelman, H.E., & Fiala, M. (1997) 'A model for monocyte migration through the blood-brain barrier during HIV-1 encephalitis', *J. Immunol* (158), pg.3499–3510.

Pervaiz, E., Gul, I.H., & Anwar, H. (2013) 'Hydrothermal Synthesis and Characterization of CoFe_2O_4 Nanoparticles and Nanorods', *J Supercond Nov Magn* 26, pg. 415-424.

Picchio, V., Cammisotto, V., Pagano, F., Carnevale, R., & Chimenti, I. (2020) 'We are IntechOpen, the world's leading publisher of Open Access books Built by scientists, for scientists TOP 1%', *Intechopen*, (Cell Interaction-Regulation of Immune Responses, Disease Development and Management Strategies), pp. 1–15.

Ramli, S. F., Aziz, H.A., Omar, F.M., Yusoff, M.S., Kamaruddin, H.H.M.A., & Ariffin, K.S. (2021) 'Removal of colour and suspended solids from landfill leachate using Tin tetrachloride (SnCl_4):

The effects of pH, zeta potential, and particle sizes ', *International Journal of Environmental Analytical Chemistry*, 00(00), pp. 1–16.

Rane, A.V., Kanny, K., Abitha, V.K., & Thomas, S. (2018) 'Methods for Synthesis of Nanoparticles and Fabrication of Nanocomposites', *Synthesis of Inorganic Nanomaterials*, pg. 121-139.

Redzic, Z. (2011) 'Molecular biology of the blood-brain and the blood-cerebrospinal fluid barriers: Similarities and differences', *Fluids and Barriers of the CNS*, 8(1), pp. 1–25.

Reichel, A. (2010) 'The Blood-Brain Barrier and CNS Penetration: a Drug Discovery Point of View', *Front. Pharmacol. Conference Abstract: Pharmacology and Toxicology of the Blood-Brain Barrier. State of the Art, Needs for Future Research and Expected Benefits for the EU*.

Reigoto, A. M., Andrade, S.A., Seixas, M., Costa, M.L., & Mermelstein, C. (2021) 'A comparative study on the use of microscopy in pharmacology and cell biology research', *PLoS ONE*, 16(1 January), pp. 1–13.

Ren, J., Shen, S., Wang, D., Xi, Z., Guo, L., Pang, Z., Qian, Y., Sun, X., & Jiang, X. (2012) 'The targeted delivery of anticancer drugs to brain glioma by PEGylated oxidized multi-walled carbon nanotubes modified with angiopep-2', *Biomaterials* 33 (11), pg. 3324-3333.

Ribovski, L., Hamelmann, N. M., & Paulusse, J. M. J. (2021) 'Polymeric Nanoparticles Properties and Brain Delivery', *Pharmaceutics*, 13(12), p. 2045.

Rodriguez-Takeuchi, S. Y., Renjifo, M. E. & Medina, F. J. (2019) 'Extrapulmonary tuberculosis: Pathophysiology and imaging findings', *Radiographics*, 39(7), pp. 2023–2037.

Rodzinski, A., Guduru, R., Liang, P., Hadjikhani, A., Stewart, T., Stimphil, E., Runowicz, C., Cote, R., Altman, N., Datar, R., & Khizroev, S. (2016) 'Targeted and controlled anticancer drug delivery and release with magnetoelectric nanoparticles', *Scientific Reports*, 6(January), pp. 1–14.

Rosenblatt, R. B., Frank, J. A. & Burks, S. R. (2020) 'Cytosolic Ca²⁺ transients during pulsed focused ultrasound generate reactive oxygen species and cause DNA damage in tumor cells', *Theranostics*, 11(2), pp. 602–613.

Ross, C., Taylor, M., Fullwood, N., & Allsop, D. (2018) 'Liposome delivery systems for the treatment of Alzheimer's disease', *International Journal of Nanomedicine* 13, pg. 8507-8522.

Roth, C. C., Barnes, R.A., Ibey, B.L., Beier, H.T., Mimun, L.C., Maswadi, S.M., Shadaram, M., Glickman, R.D. (2015) 'Characterization of pressure transients generated by nanosecond electrical pulse (nsEP) exposure', *Scientific Reports*, 5(September), pp. 1–15.

Sagar, V., Pilakka-Kanthikeel, S., Pottathil, R., Saxena, S.K., & Nair, M. (2014) 'Towards nanomedicine for neuroAIDS', *Reviews in medical virology* 24 (2), pg.109-124.

Seo, S. E., & Hawker, C. J. (2020) 'The Beauty of Branching in Polymer Science', *Macromolecules*, 53(9), pp. 3257–3261.

Shi, D., Mi, G., Bhattacharya, S., Nayar, S., & Webster, T.J. (2016) 'Optimizing superparamagnetic iron oxide nanoparticles as drug carriers using an in vitro blood-brain barrier model', *International Journal of Nanomedicine* 11, 5371-5379.

Song, J., Lu, C., Leszek, J., & Zhang, J. (2021) 'Design and development of nanomaterial-based drug carriers to overcome the blood–brain barrier by using different transport mechanisms', *International Journal of Molecular Sciences*, 22(18).

Squibb, B., & Index, M. (2008) 'Isoniazid', *Tuberculosis*, 88(2), pp. 112–116.

Sridhara, V., & Joshi, R. P. (2014) 'Numerical study of lipid translocation driven by nanoporation due to multiple high-intensity, ultrashort electrical pulses', *Biochimica et Biophysica Acta - Biomembranes*, 1838(3), pp. 902–909.

Steiner, O., Coisne, C., Engelhardt, B., & Lyck R. (2010) 'Comparison of immortalized bEnd5 and primary mouse brain microvascular endothelial cells as in vitro blood-brain barrier models for the study of T cell extravasation', *Journal of Cerebral Blood Flow & Metabolism* 31 (1), pg. 315-327.

Stewart, T. S., Nagesetti, A., Guduru, R., Liang, P., Stimphil, E., Hadjikhani, A., Salgueiro, L., Horstmyer, J., Cai, R., Schally, A., & Khizroev, S. (2018) 'Magnetolectric nanoparticles for delivery of antitumor peptides into glioblastoma cells by magnetic fields', *Nanomedicine*, 13(4), pp. 423–438.

Stimphil, E., Nagesetti, A., Guduru, R., Stewart, T., Rodzinski, A., Liang, P., & Khizroev, S. (2017) 'Physics considerations in targeted anticancer drug delivery by magnetolectric nanoparticles', *Applied Physics Reviews* 4(2), 021101.

Sousa, M., Pozniak, A., & Boffito, M. (2008) 'Pharmacokinetics and pharmacodynamics of drug interactions involving rifampicin, rifabutin and antimalarial drugs', *Journal of Antimicrobial Chemotherapy* 62 (5), pg.872-878.

Su, S. & Kang, P. M. (2020) 'Systemic review of biodegradable nanomaterials in nanomedicine', *Nanomaterials*, 10(4).

Su, X., Kells, A.P., Salegio, E.A., Richardson, R.M., Hadaczek, P., Beyer, J., Bringas, J., Pivrotto, P., Forsayeth, J., & Bankiewicz, K.S. (2010) 'Real-time MR imaging With Gadoteridol Predicts Distribution of Transgenes After Convection-enhanced Delivery of AAV2 Vectors', *Molecular Therapy* 18(8), pg.1490-1495.

Subramanian, K. S., Raja, K., & Kannan, M. (2019) 'A Textbook on Fundamentals and Applications of Nanotechnology', *Kemampuan Koneksi Matematis (Tinjauan Terhadap Pendekatan Pembelajaran Savi)*, 53(9), pp. 1689–1699.

Sun, Z., Worden, M., Wroczynskyj, Y., Yathindranath, V., van Lierop, J., Hegmann, T., & Miller, D.W. (2014) 'Magnetic field enhanced connective diffusion of iron oxide nanoparticles in an osmotically disrupted cell culture model of the blood-brain barrier', *International journal of medicine* 9, pg. 3013-3026.

Tang, J., Huang, N., Zhang, X., Zhou, T., Tan, Y., Pi, J., Pi, L., Cheng, S., Zheng, H., Cheng, Y. (2017) 'Aptamer-conjugated PEGylated quantum dots targeting epidermal growth factor receptor variant III for fluorescence imaging of glioma', *International journal of nanomedicine* 12, pg. 3899-3911.

Teleanu, D. M., Chircov, C., Grumezescu, A.M., Volceanov, A., & Teleanu, R.I. (2018) 'Blood-brain delivery methods using nanotechnology', *Pharmaceutics*, 10(4), pp. 1–16.

Tetu, J.F (2016) 'Why is the hCMEC/D3 cell line a robust in vitro model?', In *tebu-bio blog*. Available at: <https://www.tebu-bio.com/blog/2016/01/14/why-the-hcmecd3-cell-line-is-a-robust-in-vitro-bbb-model/>.

Toth, A.E., Nielsen, S.S.E., Tomaka, W., Abbott, N.J., & Nielsen, M.S. (2019) 'The endo-lysosomal system of bEnd.3 and hCMEC/D3 brain endothelial cells', *Fluids and Barriers of the CNS* 16(14).

Ulett, G. C. & Beacham, R. (2014) 'Pathogens Penetrating the Central Nervous System : Infection', 27(4), pp. 691–726.

Upadhyay, R. K. (2014) 'Drug delivery systems, CNS protection, and the blood brain barrier', *BioMed Research International*, 2014.

Usman, H., Tan, Z., Gul, M., Rashid, S., Ali, T., Shah, F.A., Li, S., & Li, J.B. (2022) 'Identification of novel and potential PPAR γ stimulators as repurposed drugs for MCAO associated brain degeneration', *Toxicology and Applied Pharmacology*, 446(May), p. 116055.

Vallabani, N.V.S., & Singh, S. (2018) 'Recent advances and future prospects of iron oxide nanoparticles in biomedicine and diagnostics', 3 *Biotech* 8 (6), 279.

Varanda, L.C., de Souza, C.G., Perecin, C.J., de Moraes, D.A., de Queiroz, F., Neves, H.R., Junior, J.B.S., da Silva, M.F., Albers, R.F., & da Silva, T.L. (2019) 'Inorganic and organic-inorganic composite nanoparticles with potential biomedical applications: synthesis challenges for enhanced performance', *Materials for Biomedical Engineering. Bioactive Materials, Properties, and Applications*. Chapter 3. pg. 47-99.

Viscusi, E. R. & Viscusi, A. R. (2020) 'Blood-brain barrier: Mechanisms governing permeability and interaction with peripherally acting μ -opioid receptor antagonists', *Regional Anesthesia and Pain Medicine*, 45(9), pp. 688–695.

Warren, G., Makarov, E., Lu, Y. Senanayake, T., Rivera, K., Gorantla, S., Poluektova, L.Y., & Vinogradov, S.V. (2015) 'Amphiphilic cationic nanogels as brain-targeted carriers for activated nucleoside reverse transcriptase inhibitors', *Journal of neuroimmune pharmacology* 10 (1), pg. 88-101.

Watanabe, T., Dohgu, S., Takata, F., Nishioku, T., Nakashima, A., Futagami, K., Yamauchi, A., & Kataoka, Y. (2013) 'Paracellular barrier and tight junction protein expression in the immortalized brain endothelial cell lines bEND.3, bEND.5 and mouse brain endothelial cell 4', *Biol Pharm Bull* 36 (3), pg. 492-495.

Weksler, B., Romero, I. A. & Couraud, P. O. (2013) 'The hCMEC/D3 cell line as a model of the human blood brain barrier', *Fluids and Barriers of the CNS*, 10(1), p. 1.

Weksler, B.B., Subileau, E.A., Perriere, N., Charneau, P., Holloway, K., Leveque, M., Tricoire-Leignel, H., Nicotra, A., Bourdoulous, S., Turowski, P., Male, D.K., Roux, F., Greenwood, J., Romero, I.A., & Couraud, P.O. (2005) 'Blood–brain barrier-specific properties of a human adult brain endothelial cell line', *FASEB J*, 19:1872–1874.

Xiao, W., Fu, Q., Zhao, Y., Zhang, L., Yue, Q., Hai, L., Guo, L., & Wu, Y. (2019) 'Ascorbic acid-modified brain-specific liposomes drug delivery system with "lock-in" function', *Chemistry and physics of lipids* 224, 104727.

Yan, H., Wang, J., Yi, P., Lei, H., Zhan, C., Xie, C., Feng, L., Qian, J., Zhu, J., Lu, W., & Li C. (2011) 'Imaging brain tumor by dendrimer-based optical/paramagnetic nanoprobe across the blood-brain barrier', *Chemical Communications* 47 (28), pg. 8130-8132.

Yang, H.Y., Fu, Y., Jang, M.S., Li, Y., Yin, W.P., Ahn, T.K., Lee, J.H., Chae, H., & Lee, D.S. (2017) 'CdSe@ZnS quantum dots loaded in polymeric micelles as a PH-triggerable targeting fluorescence imaging probe for detecting cerebral ischemia area', *Colloids and Surfaces B: Biointerfaces* 155, pg. 497-506.

Yang, T., Order, K.E., & Abbruscato, T.J. (2007) 'Evaluation of bEnd5 cell line as an in vitro model for the blood–brain barrier under normal and hypoxic/aglycemic conditions', *Journal of Pharmaceutical Sciences* 96 (12), pg. 3196-3213.

Yang, X., McGlynn, E., Das, R., Pasca, S.P., Cui, B., & Heidari, H. (2021) 'Nanotechnology Enables Novel Modalities for Neuromodulation', *Advanced Materials*, 2103208.

Yue, K., Guduru, R., Hong, J., Liang, P., Nair, M., & Khizroev, S. (2012) 'Magneto-electric nanoparticles for non-invasive brain stimulation', *PLoS ONE* 7 (9), pg.1-5.

Zhang, C., Jin, Z., Zeng, B., Wang, W., Palui, G., & Mattoussi, H. (2020) 'Characterizing the Brownian Diffusion of Nanocolloids and Molecular Solutions: Diffusion-Ordered NMR Spectroscopy vs Dynamic Light Scattering', *Journal of Physical Chemistry B*, 124(22), pp. 4631–4650.

Zhang, Y., Chen, S., Xiao, Z., Liu, X., Wu, C., Wu, K., Liu, A., Wei, D., Sun, J., Zhou, L., & Fan, H. (2021) 'Magnetolectric Nanoparticles Incorporated Biomimetic Matrix for Wireless Electrical Stimulation and Nerve Regeneration', *Advanced Healthcare Materials*, 2100695, p. 2100695.

Zheng, X., Shao, X., Zhang, C., Tan, Y., Liu, Q., Wan, X., Zhang, Q., Xu, S., & Jiang, X. (2015) 'Intranasal H102 peptide-loaded liposomes for brain delivery to treat Alzheimer's disease', *Pharmaceutical research* 32 (12), pg. 3837-3849.

Zhu, X., Jin, K., Huang, Y., & Pang, Z. (2019) '7 - Brain drug delivery by adsorption-mediated transcytosis', *Brain Targeted Drug Delivery System*. Academic Press, pg. 159-183. ISBN 9780128140017.

Zou, Z., Shen, Q., Pang, Y., Li, X., Chen, Y., Wang, X., Luo, X., Wu, Z., Bao, Z., Zhang, J., Liang, J., Lingjia, K., Yan, L., Xiong, L., Zhu, T., Yuan, S., Wang, M., Cai, K., Yao, Y., Wu, J., Jiang, Y., Liu, H., Liu, J., Zhou, Y., Dong, Q., Wang, W., Zhu, K., Li, L., Lou, Y., Wang, H., Li, Y., & Lin H. (2019) 'The synthesized transporter K16APoE enabled the therapeutic HAYED peptide to cross the blood-brain barrier and remove excess iron and radicals in the brain , thus easing Alzheimer ' s disease', pp. 394–403.

